

MICROCOPY RESOLUTION TEST CHART  
NATIONAL BUREAU OF STANDARDS - 1963 - A

12

AFGL-TR-85-0191

DETAILED GRAVITY ANOMALIES AND SEA SURFACE HEIGHTS DERIVED FROM  
GEOS-3/SEASAT ALTIMETER DATA

Richard H. Rapp

The Ohio State University  
Research Foundation  
Columbus, Ohio 43212

August 1985

Scientific Report No. 9

Approved for public release; distribution unlimited

AD-A166 593

DTIC FILE COPY

DTIC  
ELECTE  
APR 15 1986  
S D  
B

AIR FORCE GEOPHYSICS LABORATORY  
AIR FORCE SYSTEMS COMMAND  
UNITED STATES AIR FORCE  
HANSCOM AFB, MASSACHUSETTS 01731

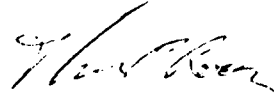
098

CONTRACTOR REPORTS

This technical report has been reviewed and is approved for publication.

  
CHRISTOPHER JEKELI

Contract Manager



THOMAS P. ROONEY

Chief, Geodesy & Gravity Branch

FOR THE COMMANDER



DONALD H. ECKHARDT

Director

Earth Sciences Division

This report has been reviewed by the ESD Public Affairs Office (PA) and is releasable to the National Technical Information Service (NTIS).

Qualified requestors may obtain additional copies from the Defense Technical Information Center. All others should apply to the National Technical Information Service.

If your address has changed, or if you wish to be removed from the mailing list, or if the addressee is no longer employed by your organization, please notify AFGL/DAA, Hanscom AFB, MA 01731. This will assist us in maintaining a current mailing list.

unclassified

SECURITY CLASSIFICATION OF THIS PAGE (When Data Entered)

REPORT DOCUMENTATION PAGE		READ INSTRUCTIONS BEFORE COMPLETING FORM
1. REPORT NUMBER AFGL-TR-85-0191	2. GOVT ACCESSION NO. <b>AD A166593</b>	3. RECIPIENT'S CATALOG NUMBER
4. TITLE (and Subtitle) DETAILED GRAVITY ANOMALIES AND SEA SURFACE HEIGHTS DERIVED FROM GEOS-3/SEASAT ALTIMETER DATA	5. TYPE OF REPORT & PERIOD COVERED Scientific Report No. 9	
	6. PERFORMING ORG. REPORT NUMBER OSU/DGSS-365 ✓	
7. AUTHOR(s) Richard H. Rapp	8. CONTRACT OR GRANT NUMBER(s) F19628-82-K-0022	
9. PERFORMING ORGANIZATION NAME AND ADDRESS The Ohio State University Research Foundation 1958 Neil Avenue Columbus, Ohio 43210	10. PROGRAM ELEMENT, PROJECT, TASK AREA & WORK UNIT NUMBERS 61102F 2309G1BC	
11. CONTROLLING OFFICE NAME AND ADDRESS Air Force Geophysics Laboratory Hanscom AFB, Massachusetts 01730 Monitor/Christopher Jekeli/LWG	12. REPORT DATE August 1985	
	13. NUMBER OF PAGES 132	
14. MONITORING AGENCY NAME & ADDRESS (if different from Controlling Office)	15. SECURITY CLASS. (of this report) Unclassified	
	15a. DECLASSIFICATION/DOWNGRADING SCHEDULE	
16. DISTRIBUTION STATEMENT (of this Report)  Approved for public release; distribution unlimited		
17. DISTRIBUTION STATEMENT (of the abstract entered in Block 20, if different from Report)		
18. SUPPLEMENTARY NOTES		
19. KEY WORDS (Continue on reverse side if necessary and identify by block number)  Earth's Gravity Field Satellite Altimetry Geos-3, Seasat		
20. ABSTRACT (Continue on reverse side if necessary and identify by block number) ➤ Gravity anomalies and sea surface heights have been computed on a 0°125 grid in the ocean areas from a combined Geos-3/Seasat altimeter data set. The basic procedure used least squares collocation estimation where model covariance models were tailored to individual areas through altimeter residual variance scaling. Preliminary tests led to production prediction procedures using a reference model defined by a set of potential coefficients complete to degree 180. Comparisons of the predicted anomalies with ship derived		

20.

values showed agreements varying from  $\pm 9$  to  $\pm 30$  mgals. No corrections to the altimeter implied sea surface heights were made for sea surface topography effects. The maximum anomaly predicted was 396 mgals near Hawaii and the most negative anomaly was -361 mgals over the Puerto Rican Trench. The  $0^\circ 125'$  data set has been used to display the results using color plots, contour maps, and perspective views. The gridded data was used to compute  $1^\circ \times 1^\circ$  and  $0^\circ 5' \times 0^\circ 5'$  mean values.  $1^\circ$  mean anomalies were compared to terrestrial data where a difference of  $\pm 7$  mgals was found in comparing 10139 values.  $\blacktriangleleft$

The actual resolution of the data was estimated to be about  $0^\circ 19'$  based on a power spectrum analysis. The resolution is limited by our data selection process which used 300 data points, a thinned altimeter data set for the prediction of the  $0^\circ 125'$  in a  $3^\circ \times 3^\circ$  block with one data selection, and matrix inversion. The predicted data were used to compute 104 potential coefficient spectra using flat earth approximations developed by Forsberg. The spectra were classified in terms of smooth, mild, or rough areas. The great majority (78) of the spectra were in the smooth classification. Good agreement was found from spectra computed from topographically reduced land data and the mean ocean data, but the spectra from two models were substantially higher than found from the ocean data. The decay of the spectra could be represented in the form of  $\lambda^{-3.6}$  which follows from the Forsberg data and the altimeter data considered to degree 800. The geoid undulation information between various spherical harmonic degrees was computed using the spectra and compared with other results. The geoid information was quite sensitive to the type of region from which the spectra was computed.

$0.5 \times 0.5 \text{ } \circ \text{ } \circ \text{ } \circ$

FOREWORD

This report was prepared by Richard H. Rapp, Professor, Department of Geodetic Science and Surveying, The Ohio State University, under Air Force Contract No. ~~F19628-82~~-K-0022, The Ohio State University Research Foundation Project No. 714274. The contract covering this research is administered by the Air Force Geophysics Laboratory, Hanscom Air Force Base, Massachusetts, with Dr. Christopher Jekeli, Scientific Program Officer.

**S** DTIC  
ELECTE **D**  
APR 15 1986  
**B**

Accession For	
NTIS GRA&I	<input checked="" type="checkbox"/>
DTIC TAB	<input type="checkbox"/>
Unannounced	<input type="checkbox"/>
Justification	
By _____	
Distribution/	
Availability Codes	
Dist	Avail. and/or Special
A-1	



## ACKNOWLEDGEMENTS

This study concludes a long chain of studies related to the processing of satellite altimeter data. Many graduate students at Ohio State played an important role ultimately leading to the results described in this report. Mr. Ed Herbrechtsmeier wrote many of the fundamental programs for the processing of the original large Geos-3 data set. Mr. David Rowlands extended these program for the application to the Seasat data released by JPL. Mr. Jaime Cruz improved the first Seasat analysis by introducing additional crossovers in contour areas. Mr. Chih-kuo Liang first started to work with the Geos-3 altimeter data for the combinations with the Seasat data. Liang carried out all the production predictions described in this report, developing unique programs to handle and store the large amounts of input and output data. Mr. Theodossios Engelis helped in the tests of various prediction models; the development of sea surface topography models, and the power spectrum analysis of the final results. Mr. Chugiat Wichiencharoen prepared programs for analyzing the many potential coefficient spectra that were computed from the predicted anomalies. And Mr. Piotr Laskowski developed several of the plotting programs that were used to display the results.

A substantial portion of the computer time used in this research was provided by the Instruction and Research Computer Center, The Ohio State University.



## TABLE OF CONTENTS

	PAGE
FOREWORD	iii
ACKNOWLEDGEMENTS	iv
SECTION	
Introduction	1
Method	1
The Ellipsoid Parameters Used in this Study	2
The Sea Surface Topography Models	3
Covariance Models	3
Numerical Values of $C(N_p, \Delta g_Q)$	14
30'x30' Mean Anomaly Predictions	18
Japan Trench Predictions and Comparisons	18
Puerto Rico Trench Predictions and Comparisons	19
Blake Plateau Predictions and Comparisons	20
Point Anomaly Predictions--Preliminary Tests	21
The Accuracy Computations	40
The Choice for Prediction Runs	41
The Satellite Altimeter Data Set	42
Sea Surface Topography Considerations for Production Computations	45
Operational Data Selection and Production Runs	48
The Standard Deviations of the Predicted Quantities	53
Statistical Analysis of the Point Predictions	53
Selected Anomaly and Sea Surface Height Maps	58
Spectral Content of the 0:125x0:125 Predicted Values	72

1°x1° Mean Anomaly Determinations and Comparisons with Terrestrial Data	72
0:5x0:5 Mean Anomaly Determination	78
Potential Coefficient Behavior	79
Anomaly Degree Variances	88
Geoid Undulation Information by Degree Range	90
Maximum Anomaly and Sea Surface Height Gradients	91
Point Anomaly Variance	93
Summary	93
REFERENCES	97
APPENDIXES	
A. Readjustment of Selected Seasat Primary Arcs by C. Liang	100
B. Estimates of Sea Surface Topography by T. Engelis	105
C. Power Spectrum Analysis of the 1/8°x1/8° Anomalies by T. Engelis	116
D. Location of Rough, Mild, and Smooth 15°x15° Areas Used in Spectrum Classification	125

## Introduction

This report is related to the recovery of gravity anomalies from satellite altimeter data. Several previous reports have been prepared on the subject by the author (Rapp, 1983a, 1979). The emphasis in our previous studies has been the determination of mean gravity anomalies in 1°x1° and 5° extent. In this study our emphasis will be on point gravity anomalies.

A second difference of this study from our previous ones relates to the data used. In our previous studies we have used only Geos-3 (Rapp, 1979b) or only Seasat (Rapp, 1983a) altimeter data. We now have a combined Geos-3/Seasat data set (Liang, 1983) that provides a denser data set than either alone. In addition new adjustments of the Seasat data have taken place. These adjustments have substantially improved the consistency of the altimeter data over what was used in our earlier studies.

The results presented here are not the first attempt we have made at the recovery of point gravity anomalies. Using Geos-3 data we had previously shown the good agreement between ship measured gravity data and altimetric implied data. In this report we will look at many more comparisons and carry out an ocean wide estimation of gravity anomalies on a uniform grid.

## Method

The method of anomaly recovery is based on least squares collocation. The anomalies are computed from the corrected sea surface height using a reference gravity field and a set of covariances. Specifically we have:

$$\Delta g = \underline{C}_{gh} (\underline{C}_{hh} + D)^{-1} (h - h_R) + \Delta g_R \quad (1)$$

$$m_g^2 = \underline{C}_{gg} - \underline{C}_{gh} (\underline{C}_{hh} + D)^{-1} \underline{C}_{hg} \quad (2)$$

where

- $\Delta g$  predicted free-air gravity anomaly with respect to the ellipsoid gravity field;
- $h$  column vector of the altimeter implied geoid undulations;
- $\underline{C}_{gh}$  row vector containing the covariance (referred to the reference field) between the anomaly being predicted and the given geoid undulations;
- $\underline{C}_{hh}$  square, symmetric matrix containing the covariances (referred to the reference field) between the given geoid undulations;
- $D$  error covariance matrix of the 'observed' geoid undulations which was taken to be a diagonal matrix whose elements corresponded to the square of the standard deviation of the altimeter measurement;

- $\underline{C}_{gg}$  expected mean square value (referred to the reference field) of of the anomaly predicted;
- $m_g$  predicted anomaly standard deviation;
- $\Delta g_R, h_R$  gravity anomaly and geoid undulation implied by the reference gravity field.

Equations similar to (1) and (2) can be written for the estimation of the geoid undulation. Our ultimate aim will be to apply (1) to obtain  $\Delta g$  and the geoid undulations at spherical grid interval with respect to a defined reference system. We will also discuss tests in which 30' mean gravity anomalies were computed in preliminary studies that were made early in this research effort.

### The Ellipsoid Parameters Used in this Study

The altimeter data we used refers to the ellipsoid of the Geodetic Reference System 1980. The parameters of the ellipsoid are:

$$a = 6378137 \text{ m}$$

$$f = 1/298.257$$

In the collocation solutions we intend to use, the data vector (i.e. the geoid undulations) should refer to the best ellipsoid parameters. Currently the best "a" value is thought to be (Rapp, 1983b).

$$a = 6378136 \text{ m}$$

To refer the existing sea surface heights to the new ellipsoid we must add 1 meter to such values. This will be done for all computations in this paper so that all geoid undulations given in this paper will refer to the following ellipsoid:

$$a = 6378136 \text{ m}$$

$$f = 1/298.257$$

The appropriate gravity formula must also be considered as a reference for the gravity anomalies. The equatorial gravity for GRS80 is:

$$\gamma_a = 9.780327 \text{ ms}^{-2}$$

$$= 978032.7 \text{ mgals}$$

The equatorial gravity for the ellipsoid used in our computations (to be consistent with the 6378136 m equatorial radius) is therefore (1 m corresponds to approximately 0.3 mgal change in gravity):

$$\gamma_a = 978033.0 \text{ mgals}$$

Before the anomalies derived from the altimeter data are associated with a specific gravity formula the effect of the atmosphere must be considered to obtain anomalies that are consistent with terrestrial anomaly estimates (Rapp, 1979b). To do this 0.87 mgals must be subtracted from the anomaly derived from equation (1).

All anomaly comparisons that are made in this report between terrestrial and altimeter derived anomalies have been made after conversion to the same gravity formula and the application of the atmospheric correction to the altimeter anomalies. The anomaly maps that will be given do not have the atmospheric correction applied.

### The Sea Surface Topography Model

The sea surface heights obtained from the altimeter data refer to the ocean surface which is not an equipotential surface. To obtain the geoid, sea surface topography must be removed from the altimeter defined sea surface height. Actual estimates of sea surface topography are difficult to obtain on a global, time critical basis. We have therefore used the data of Levitus (1982) to develop a sea surface topography data base for our initial tests.

We specifically started with the mean annual dynamic topography computed by Levitus with respect to the 2250 dbar surface. The data consisted of 33856 1°x1° values in the ocean regions. The mean value of these values was 2.02 dyn-m. This value is used to define the geoid and consequently was removed from all of the original values. The remaining values in land areas were assigned a value of zero so that a complete data array consisted of 64800 values. For the evaluation of the sea surface topography at an arbitrary point a bilinear interpolation procedure was used. The above procedure was developed and implemented in a subroutine by T. Engelis. A discussion of sea surface topography using the Levitus data is given by Engelis (1983, 1985).

It should be noted that this sea surface topography represents a long term time average (~ 20 years) and a spatial average on the order of 700 km.

### Covariance Models

The covariances that appear in equations (1) and (2) need to be obtained from the empirical data, from covariance models, or a combination of both. Since  $(h - h_p)$  is the "observed" quantity we could directly compute the  $C_{hh}$  covariance function from the individual samples in a region. The covariance function would reflect the geoid undulation signal information, altimeter noise, and the noise or error contribution from the reference field.

The cross covariances ( $C_{\Delta gh}$ ) can not be obtained by empirical means because we do not have the empirical gravity data to cross correlate with the altimeter residuals. The cross covariances must be obtained from some models

that are somehow related to the actual data area.

The first theoretical covariance function considered is that developed by Tscherning and Rapp (1974) on the basis of an anomaly degree variance model,  $c_n$ . Given such a model the covariance functions with respect to a degree  $N$  reference model are as follows:

$$C(\Delta g_P, \Delta g_Q) = \sum_{n=N+1}^{\infty} c_n s^{n+2} P_n(\cos \psi_{PQ}) \quad (3)$$

$$C(\Delta g_P, N_Q) = \frac{R^2}{r_P r_Q} \sum_{n=N+1}^{\infty} \frac{c_n}{(n-1)} s^{n+1} P_n(\cos \psi_{PQ}) \quad (4)$$

$$C(N_P, N_Q) = R^2 \sum_{n=N+1}^{\infty} \frac{c_n}{(n-1)^2} s^{n+1} P_n(\cos \psi_{PQ}) \quad (5)$$

For the Tscherning/Rapp model we have:

$$c_n = \frac{A(n-1)}{(n-2)(n+B)} \quad (6)$$

where  $A=425.28 \text{ mgal}^2$  and  $B=24$ . For points  $P$  and  $Q$  located on a mean sphere (as we will assume) we have  $s=0.999617$ . Closed expressions for (3), (4), and (5) exist when  $N=3$ . For higher  $N$ , the covariances are found by removal of the contribution from degree 3 to  $N$ . Subroutine COVA (in Tscherning et al. (1974)) can be used for such a computation.  $C(N_P, N_Q)$  is shown in Figure 1 for  $N=20$  and in Figure 2 for  $N=180$ . For  $N=20$ , the signal covariance is  $13.32 \text{ m}^2$  and the correlation length (i.e.,  $s$  where  $C(s)=C_0/2$ ) is 2:30. For  $N=180$ , the signal variance is  $0.22 \text{ m}^2$  and the correlation length is 0:29. The smaller correlation length as  $N$  increases is an advantage in using higher degree reference fields.

The errors in the reference field can be considered knowing the error degree variances of the model (Colombo, 1980). The two models considered here are the GEM9 field (Lerch et al., 1979) which is complete to degree 20, and the 180x180 model of Rapp (1981). The error degree variances for the GEM9 field can be computed from the published accuracy estimates of the coefficients. For the Rapp model the published accuracy estimates to degree 36 have been used. Beyond this a more optimistic estimate assuming a global anomaly accuracy of  $\pm 10 \text{ mgals}$  has been used.

The error covariances are computed using equations (3, 4, 5) with  $\delta c_n$  replacing  $c_n$ . The error covariances for each field is shown in Figure 1 (GEM9) and Figure 2 (OSU81) for  $C(N_P, N_Q)$ .

The total covariance function for use in equation (1) is the sum of the signal and noise covariance functions. We have (Colombo 1980):

$$C(\psi) = C_R(\psi) + \Delta C(\psi) \quad (7)$$

where  $C_R(\psi)$  is the covariance function implied by the reference field and  $\Delta C(\psi)$  is that implied by the potential coefficient noise model. This sum for  $C(N_p, N_q)$  is shown in Figures 1 and 2. The variance (with noise) for the GEM9 field is now 16.3 m<sup>2</sup> with a correlation length of about 2:6 which is slightly longer than when the noise was not added. The variance (with noise) for the OSU81 field is now 1.35 m<sup>2</sup> and the correlation length is 2:0 which is considerably larger than the case without noise.

An alternative interpretation to equation (7) has been given by Jekeli (1985, private communication) who showed that  $\Delta C$  could be considered part of the noise matrix D. To show this Jekeli represents the residual altimeter observation as

$$\hat{h} - \hat{h}_R = h - h_R + \varepsilon_{h-h_R}$$

where the  $\hat{\phantom{h}}$  indicates the observed quantity and  $\varepsilon$  is the error in the observations. We have:

$$\text{cov}(\hat{h} - \hat{h}_R, \hat{h} - \hat{h}_R) = \text{cov}(h - h_R, h - h_R) + \text{cov}(\varepsilon_{h-h_R}, \varepsilon_{h-h_R})$$

If we assume no correlation between  $\varepsilon_h$  and  $\varepsilon_{h_R}$  we have:

$$\text{cov}(\varepsilon_{h-h_R}, \varepsilon_{h-h_R}) = \text{cov}(\varepsilon_h, \varepsilon_h) + \text{cov}(\varepsilon_{h_R}, \varepsilon_{h_R})$$

We thus have:

$$\text{cov}(\hat{h} - \hat{h}_R, \hat{h} - \hat{h}_R) = \text{cov}(h - h_R, h - h_R) + \text{cov}(\varepsilon_h, \varepsilon_h) + \text{cov}(\varepsilon_{h_R}, \varepsilon_{h_R})$$

This result is the same as (7) when the D given in (1) is added.

The covariance model has two primary parameters (A, s) that can easily be changed in order to fit an empirical covariance function. The variance of the quantity is primarily dependent on A so that knowing one we can estimate the other. The second parameter s depends on the ratio of the Bjerhammer sphere radius to the mean radius of the earth:

$$s = \left( \frac{R_B}{R} \right)^2 \quad (8)$$

One quantity that is important in the modelling of an empirical covariance function is the correlation length (Moritz, 1980, p. 174),  $\zeta$ .  $\zeta$  is the value where  $C(\zeta) = C(0)/2$ . We have computed this correlation length for the undulation covariance function for the Tscherning/Rapp degree variance model

using different values of  $R_B$  (with  $R=6371.0$  km) for a degree 20 and a degree 180 reference field. These results are shown in Table 1.

**Table 1**  
**Geoid Undulation Correlation Lengths for the Tscherning/Rapp**  
**Degree Variance Model**

$R_B - R_E$ (km)	Degree 20 Reference (degree)	Degree 180 Reference (degree)
0.10	2.30	0.29
0.50	2.30	0.29
1.00	2.31	0.29
1.50	2.31	0.29
2.00	2.32	0.30
2.50	2.32	0.30
3.00	2.33	0.31
3.50	2.33	0.31

We see that the correlation length is insensitive to  $R_B - R_E$  for the differences considered. As the difference increases, the correlation length increases. We would not be able to match well, with this model, undulation covariances that have correlation lengths shorter than given in Table 1.

Other degree variance models can be used (Moritz(1980), Rapp(1979a)) that involve more parameters which enable shorter correlation lengths to be modeled.

Another covariance model that will be useful is that given by Jordan (1972). He proposes a third order Markov undulation model with consistent covariance and cross covariance for quantities of interest to us. In our application we consider these models for the residual observed quantities, i.e.  $(x - x_{ref})$ . Specifically we have:

$$C(N_P, N_Q) = \sigma_N^2 \left( 1 + \frac{r}{D} + \frac{r^2}{3D^2} \right) e^{-r/D} \quad (9)$$

$$C(N_P, \Delta g) = \frac{2\sigma_N \sigma_g}{\sqrt{6}} \left[ \frac{r}{D} \left( 1 - \frac{r^2}{3D^3} \right) \cdot \left[ I_0 \left( \frac{r}{2D} \right) K_1 \left( \frac{r}{2D} \right) - I_1 \left( \frac{r}{2} \right) K_0 \left( \frac{r}{2D} \right) \right] + \frac{r^2}{4D^2} \cdot \left[ I_0 \left( \frac{r}{2D} \right) K_0 \left( \frac{r}{2D} \right) + I_1 \left( \frac{r}{2D} \right) K_1 \left( \frac{r}{2D} \right) \right] \right] \quad (10)$$



Figure 1  
Undulation Covariances with Respect  
to Degree 20 Field

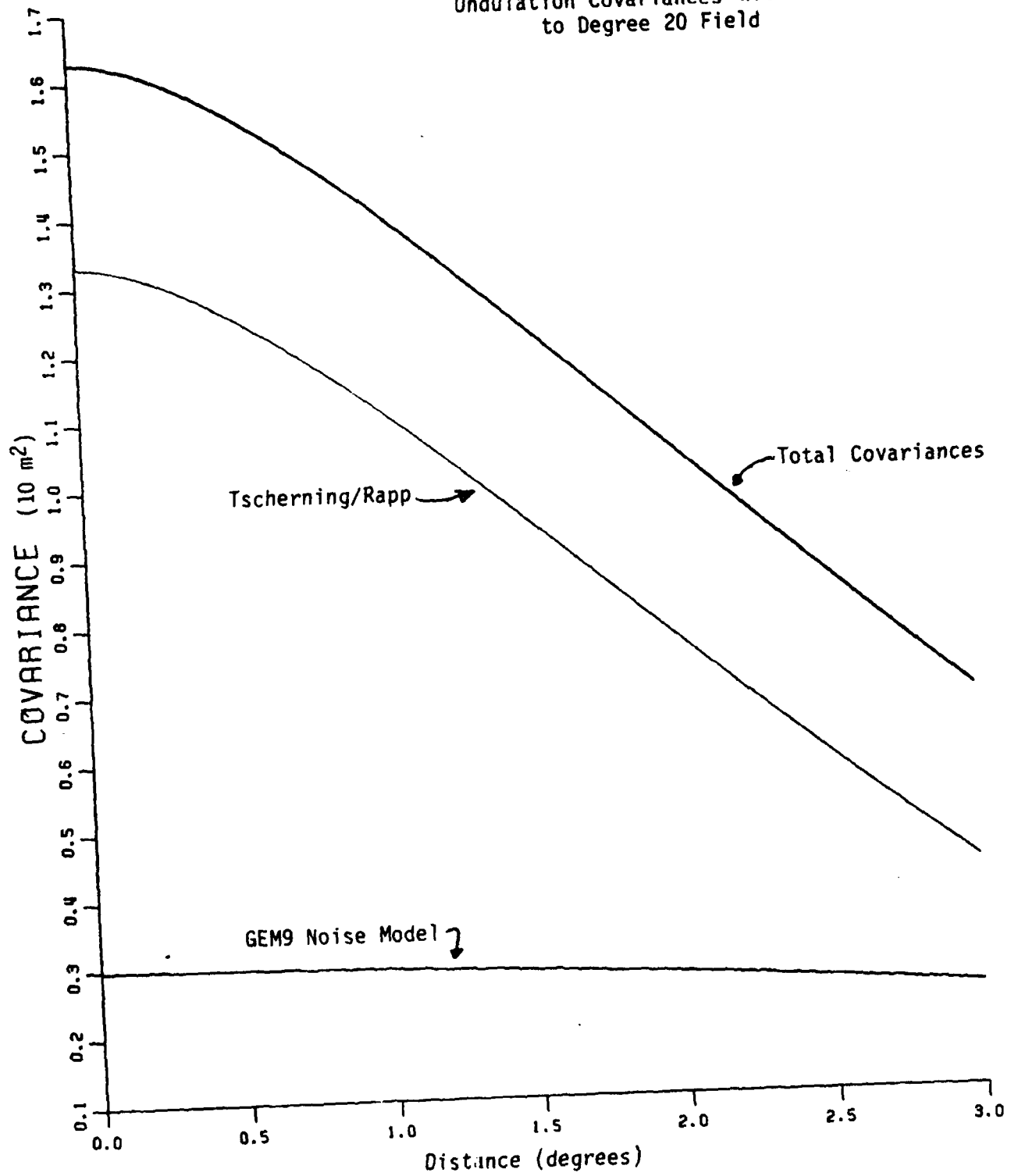
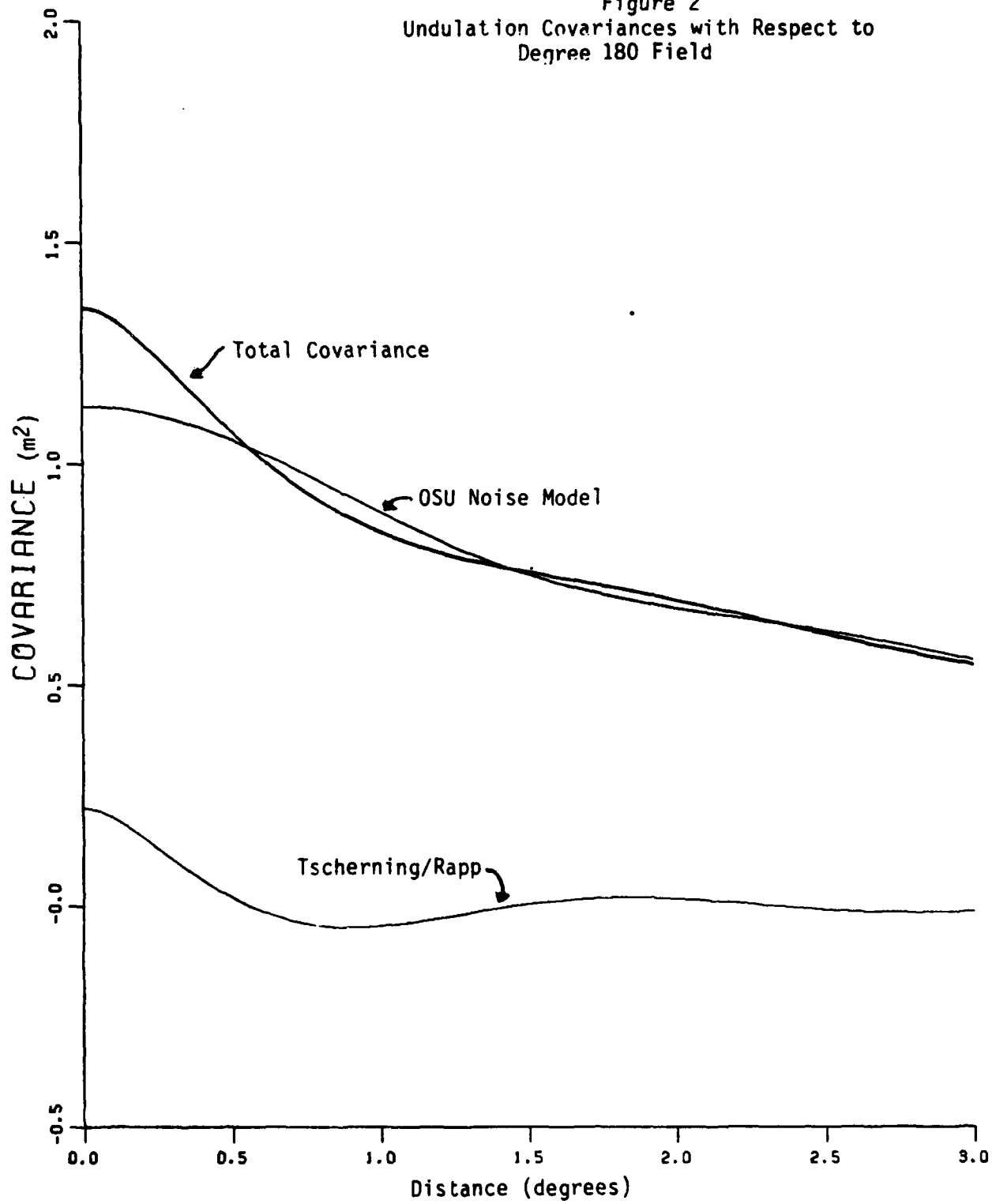


Figure 2  
Undulation Covariances with Respect to  
Degree 180 Field



where:  $\sigma_N^2$  is the undulation variance;  
 $\sigma_g^2$  is the anomaly variance;  
 $r$  is the PQ separation  
 $d$  is the characteristic distance  
 $I_j, K_j$  are modified Bessel functions of order  $j$

The correlation distance ( $\zeta$ ) of the stationary random process is the separation at which the covariance has declined to  $1/e$  of the variance. That is,  $C(\zeta) = 0.367879C(0)$ . Each gravimetric quantity will have its own correlation distance that is related to the characteristic distance:

$$\zeta_N = 2.905D = \text{undulation correlation distance} \quad (11)$$

$$\zeta_g = 1.3610 = \text{anomaly correlation distance} \quad (12)$$

This Jordan model has two parameters,  $\sigma_N$  and  $D$ , that can be determined to yield fits of the model to empirical covariance functions. From such a function we have immediately  $\sigma_N$ . We can numerically determine  $\zeta$  from the covariance function and then compute  $D$  from (11) when dealing with undulations. Given  $\sigma_N$  and  $D$ , the anomaly variance,  $\sigma_g$ , can be computed from:

$$\sigma_g = \sqrt{\frac{2}{3}} \gamma \frac{\sigma_N}{D} \quad (13)$$

where  $\gamma$  is an average value of gravity. We note for our application of anomaly recovery the importance of  $C(N_p, \Delta g_q)$ . In the Jordan model this cross covariance function is quite sensitive to  $\sigma_N$  and  $D$ . The smaller  $D$  is, the larger  $\sigma_g$ , and the larger the cross covariance is.

#### Empirical Undulation Covariance Estimates

Given estimates of sea surface heights from satellite altimetry we can compute at these points the undulation implied by the GEM9 field or by the OSU81 180x180 field. We then have a set of residual heights for which we now wish to determine an empirical covariance function.

Given a quantity  $s$ , at location  $x, y$ , the isotropic covariance function can be written as:

$$C_{ss}(r) = E((s(X, Y) - \bar{s})(s(X+x, Y+y) - \bar{s}))$$

$$r = \sqrt{x^2 + y^2} \quad (14)$$

Here  $\bar{s}$  is the mean (in the given data set) of the quantity for which the auto correlation function is being computed. Equation (14) is written to show the removal of the mean value of the observed quantity from the data in the computation. This effectively "centers" (Moritz, 1980, p.76) the data. We will look at covariance samples when  $\bar{s}$  is used and when it is set to zero. The covariance functions computed from (14) will reflect the signal and reference field. As such it would be comparable to  $C(\psi)$  given in (7) plus the noise  $D$ .

Given a set of altimeter data in a specific region, the covariance function is computed by taking the mean value of the products as shown in (14). The distance to be associated with a product is used to store and sum the product in a histogram unit. For example, one bin may contain all products for which  $0.9754 \leq \psi < 1.025$ . An average  $\psi$  is calculated for each bin and is thus associated with each mean product.

The tests that we made took data in a.) areas of  $3^\circ \times 3^\circ$  and b.) areas of  $2^\circ \times 2^\circ$ . We carried them out in several different geographic areas with respect to the GEM9 field and the OSU81 field as reference gravity models.

The first test area is that of the New England seamounts in the western Atlantic. The empirical undulation covariance with respect to the GEM9 and OSU81 fields are shown in Figures 3 and 4 where the mean has , and has not, been removed from the data vector. For the GEM9 case the mean was  $-2.2\text{m}$ , accounting for the large difference in the residual undulation variance. For the 180 case the mean was  $0.15\text{ m}$  so that the two curves are close together. The data for these two figures was taken in a  $2^\circ \times 2^\circ$  block.

Figure 5 show a 180 covariance function in the Louisville Ridge area in the southwest Pacific. The mean of the residual was  $0.09\text{m}$ . The data for this graph was selected in a  $3^\circ \times 3^\circ$  area.

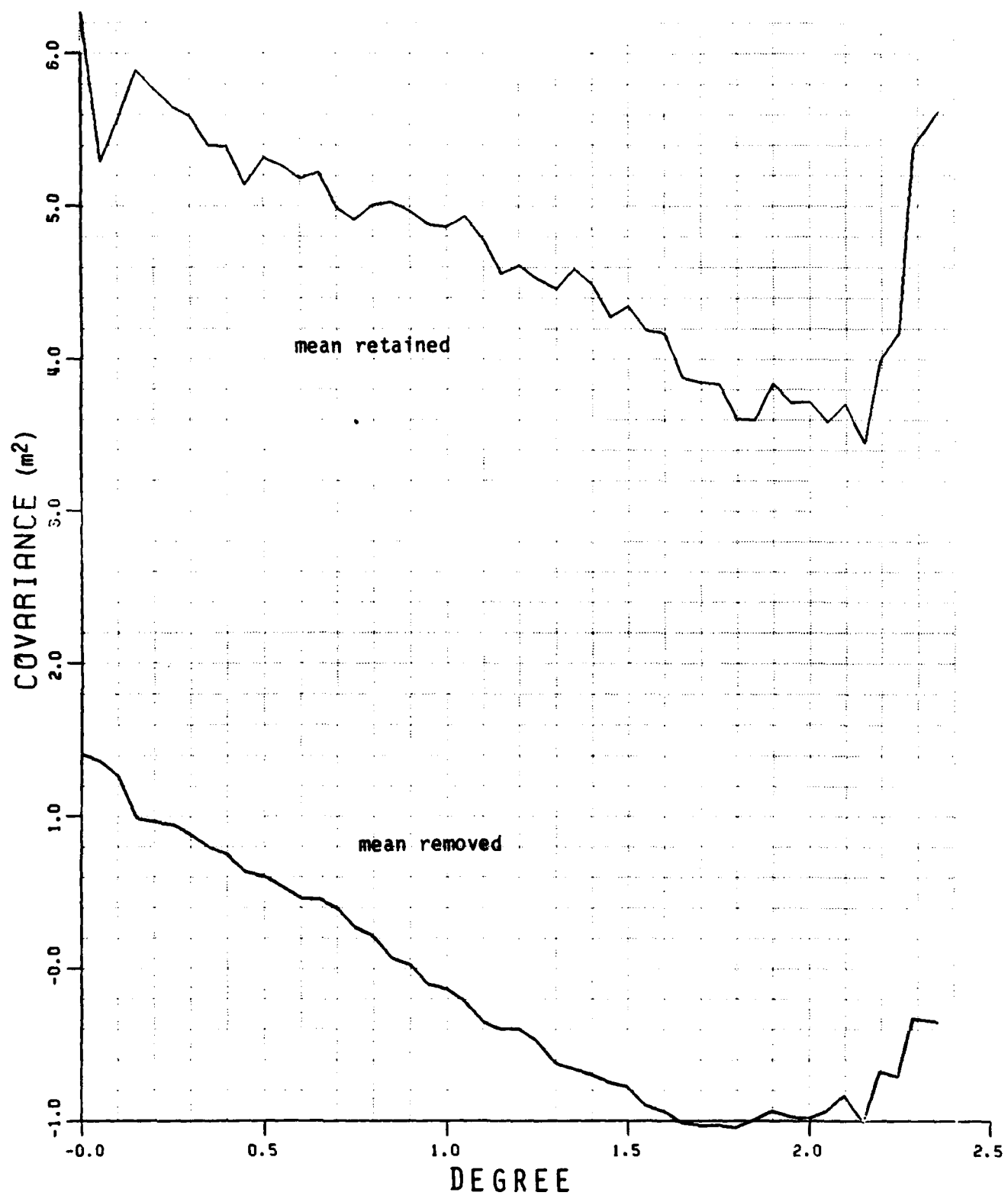


Figure 3  
 Empirical Undulation Covariance Function in New England Sea Mount Area  
 (GEM9 reference)

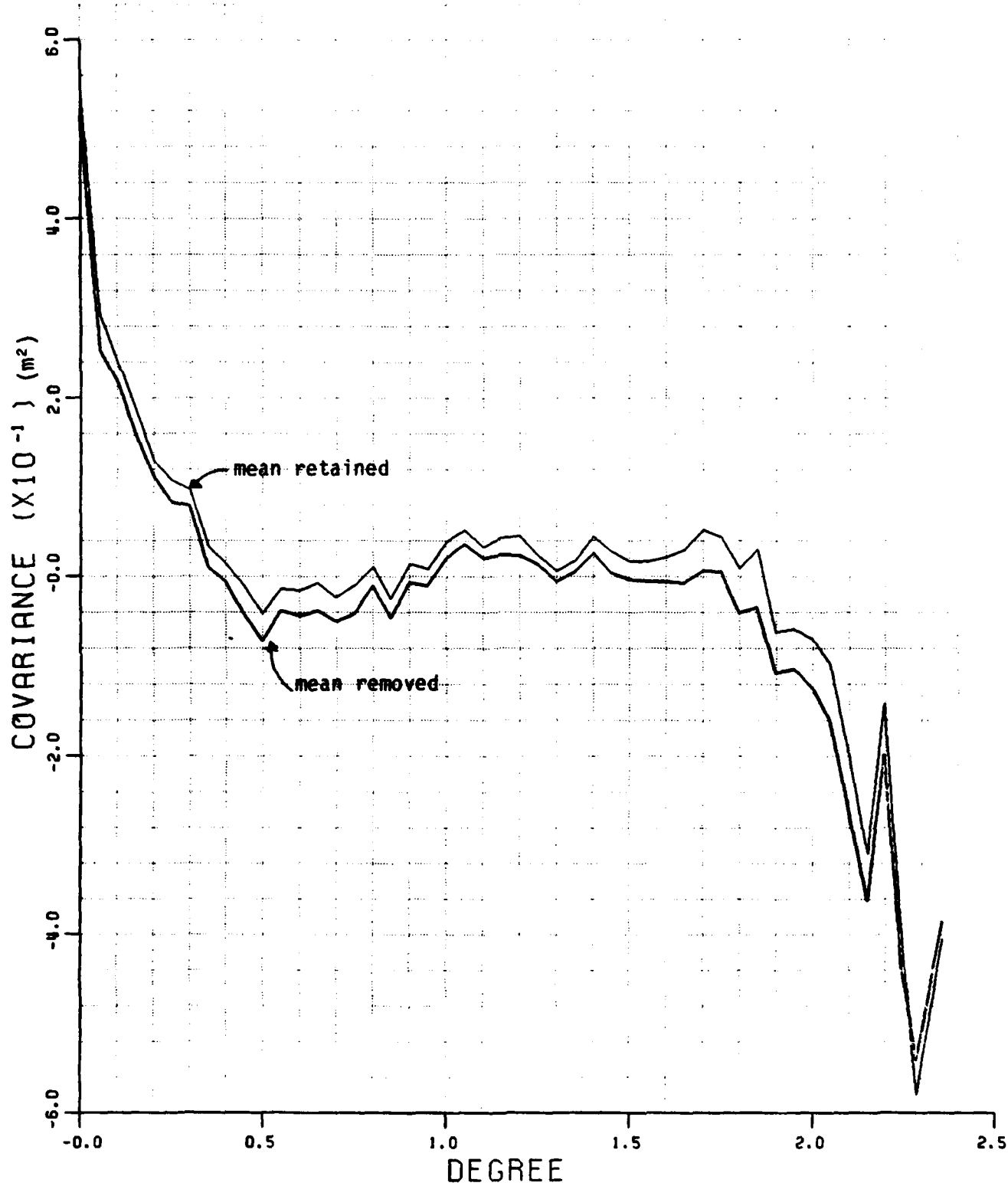


Figure 4  
Empirical Covariance Function in New England Sea Mount Area  
(OSU 180 reference)

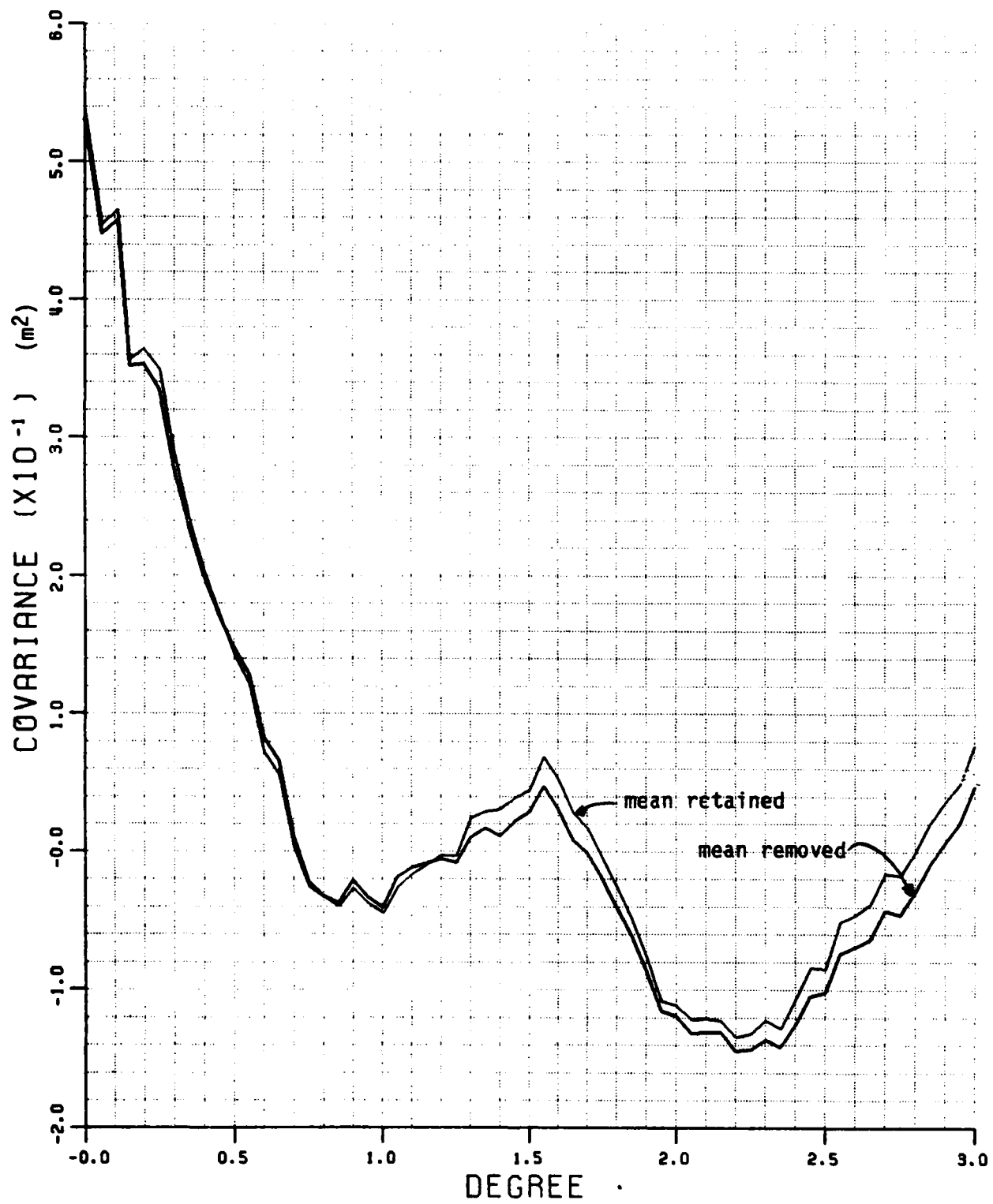


Figure 5  
 Empirical Covariance Functions in the Louisville Ridge Area  
 (OSU 180 reference)

Of more specific interest is the relation of the empirical covariance functions to the model covariance function described earlier. Figures 6 and 7 show empirical and model covariance functions based on data in a  $3^{\circ} \times 3^{\circ}$  area around the Puerto Rico trench for the GEM9 and OSU180 reference fields respectively. Plotted in each figure is the Tscherning/Rapp covariance function scaled so that the sum of the residual and noise variance would be the same as the actual variance, and the Jordan model with  $\sigma_N^2$  equal to the empirical variance, and the D value estimated from the correlation distance. For the GEM9 reference, D was 0.17 while it was 0.63 for the OSU180 reference field. We note the good fit of the Jordan function for  $\psi$  up to  $1.2$  for the 180 reference and higher for the GEM9 reference.

Figure 8 is another example using data in the Louisville Ridge area with the 180 reference field. The D value in this case is 0.14.

These curves demonstrate that the Jordan function can be fitted to the empirical function in a simple manner. The Tscherning/Rapp covariances show a greater correlation than appears to exist for the empirical data in the areas tested. In some cases it was not possible to determine a D value for the Jordan model due to the slow decay of the covariance function. In some cases D was found to be small (i.e.  $< 0.1$ ). The small D implies a large  $\sigma_g$  which can become unreasonable. In such cases we will set D to 0.1.

#### Numerical Values of $C(N_p, \Delta g_Q)$

We now consider numerical values of  $C(N_p, \Delta g_Q)$  based on equation (4) (with both signal and reference field noise contributions) and equation (10). For the use of equation (4), the  $C(N_p, N_Q)$  and  $C(N_p, \Delta g_Q)$  functions have been scaled to give the same variance for  $C(N_p, N_Q)$  as determined empirically. For the use of (10), the  $\sigma_N^2$  has been found through examinations of the numerical covariance function. However to show the dependence of  $C(N_p, \Delta g_Q)$  on D, we have used a number of different values. The value of  $\sigma_N^2$  for two different areas was computed with data referenced to the OSU180 field. The first area was near the Puerto Rico Trench where  $\sigma_N^2$  was  $1.93\text{m}^2$  and the D estimate was 0.133. The second area was in the North Sea where  $\sigma_N^2$  was  $0.24\text{m}^2$  and D was 0.199. For these two areas we have computed  $C(N_p, \Delta g_Q)$ . Values with  $\psi = 0^{\circ}$  are shown in Table 1.



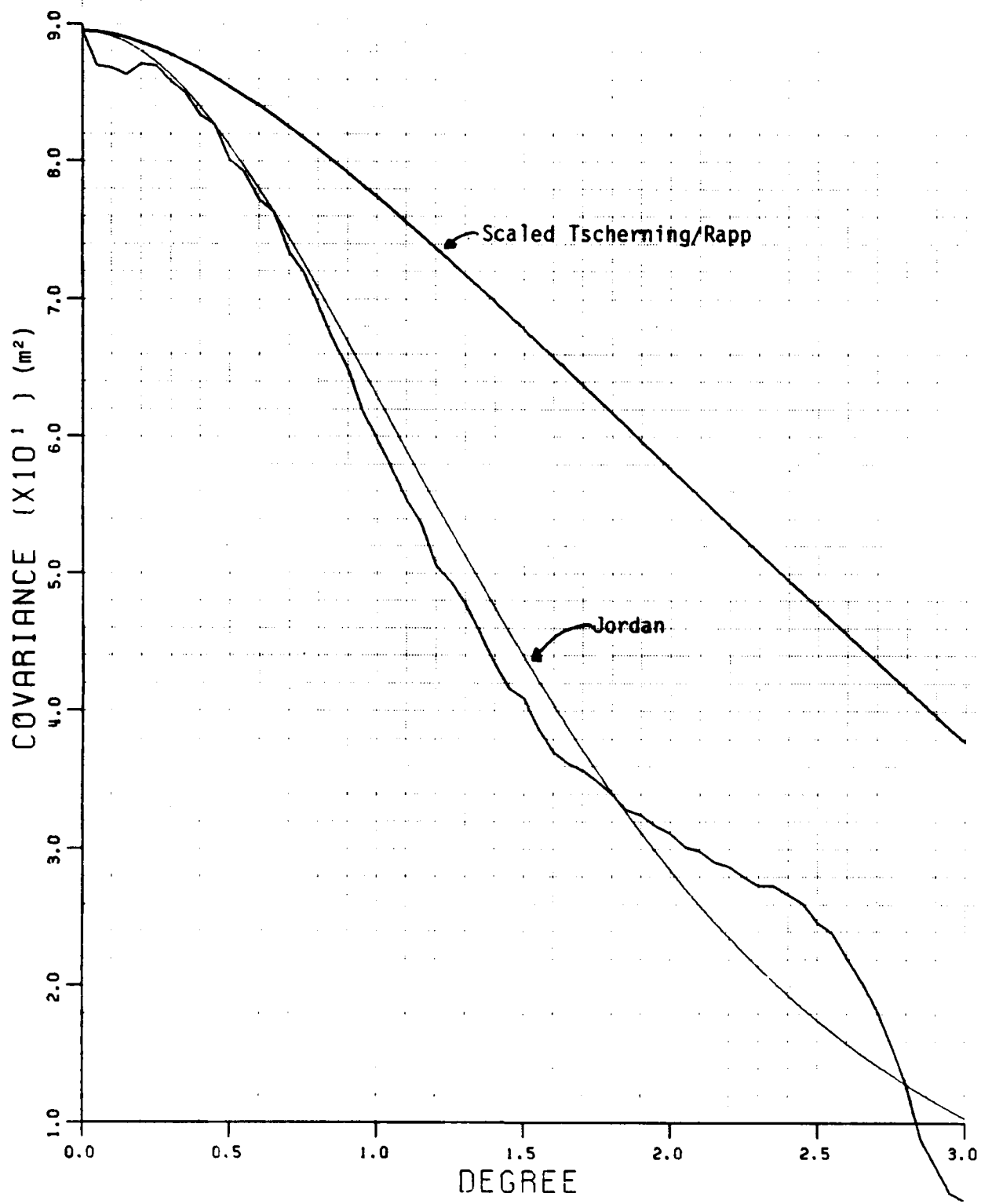


Figure 6  
 Empirical and Model Geoid Undulation Covariances in the Puerto Rico Trench Area (GEM9 reference)

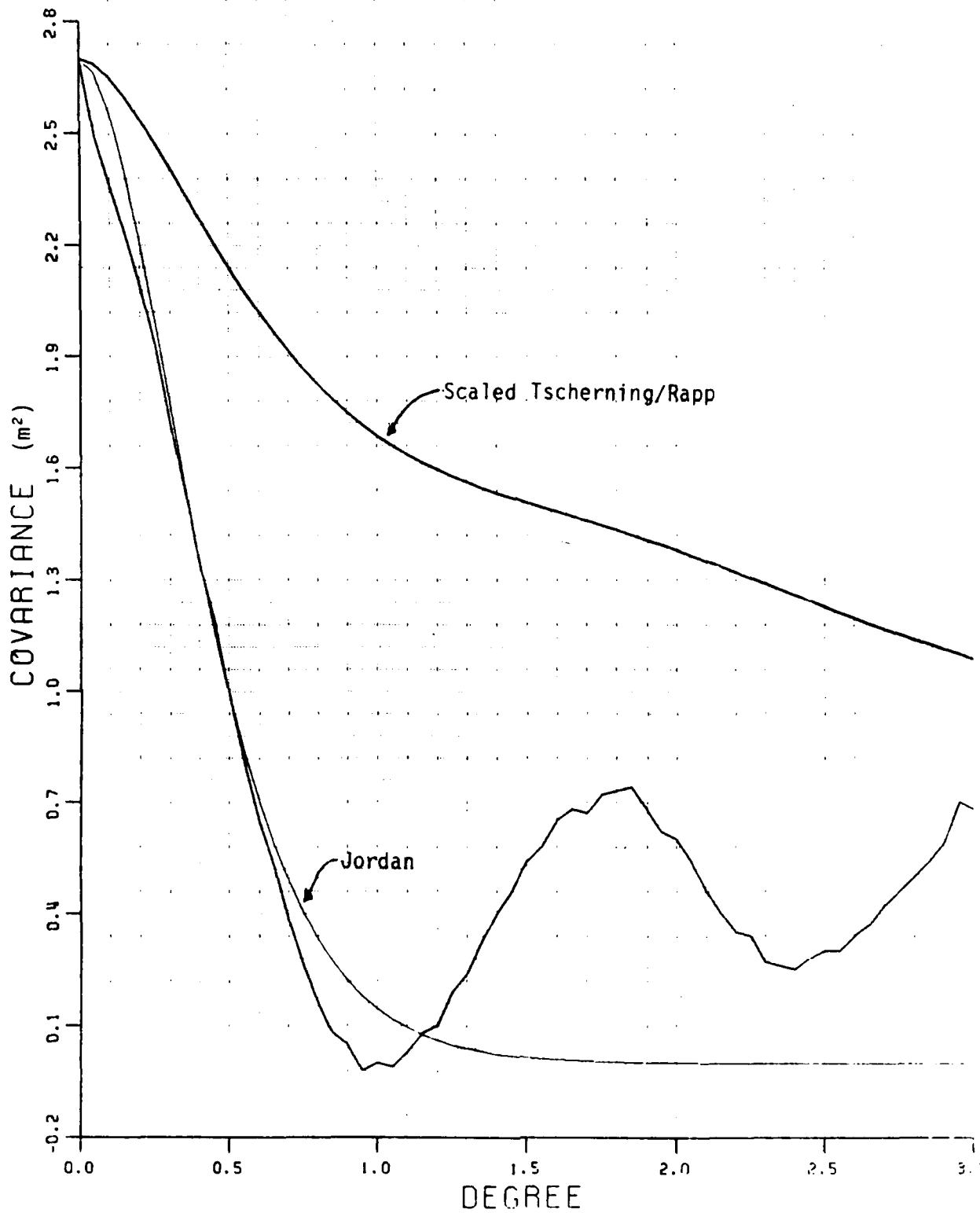


Figure 7  
 Empirical and Model Geoid Undulation Covariances in the Puerto Rico Trench Area (OSU 180 reference)

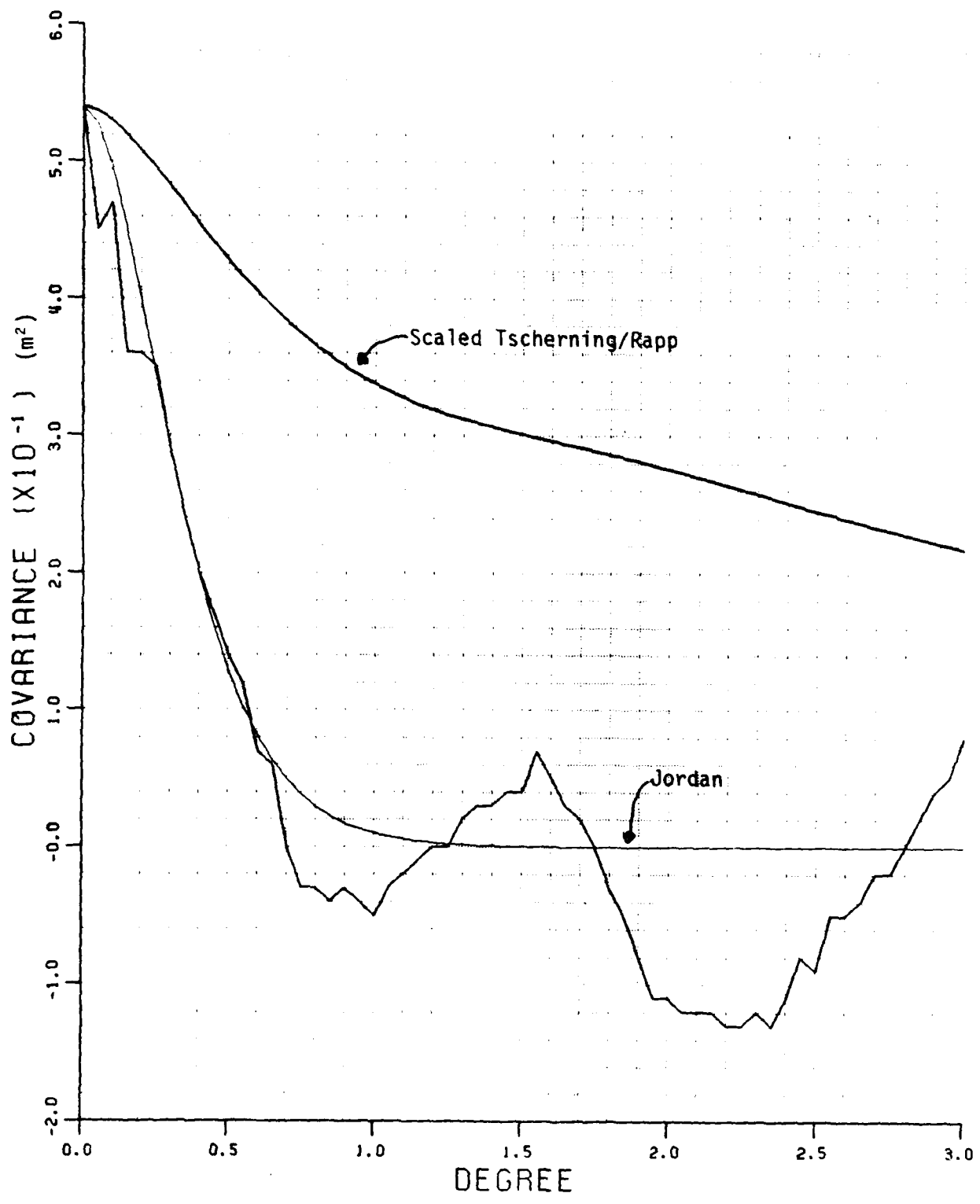


Figure 8  
 Empirical and Model Geoid Undulation Covariances in the Louisville Ridge Area  
 (OSU 180 reference)

Table 1  
 $C(N_p, \Delta g_Q)$ , mgal/m  
 OSU180 Reference  
 Jordan Model

D°	Puerto Rico Trench Area	North Sea Area
0.120	94mgal/m	12mgal/m
0.133	85	
0.200	57	7
0.400	28	3.5
0.600	19	2.4
0.800	14	1.8
1.00	11	1.4

The corresponding value of this covariance for the Tscherning/Rapp model was 26mgal/m for the Puerto Rico Trench and 8mgal/m for the North Sea Area.

The large values of  $C(N_p, \Delta g_Q)$  for the Jordan model in the Puerto Rican Trench area implies that an anomaly will be more affected by a given undulation residual than when the Tscherning/Rapp model is used. In order to have the same  $C(N_p, \Delta g_Q, \psi=0)$  for the Jordan and Tscherning/Rapp models the D value would need to be about 0.4 which is twice that found from the actual data.

#### 30'x30' Mean Anomaly Predictions

We first examine the predictions of 30'x30' mean free-air anomalies from our combined Geos-3/Seasat data set. The specific data used was the Geos-3 data that was adjusted to the Seasat data as described by Liang(1983).

The primary purpose of the tests was to see the effect of using the GEM9 and OSU180 reference fields, and to see the effect of scaling the covariance functions to the local area instead of using a uniform global covariance function. Unless otherwise noted, the covariance function is that of Tscherning/Rapp.

#### Japan Trench Predictions and Comparisons

The area of prediction was as follows:  $25^{\circ}42'N, 142^{\circ}40'W$  to  $26^{\circ}00'N, 143^{\circ}00'W$ . This was a  $4^{\circ}x4^{\circ}$  area containing 64  $0.5^{\circ}x0.5^{\circ}$  blocks. The terrestrial data used for the comparison was computed from  $10'x10'$  averages provided by Ganeko (private communication, 1982) and described in Ganeko(1983). The root mean square free-air anomaly in the area is 94mgals.

The predictions were made using the collocation procedure represented by equation (1). The number of altimeter observations used was approximately 420. A single set of such observations was used to predict the mean anomalies

in a area whose maximum size was 4°x4°. The results of this comparison of these values to the terrestrial data is given in Table 2.

Table 2  
Comparison of Terrestrial and  
Altimeter Derived 30"x30" Anomalies  
in the Japan Trench Area  
(mgals)

Reference Field	Covariance	Mean Diff*	RMS Diff
GEM9	Global	0.7	±15.5
OSU180	Global	-1.0	16.0
GEM9	Local	1.0	15.2

\* (alt-ter)

The predicted accuracy (from equation (2)) of the predicted anomalies varied from 9 to 21 mgals with the GEM9, local covariance prediction. This agrees quite well with the RMS differences or comparisons with the terrestrial data. The RMS difference between the two global predictions was ±4.6 mgals so that the use of two very different reference fields had only a minor effect on the results.

#### Puerto Rico Trench Predictions and Comparisons

This area of predictions was as follows: 19°40'N-21°29'N; 293°40'W-297°W. This was a 2°x4° area containing 32 0.5° blocks.

The terrestrial estimates were made using ship gravity data provided by Watts (private communication, 1982). This data was not adjusted by us for crossover discrepancies. The 0.5° predictions were made using the collocation procedure with GEM9 as a reference field. The predicted accuracies of the terrestrial 0.5° blocks from equation (2) varied from 19 to 46 mgals with an RMS of ± 30 mgals. Improved estimates could be obtained by removing ship gravity bias and drift terms. The root mean square anomaly in this area is ±156 mgals. The results of the comparisons of various altimeter derived solutions to the terrestrial data are given in Table 3.

Table 3  
Comparison of Terrestrial and Altimeter  
Derived 30'x30' Anomalies in the  
Puerto Rico Trench Area  
(mgals)

Reference Field	Covariance	Mean Diff*	RMS diff
GEM9	Global	2.2	±12.6
OSU180	Global	6.6	12.6
GEM9	Local	2.1	12.4

\* (alt-ter)

A second prediction area was chosen in the Puerto Rico Trench area for improved terrestrial predictions considering the correlation of the free-air anomaly and depth. Depth information was obtained at 5'x5' intervals. Liang(1984, private communication) developed four different techniques to incorporate the bathymetry data in the terrestrial prediction. No improvement in the comparison of the terrestrial and the altimeter anomalies was seen when the bathymetry was used. In fact, several of the procedures gave substantially poorer results. In this second PRT region (19°21'N, 293°29'W), the RMS discrepancy with terrestrial data was ±10.4 mgal.

#### Blake Plateau Predictions and Comparisons

The last 30' test area was chosen for its mild anomaly field as opposed to the much rougher fields in the two prior trench areas. Four test regions were used with the terrestrial estimates again provided by Watts data.

The first region was 28°32'N, 284°28'W. The second region was 24°28'N, 284°28'W. The third region was 24°28'N, 290°29'W. The fourth region was 24°27'N, 290°29'W. The RMS anomaly in this region was on the order of ±35 mgals, with the average predicted accuracy of the altimeter derived mean anomalies ±4 mgals. The results of the comparisons are shown in Table 4.

The tests described in the above sections indicate the ability of the satellite altimeter data to resolve 30'x30' anomalies. The accuracy of the determination in rough areas will be on the order of ±10 to 15 mgals while in smoother areas it will be on the order of ±5 mgal. Our predictions agree well with the terrestrial data considering the accuracy of the data.

Table 4  
Comparison of Terrestrial and Altimeter  
Derived 30'x30' Anomalies in the  
Blake Plateau Area  
(mgals)

Region	Reference Field	Covariance	Mean Diff	RMS Diff
I	GEM9	Global	5.4	±9.1
I	GEM9	Local	5.4	8.0
II	GEM9	Local	2.0	7.1
III	GEM9	Local	-2.0	5.5
IV	GEM9	Local	1.5	5.5

### Point Anomaly Predictions-Preliminary Tests

We now turn to the prediction of gravity anomalies at specific points for comparison with ship data. Such tests have been performed earlier (Rapp, 1979b, Figure 14) but the tests to be described here will be more comprehensive.

The first test was to take a ship gravity profile as provided by Watts and calculate the altimeter derived anomaly using a Geos-3/Seasat data base. The profile was designated as V2901 and was used for earlier tests (Rapp, 1979b). The profile crosses the 90° East Ridge in the Indian Ocean. The ship anomalies are shown as the continuous line in Figure 9. The profile is approximately 1200km long with the center (as plotted) at  $\phi = -6.3^\circ$ ,  $\lambda = 89.4^\circ$ .

The altimeter derived anomalies were computed by T. Engelis. The whole line was divided into 9 segments with altimeter data selected for each segment. The data was then used in equation (1) to predict 8 points on the profile segment. For these predictions the GEM9 reference field was used. A 3° data border was used with a maximum of 420 altimeter points selected for each prediction segment. This data was selected to be denser near ( $<1^\circ$ ) the line segment and less dense farther away. The mean difference (Watts-altimeter) was 2.1 mgals, with a root mean square difference of  $\pm 9.1$  mgal. Although this is a good agreement between the two data sets, it is clear from Figure 9 that there is more high frequency information in the ship data. If more profiles were computed, power spectral analysis of the two data sources could be carried out as was done by Eren (1980) when Geos-3 data alone was used for these types of computations.

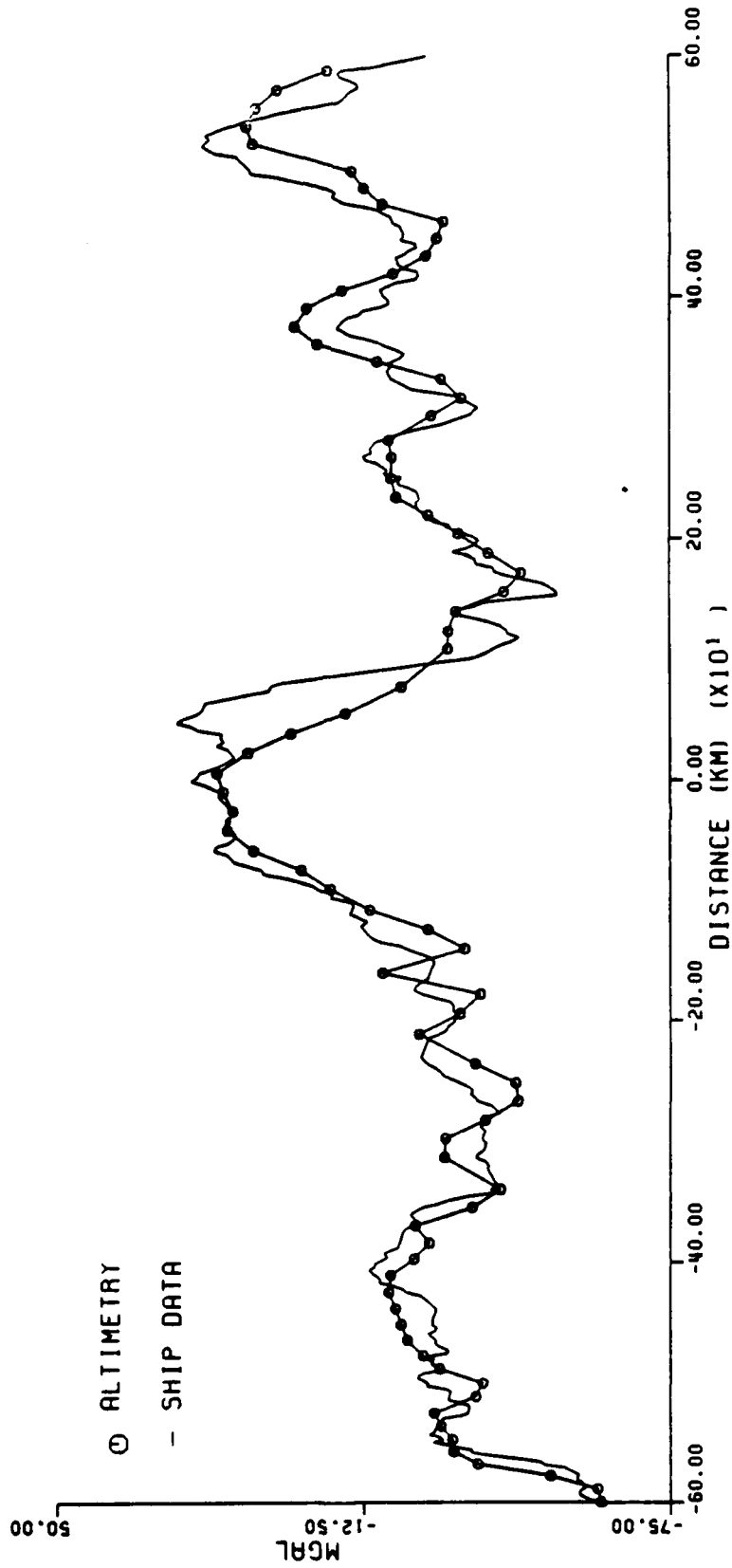


Figure 9  
Ship and Altimeter (GS/SS) Gravity Data Across the 90° East Ridge



We next turn to a sequence of tests to better define the prediction techniques for point gravity anomalies now to be computed on a grid of  $\theta \times \theta$ . In these tests we were specifically interested in a.) the  $\theta$  size to be used with one data selection and matrix inversion and b.) the covariance model (Tscherning/Rapp or Jordan) to be used in the prediction. The first test area was a  $1 \times 1$  area in the Indian Ocean where good ship data was available. The data was used to compute a  $10' \times 10'$  or  $20' \times 20'$  grid ( $\phi = -11.8^\circ$ ,  $\lambda = 88.2^\circ$ ) of anomalies from the Geos-3/ Seasat data.

Table 5  
Grid Prediction Comparison in an  
Indian Ocean  $1 \times 1$  Block

$\theta$	Data Points	Border	Ref Field	Mean Diff (mgals)	RMS Diff (mgals)
1°	367	3°	GEM9	9.8	$\pm 14.4$
2°	404	1°	OSU180	9.8	14.4
2°	245	1°	OSU180	10.2	15.0
2°	344	0.5°	OSU180	11.1	15.8
2°	225	0.5°	OSU180	11.1	$\pm 15.4$

We see no substantial difference in the results presented in Table 5. Other tests were run with  $\theta$  values of  $3^\circ$  and  $4^\circ$  using a 0.5 border and the OSU 180 reference field. The RMS difference of the common prediction anomalies in the  $2^\circ$ , 404 point case was  $\pm 0.9$  mgal ( $\theta = 3^\circ$ , 370 points);  $\pm 5.0$  mgals ( $\theta = 3^\circ$ , 292 points); and  $\pm 4.5$  mgal ( $\theta = 3^\circ$ , 370 points). We concluded that increasing the value of  $\theta$  had only a marginal effect on the predicted anomalies, being always less than the accuracy of the predicted anomalies.

A second test was run in a region near the Puerto Rico Trench. The southern latitude of this area was  $19.5^\circ$  and the western longitude  $293.5^\circ$ . Anomalies in this area ranged from 40 mgals to -360 mgals. Predictions were made with two reference fields, various prediction block sizes ( $\theta$ ), number of data points and data borders. Comparisons were then made to the grid estimate based on the Watts data. Some of these tests are described in Table 6.

Table 6  
Grid Prediction Comparisons  
in Puerto Rico Test Region One

$\theta^\circ$	Data Points	Border	Ref Field	Mean Diff (mgals)	RMS Diff (mgals)
1°	449	3°	GEM9	-0.5	±24
1°	449	3°	OSU180	-0.4	±20
1°	260	0.5°	OSU180	-3.4	±16
2°	402	0.5°	OSU180	-3.2	±17
2°	271	0.5°	OSU180	-4.9	±16
3°	405	0.5°	OSU180	-6.2	±14
3°	291	0.5°	OSU180	-7.7	±13
3°	411	0.5°	OSU180	-9.6	±17

From these tests we decided that the largest size block in which a grid prediction should be made from one data inversion was 3°. This was used to the selection of the OSU180 field as the reference field, and a 0.5° border of data. The border is taken from the outer edge of the limits of the grid being predicted.

We now moved to test the prediction accuracy in four other areas. The primary intent of this prediction was to consider which covariance function (the Tscherning/Rapp or the Jordan) gave better predictions. In this test the Tscherning/Rapp covariances were scaled such that the undulation variance of the actual data was the same as the model undulation variance. The Jordan parameters were found from the empirical covariances as described in a previous section. The minimum D value accepted was 0.1° (smaller values simply implied an unreasonably large anomaly variance).

For all the following tests the data selection was made so that when using the combined data set an equal (approximately) number of Geos-3 and Seasat observations were used. If this was not done, one would generally get more Geos-3 observations because of their greater density in the areas tested.

The first area in this group test was again the Puerto Rico Trench area. Figure 10 shows the location of the available ship data, and Figure 11 shows the anomaly field based on ship data. The grid interval for Figure 11 and most other maps discussed in the test section was 0.25° (decreasing this spacing to 0.125° increased the computing time by only 5% with some increase in resolution).

The anomaly and undulation predictions were carried out using the procedures described above. The anomaly map, when using the Tscherning/Rapp covariances, is shown in Figure 12. Figure 13 shows the anomaly map with the Jordan covariance function. The geoid undulation map is shown in Figure 14 for reference purpose based on the Tscherning/Rapp model.

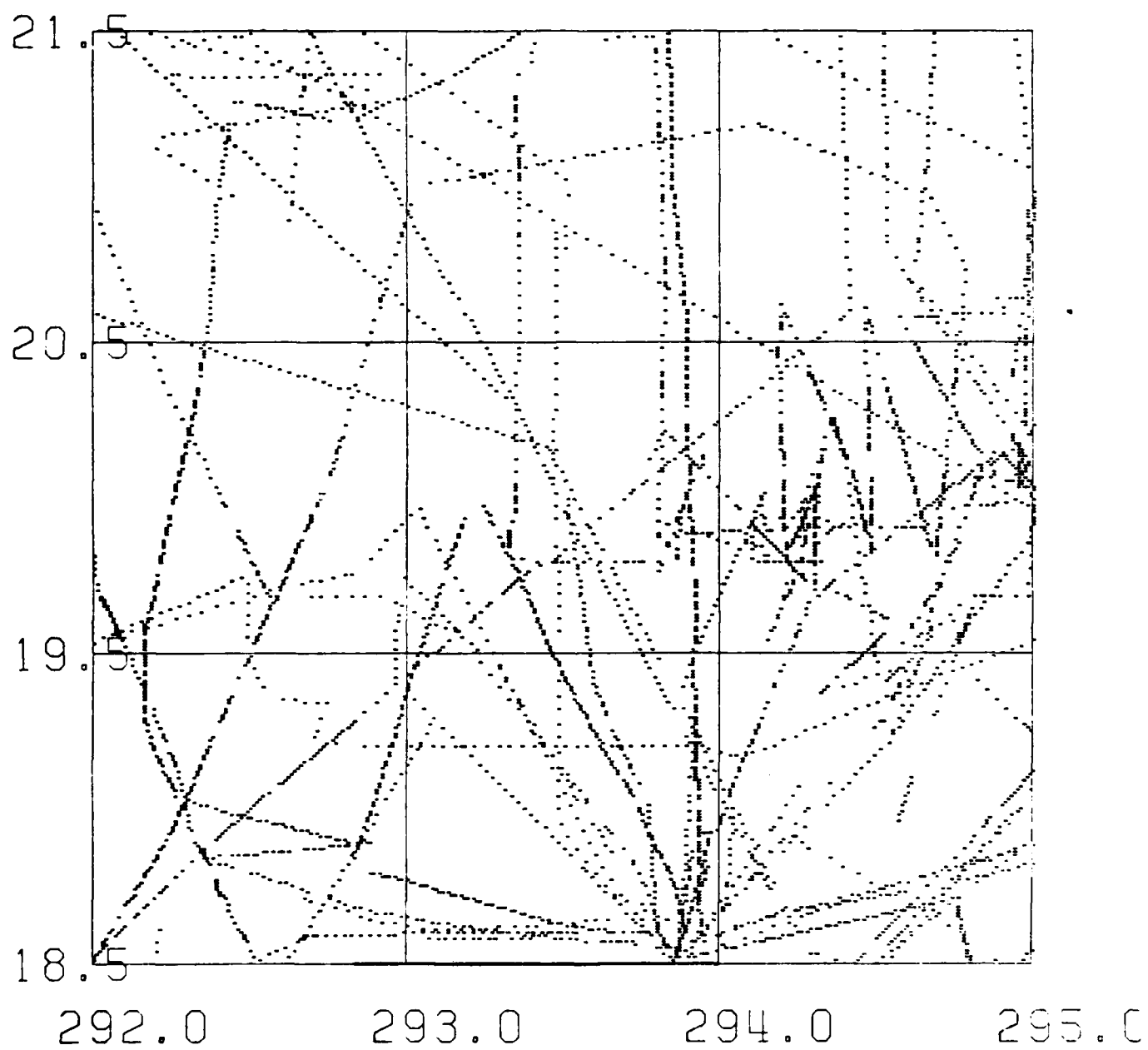


Figure 10  
Ship Gravity Data used in Puerto Rico Trench Area

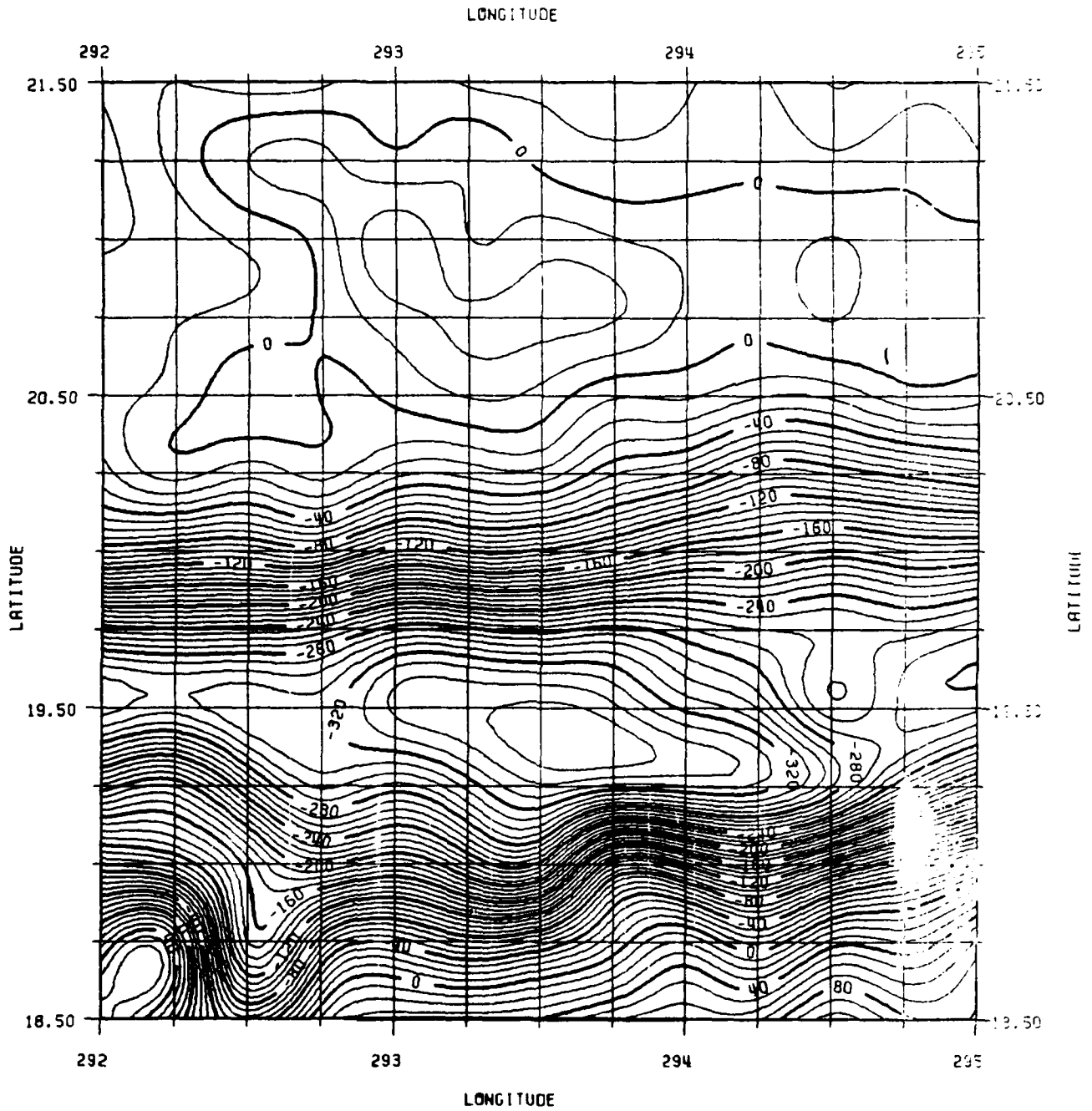
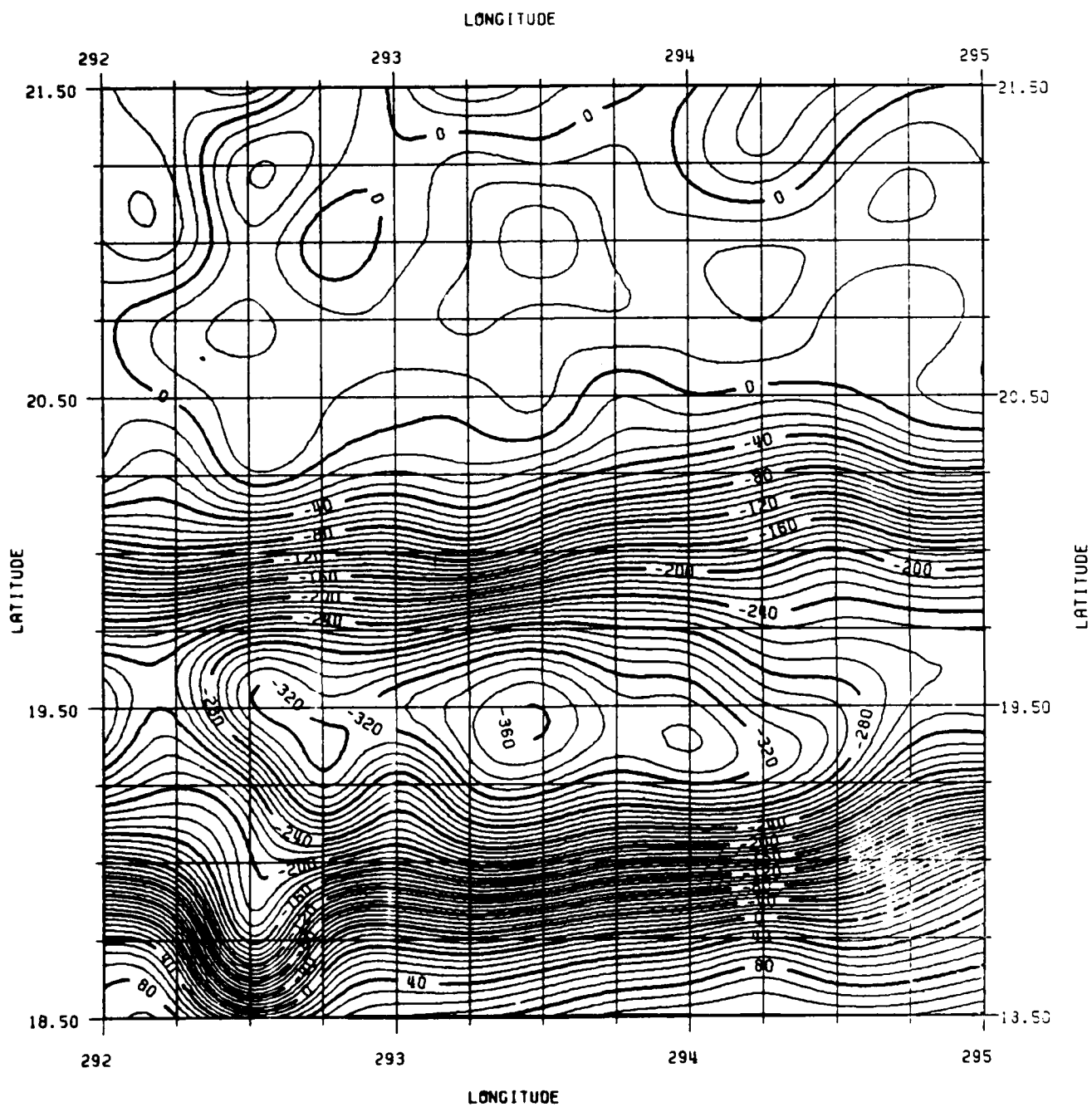


Figure 11  
 Gravity Anomalies in the Puerto Rico Trench Area Based on Ship Data  
 (C.I. = 10 mgals)



**Figure 12**  
**Gravity Anomalies in the Puerto Rico Trench Area from Altimeter Data Using**  
**the Tscherning/Rapp Covariances (C.I. = 10 mgals)**

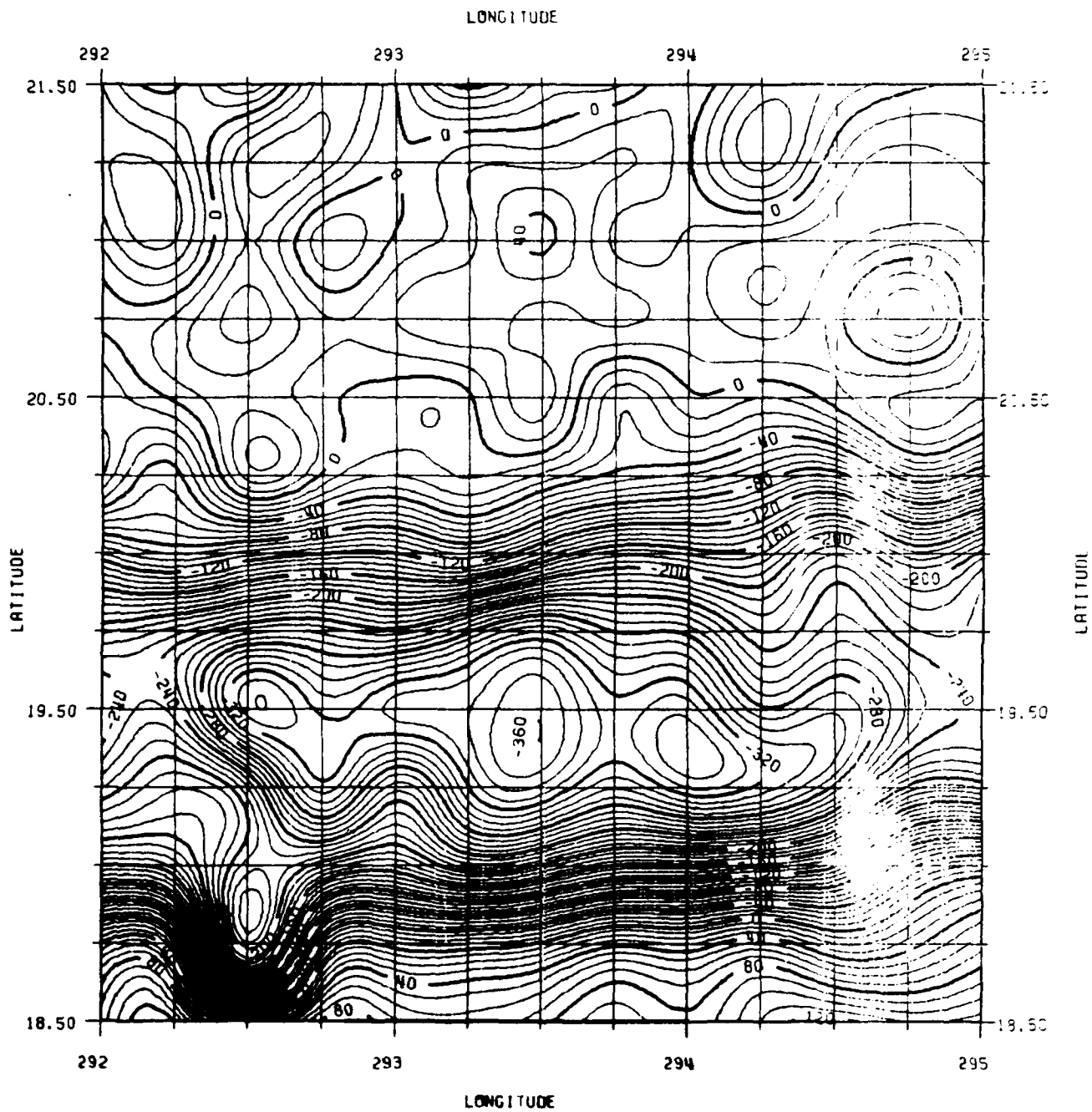


Figure 13  
 Gravity Anomalies in the Puerto Rico Trench Area from Altimeter Data Using  
 the Jordan Covariance Function (C.I. = 10 mgals)

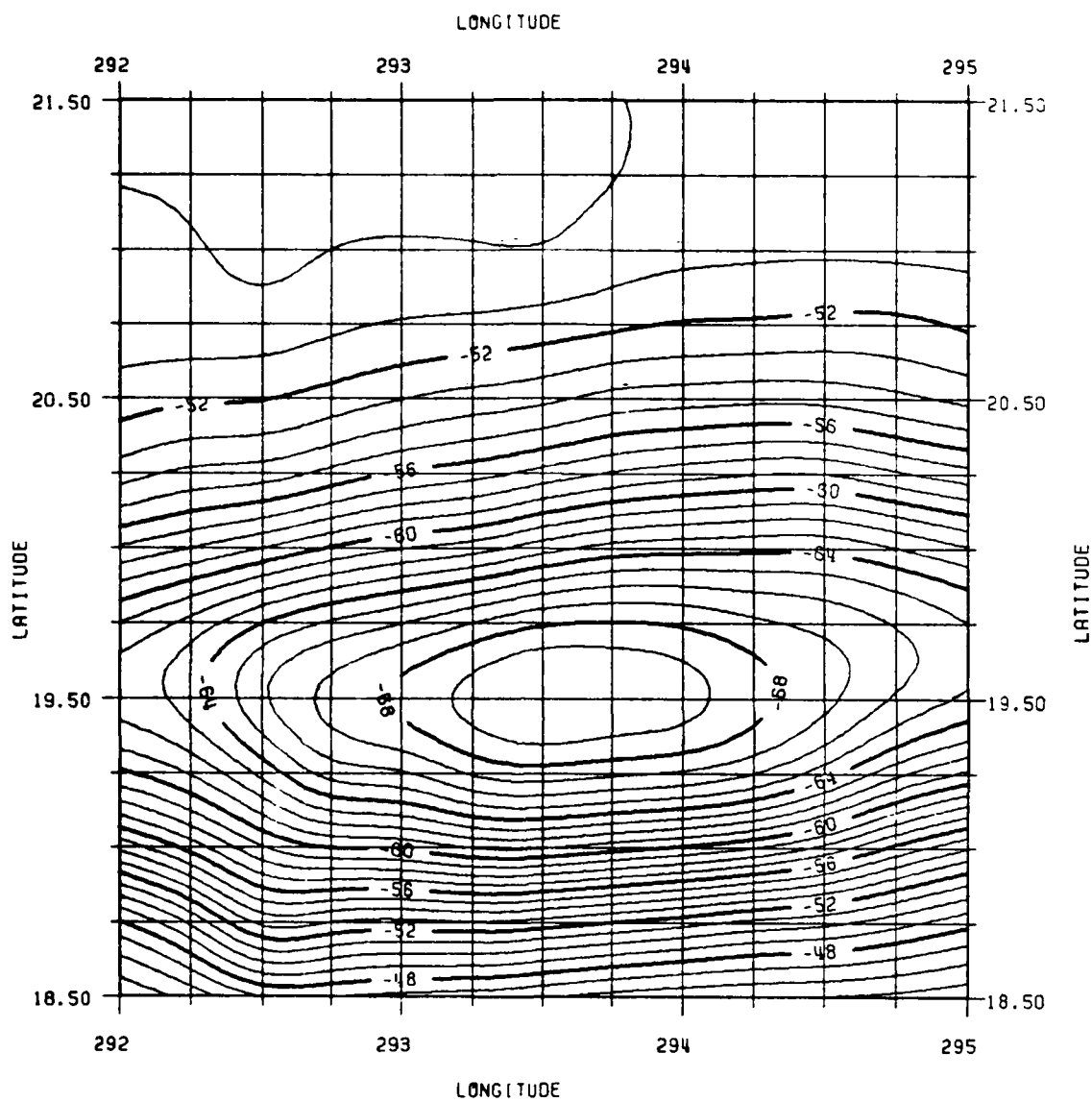


Figure 14  
 Geoid Undulations in the Puerto Rico Trench Area Based on a Combined  
 Geos-3/Seasat Data Set (C.I. = 1 m)

Visual comparison of Figures 12 and 13 shows them to be quite close in form, except for more apparent high frequency information in the northern section when the Jordan model was used. Comparison with Figure 11 (the ship data) shows better agreement with the Tscherning/Rapp map in the sense that the loop seen in the northern part of Figure 13 is not apparent in Figures 11 and 12.

Some statistical comparisons between these data sets are given in Table 7.

Table 7  
Anomaly Comparison in the  
Puerto Rico Trench for Two Covariance models  
(mgals)

	Altimeter Anomalies			
	T/R Covariance		Jordan Covariance	
	Mean Diff	RMS Diff	Mean Diff	RMS Diff
Ship Data	-7.4	±21	-8.7	±27

The result implies that the Tscherning/Rapp model will give better results in the prediction of anomalies although the Jordan model gave a better fit to the empirical covariance functions. The mean difference of about -7mgals may be related to a base station question or most probably to the very large (~-360mgals) of some anomalies in this area.

The geoid undulation from the two predictions were compared with a mean difference of 1 cm and a RMS difference of ±16 cm. A few differences could reach a magnitude of 60 cm. Another test was done in the area restricting the southern latitude limit of the test region to 19.75°. This reduces from the data the very large anomaly fluctuations apparent in Figures 11,12, or 13. In this case the RMS difference (ship vs. altimeter) was ±14 mgals using the Jordan model and ±11 mgals using the Tscherning/Rapp model.



The second main test area for the point predictions was in the Blake Plateau area. Specifically the area in which gridded predictions took place using a uniform Geos-3/Seasat data set, or only Seasat data, was  $28.25^{\circ}\phi\text{--}31^{\circ}; 284^{\circ}\lambda\text{--}286.75^{\circ}$ . Predictions were made using the Watts ship data and the altimeter data with the two covariance models. The results of the comparisons are given in Table 8 for the two cases: the uniform Geos-3/Seasat data and just the Seasat data.

Table 8  
Anomaly Comparisons in the Blake Plateau  
Region for Two Covariance Models  
(mgals)

Data	Altimeter Anomalies			
	T/R Covariance		Jordan Covariance	
	Mean Diff	RMS Diff	Mean Diff	RMS Diff
Geos-3/Seasat	-6.0	$\pm 14.3$	-6.8	$\pm 18.3$
Seasat Only	-6.5	$\pm 13.5$	-6.7	$\pm 15.5$

The results show that the Tscherning/Rapp function gives better results than the Jordan function. The use of the Seasat data above also yields slightly better results than the combined data set. The anomalies implied by the Geos-3/Seasat data are shown in Figure 15 for the Tscherning/Rapp covariance function and Figure 16 for the Jordan function. The maps are quite similar but the one with the Jordan function appears somewhat rougher. The maximum discrepancy of the altimeter and ship data is on the order of 30 mgals and occurs in an area ( $\phi=30^{\circ}, \lambda=284^{\circ}$ ) where the altimeter data is quite sparse.

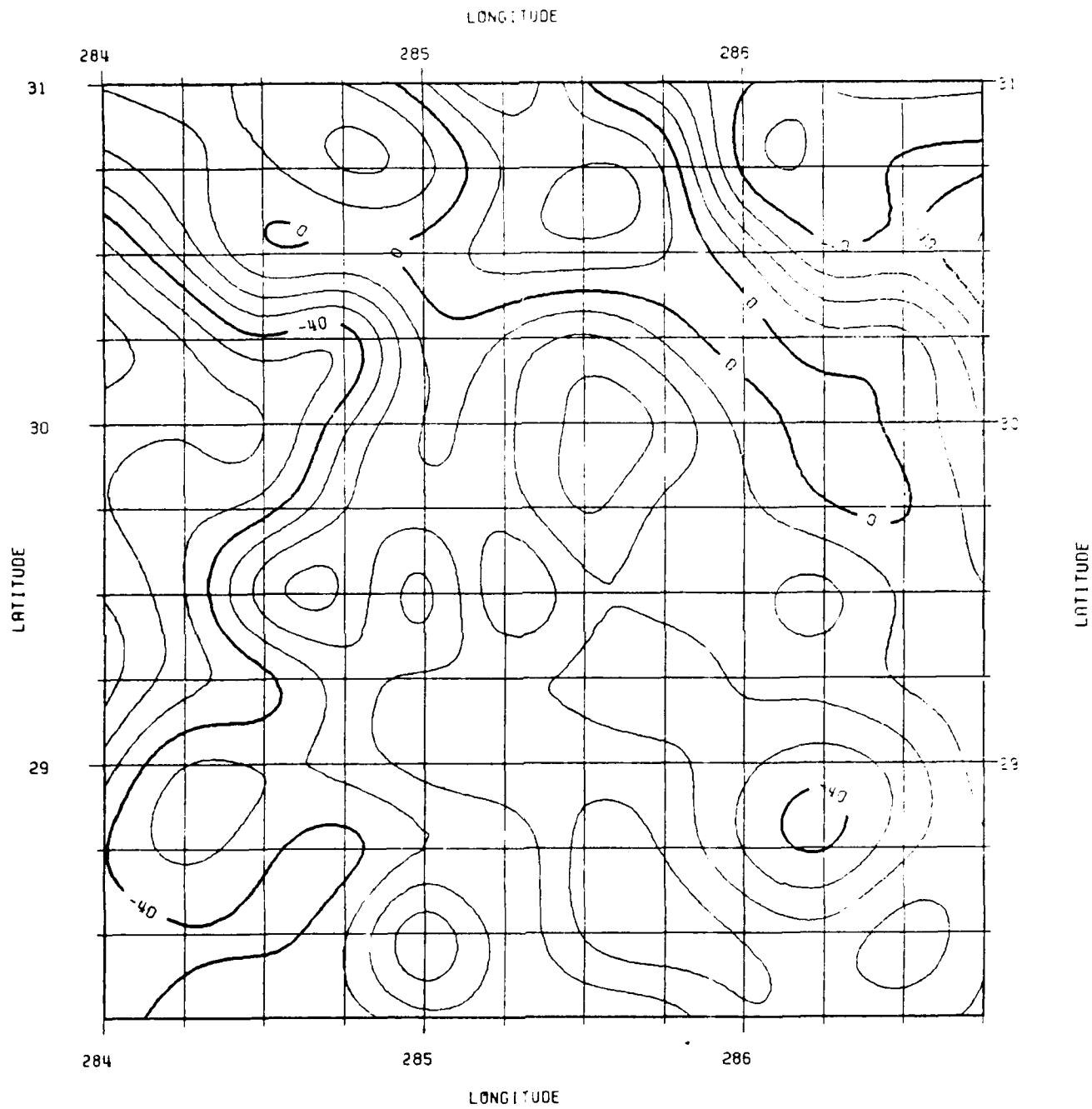


Figure 15  
 Gravity Anomalies in the Blake Plateau Region From Altimeter Data Using the  
 Tscherning/Rapp Covariance (C.I. = 10 mgals)

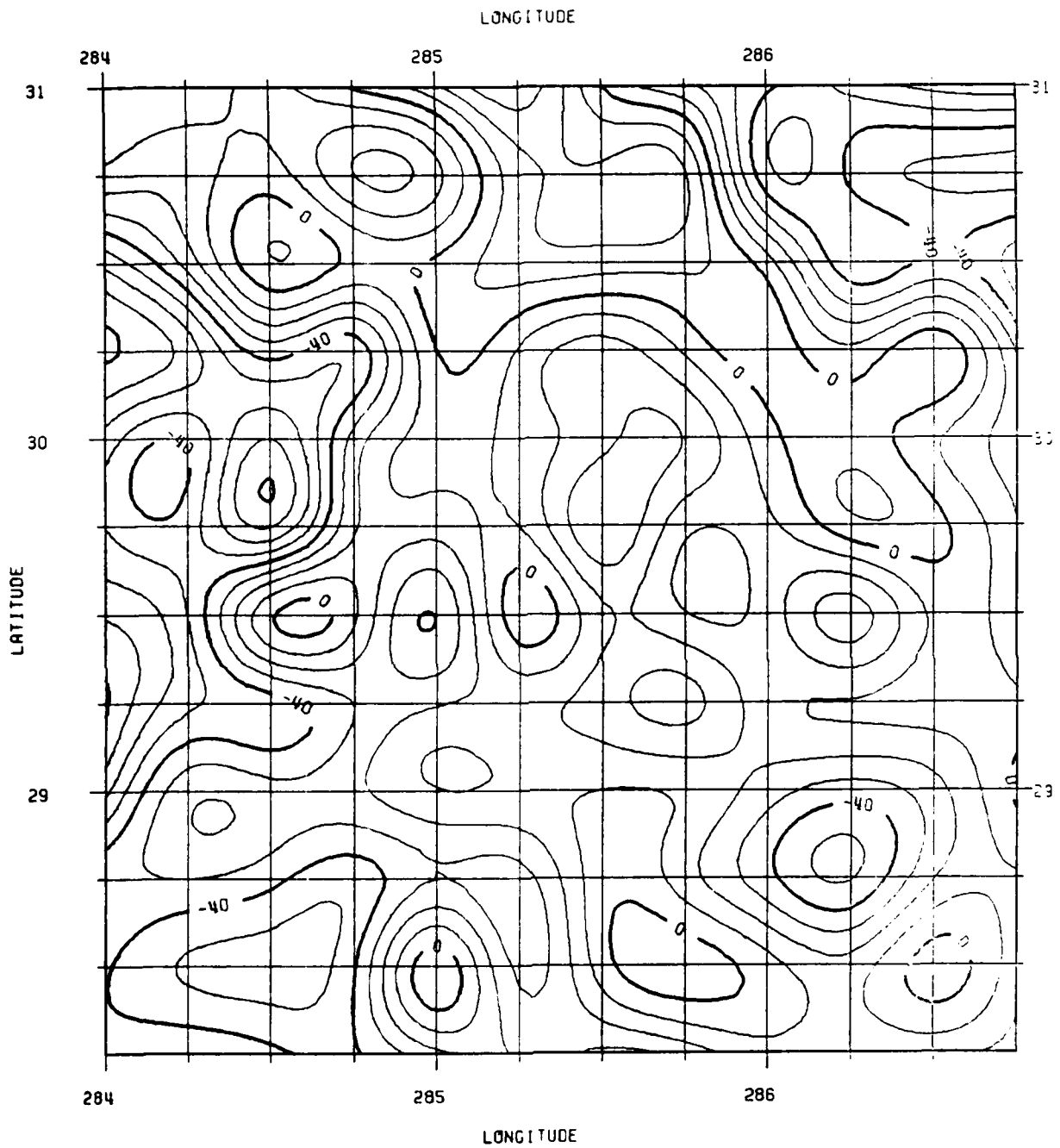


Figure 16  
Gravity Anomalies in Blake Plateau Region  
From Altimeter Data Using the  
Jordan Covariance (C.I.=10mgals)

The agreement of the altimeter derived anomalies and the ship data could perhaps be improved if the crossover discrepancies in the ship gravity tracks were removed. In a number of cases these discrepancies could reach 20 mgals.

The third area in which point anomaly predictions were tested was the North Sea. Our selection of this area was based on the altimeter/anomaly study carried out by Brenneke and Lelgemann(1983) and the terrestrial data that was available in the form of 6'x10' mean anomalies as described by Torge, Weber, and Wenzel(1983). The first step here was to compute a "point" 0.25° data grid from the Torge et al data. The predictions were done regarding the 6'x10' as point values and using a scaled covariance function. The predicted accuracy of the values is on the order of ±7 mgals.

The specific region in which the predictions took place was 45°N-60°N; 0°E-6°E. The predictions were done at one time for four 3°x3° areas. Both uniform Geos-3/Seasat and just Seasat data were used with the two covariance functions. Statistics on the comparisons of the 576 predicted anomalies to the terrestrial data set are given in Table 9.

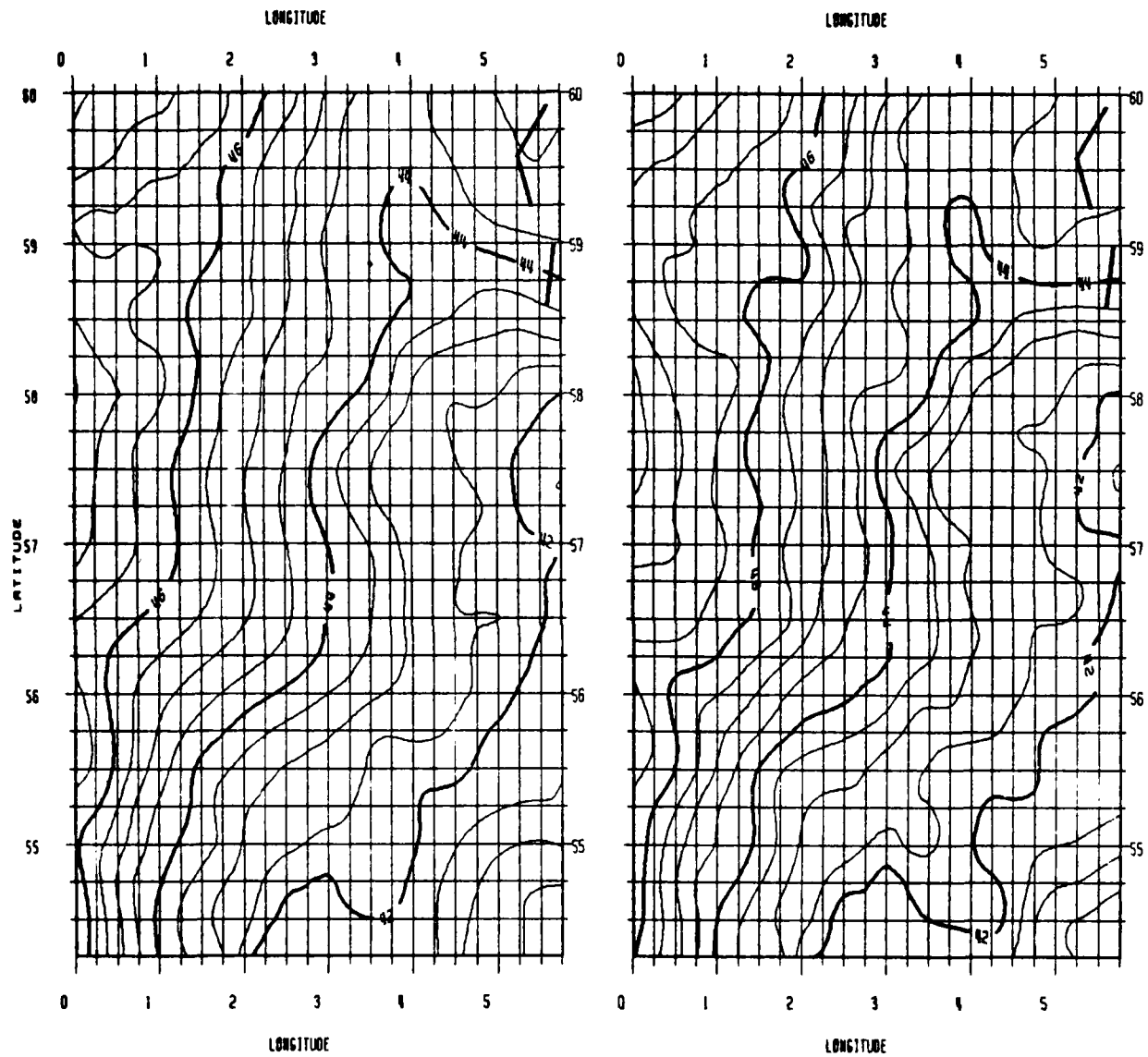
Table 9  
Anomaly Comparisons in the North Sea Area  
for Two Covariance Models  
(mgals<sup>2</sup>)

Data	Altimeter Anomalies			
	T/R Covariances		Jordan Covariances	
	Mean Diff	RMS Diff	Mean Diff	RMS Diff
Geos-3/Seasat	0.9	±11.5	1.2	±13.4
Seasat Only	1.1	± 9.4	1.6	± 9.8

From this table it appears that the scaled Tscherning/Rapp covariance function yields better results with a given data set. We also see that the Seasat data alone gives better results in this area than using the combined data set. This implies that the Geos-3 may not be properly adjusted or sufficiently accurate in this somewhat restricted region.

To examine this question further we show in Figure 17 the geoid undulations from the Seasat data alone and from the combined Geos-3 data set using the Tscherning/Rapp covariance model.

Although quite similar in appearance, the geoid undulations from the combined Geos-3/Seasat data appear more irregular than the Seasat alone plot. Maps made just with the Geos-3 data were more irregular and reflect the larger crossover discrepancy that exists with the Geos-3 data. The mean difference and RMS difference between the undulations from Seasat alone, and



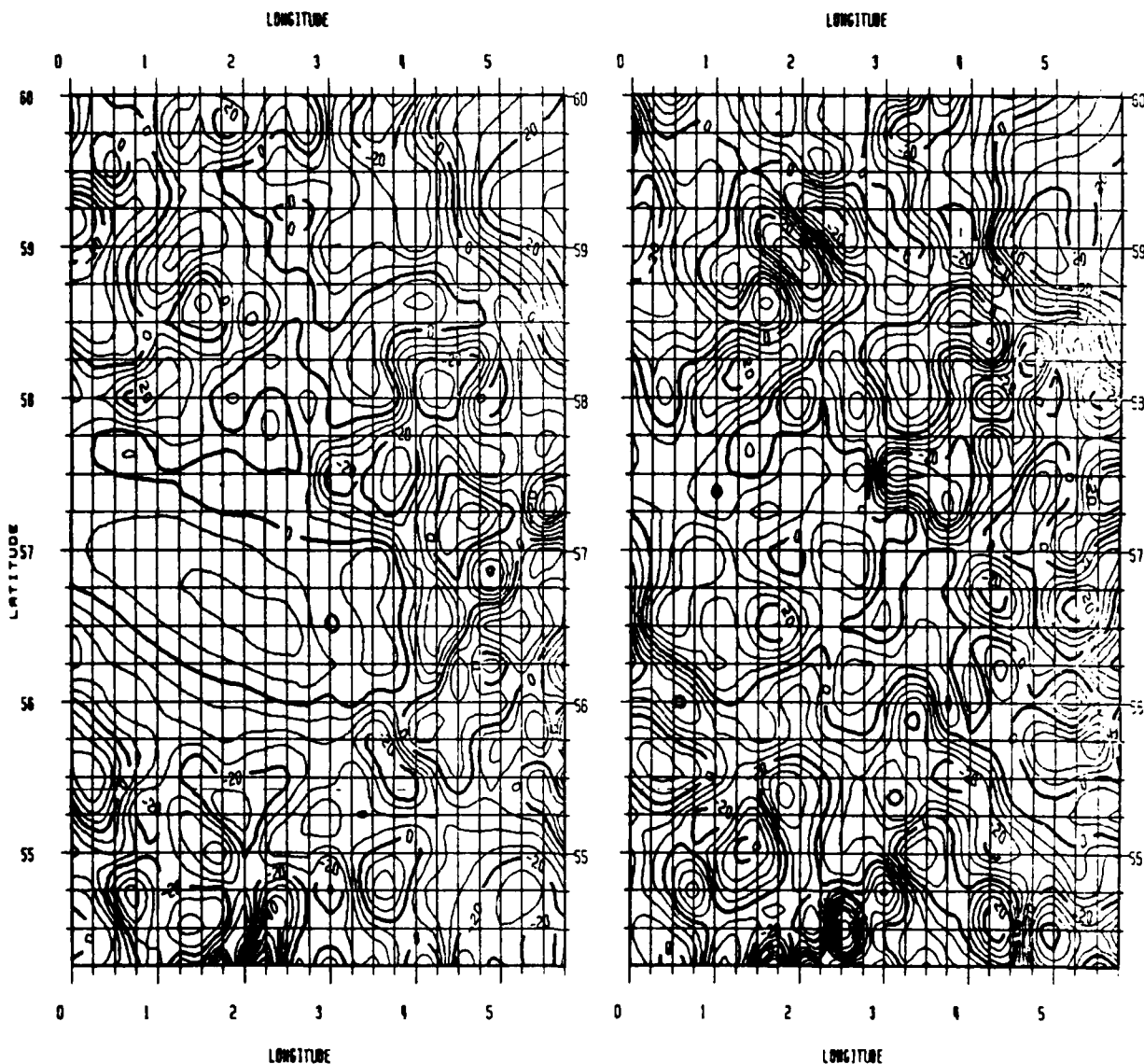
Seasat Only

Combined Geos-3/Seasat

Figure 17  
 Geoid Undulations in the North Sea Area  
 (Contour Interval = 0.5 m)

from the combined data set is  $-9\text{cm}$  and  $\pm 19\text{cm}$ . The mean and RMS difference between predictions using the Geos-3/Seasat data set with the two different covariance function is  $1\text{cm}$  and  $\pm 7\text{cm}$ .

The gravity anomalies for this area are shown in Figure 18 for the Seasat alone and the combined Geos-3/Seasat data using the Tscherning/Rapp covariances.



Seasat Only

Combined Geos-3/Seasat

Figure 18  
Gravity Anomalies in the North Sea Area  
From Alimeter Data  
(Contour Interval = 5mgals)

These tests in the North Sea area show that one must treat the combined altimeter data set with care as the use of the Seasat data alone gave better results than the combined set. Unfortunately it seems to be apparent from the contour maps that undesirable noise is present in the solution. The problem most probably relates to the reduction and adjustment of the altimeter data, especially for the short Geos-3 arcs in a region with only data on one side (that is, there is no substantial altimeter data to the east of the North Sea).

We now turn to our last test area which is off the coast of southern California. The terrestrial gravity data has been taken from a 5 mgal contour interval map prepared by Beyer et. al. (1974). The specific limits of the area in which the anomalies were predicted was  $32^{\circ}00' \leq \lambda \leq 33^{\circ}75'$ ;  $239^{\circ} \leq \phi \leq 241^{\circ}$ . The data from the map was digitized on a  $0.125^{\circ}$  grid. The terrestrial map is shown in Figure 19. There are rapid variations of the anomalies in several portions of this area with much high frequency information present in the data.

The altimeter anomaly predictions were made on a  $0.125^{\circ}$  grid to match that used in the terrestrial estimation. The anomaly map based on the Tscherning/Rapp covariance function with the uniform Geos-3/Seasat data is shown in Figure 20. It is clear that much high frequency gravity information is missing although the general structure of the field is the same. The comparison of the terrestrial altimeter derived anomalies is given in Table 10.

Table 10  
Anomaly Comparisons off the Coast of  
California for Two Covariance Models  
(mgals<sup>2</sup>)

Data	Altimeter Anomalies			
	T/R Covariances		Jordan Covariances	
	Mean Diff	RMS Diff	Mean Diff	RMS Diff
Geos-3/Seasat	-0.6	$\pm 19.7$	-0.2	$\pm 18.8$

The results in this table are the poorest of all our previous tests. It may be related to the high frequency anomaly field in the area, or it may be related to a poor sea surface due to the area being at the edge of the coast. However a geoid undulation map does not reveal any significant irregularities.

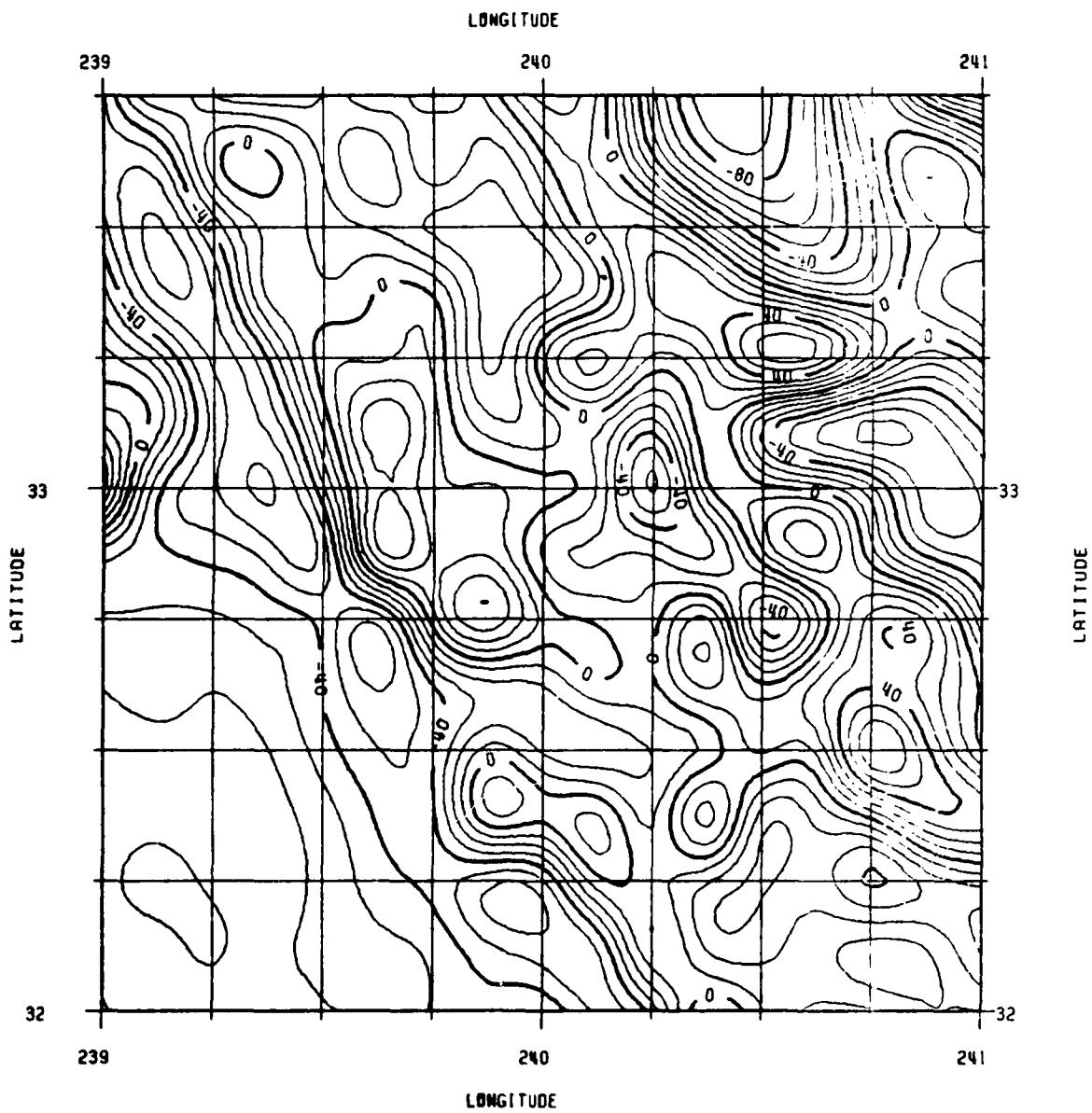


Figure 19  
 Terrestrial Free-Air Anomalies Off Southern California Based on Beyer et al  
 (1974) (C.I. = 10 mgal)



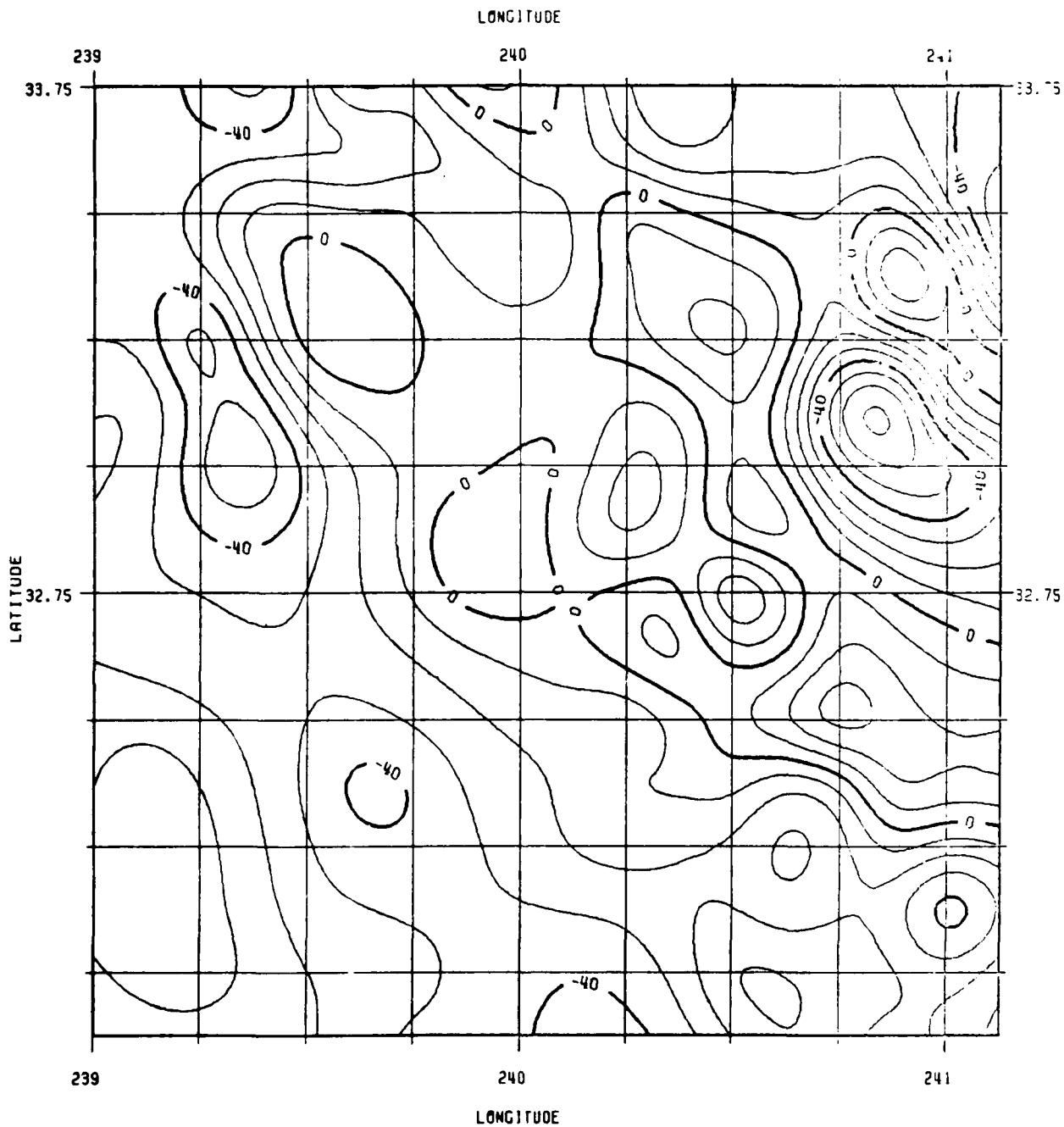


Figure 20  
Gravity Anomalies of the Coast of California From Altimeter Data (C.I. = 10 mgal)

### The Accuracy Computations

The accuracy of the predictions is computed from equation (2). The actual value depends on the data distribution, data noise, and the scale of magnitude of the covariances. We will scale our covariance functions from area to area to match model variance with actual variance (e.g. for residual geoid undulations). These values vary considerably from region to region so that with the same data one might have predicted accuracies that could range from  $\pm 10$  mgals to  $\pm 50$  mgals. It is therefore difficult to interpret the accuracy estimates from equation (2) in a global sense because of the way in which we scale our covariance functions. Within a specific area, computed with the same covariance function, the accuracy estimates can effect the relative accuracy of the predicted quantity.

The computation of the accuracy causes a substantial computational effort over that if just a prediction were done. To see this let's write (1) and (2) in the following form:

$$\Delta g = \underline{C}_{gh} \cdot A + \Delta g_R \quad (15)$$

where:

$$A = (\underline{C}_{hh} + D)^{-1} (h - h_R)$$

Given a data set, the vector A can be evaluated once before any prediction actually takes place. The predictions then go quite fast because each prediction is made as the product of two vectors.

Unfortunately, such a modification of (2) is not possible because the  $\underline{C}_{gh}$  vector depends on the location of the point to be predicted. In our past computations we have computed both  $\Delta g$  and  $m^2 g$  by writing (1) and (2) in the form:

$$\Delta g = B(h - h_R) + \Delta g_R \quad (16)$$

$$m^2 g = \underline{C}_{gg} - B\underline{C}_{hg} \quad (17)$$

where:

$$B = \underline{C}_{gh} (\underline{C}_{hh} + D)^{-1} \quad (18)$$

B must be computed for each prediction point although the matrix inversion need only be done once for a given data array.

If the accuracy estimate is not computed, the calculations of the gravity anomaly is about eight times faster than the calculations of both quantities. If a vector processing computer were available this accuracy estimate penalty could be substantially reduced.

It is possible to obtain an approximate accuracy estimate by considering values rigorously computed with a specific covariance function and then scaling this result to another area knowing the relationship in the variance of the covariance functions.

A number of tests were made computing the formal accuracy of the predicted anomalies. The average accuracy of a predicted anomaly was  $\pm 23$ mgal when the residual anomaly variance was  $1150.14 \text{mgal}^2$ . The average accuracy of a predicted geoid undulation was  $\pm 0.2$ m when the residual undulation variance was  $1.60 \text{m}^2$ . For our prediction computation we computed the scaled accuracy estimate for each region which was assigned to be the same for each point predicted in the region. Specifically we used the following:

$$m(\Delta g)_c = 23 \left[ \frac{1150.14}{C_o(\Delta g_i)} \right]^{1/2} \quad \text{mgals} \quad (19)$$

$$m(N)_i = 0.2 \left[ \frac{1.60}{C_o(\Delta N_i)} \right]^{1/2} \quad \text{meters} \quad (20)$$

A disadvantage of this procedure is that we are not able to recognize poor predictions caused by the lack of altimeter data in a portion of a region.

Another way will be sought by examination of the actual numbers (or count) of the altimeter in geographic cells. Specific details are found in another section.

### The Choice for Prediction Runs

There are a number of decisions to be made when choosing the final prediction procedures. Our tests described in the previous section have been described to indicate which variables should be selected. We choose the following:

Reference Field: OSU 180x180 (1981)  
 Covariance Function: Scaled Tscherning/Rapp  
 Block Size:  $3^\circ \times 3^\circ$  (for one matrix inversion)  
 Data Number: Approximately 300 points  
 Data Border:  $0.5^\circ$  about block border  
 Grid Interval:  $0.125^\circ$

The grid interval for the predictions made for most of the tests previously described was  $0.25^\circ$ . However, decreasing this interval to  $0.125^\circ$  only causes about a 5% increase in the computer time, so that the smaller interval was selected although it may not be justified on the basis of the spectral content of the data. This will be discussed later in the report.

## The Satellite Altimeter Data Set

The first global gravity field analysis that we did with altimeter data was with Geos-3 data (Rapp, 1979b). The second global analysis was done with the Seasat data (Rapp, 1982, 1983a). The gravity anomaly recovery from the Seasat data described in Rapp (1983) was slightly flawed in parts of the Pacific because some long arcs were not properly adjusted in our crossing arc adjustment. An improved Seasat adjustment was carried out in 1982 by Jaime Cruz. This second general adjustment eliminated most of the problem that existed in the first adjustment. The wide areas of large crossover discrepancies that existed in the Pacific now had disappeared (Rapp, 1982, Figure 3) although there were a few areas where track dependent patterns were still visible. The location of the Seasat data that was available from this second crossing arc adjustment is shown in Figure 21.

In September 1981 we received from NOAA a revised Geos-3 data set that was acquired over a 3.5 year period. The original data set included 10,520 arcs starting from April 1975 and extending to December 1978. For improved gravity field work this data base was adjusted (using the crossing arc technique) to the Seasat primary arcs that were initially used by Rowlands (1981) in our first Seasat adjustment and then by Cruz in the improved second adjustment. In essence the Seasat primary arcs were held fixed with the Geos-3 arcs receiving bias and tilt correction based on the crossover discrepancies of Geos-3 with the primary Seasat arcs, a primary crossover, and Geos-3 with itself (a local crossover).

This adjustment was complicated by the large amount of Geos-3 data in some areas and by the large number of crossovers in the large time extent data set. To manage this problem, the world was divided into six regions and regional adjustments carried out. The regions were made as large as possible considering the arc lengths and the data density. Although smaller regions could give better data fits, we are concerned that gravity, tide, or other types of signal will be absorbed in the parameter of the adjustment. The distribution of the adjusted arcs in the Geos-3 data base are shown in Figure 22.

The complete details of the combined Geos-3/Seasat adjustment are given by Liang(1983). Before the adjustment of the Geos-3/Seasat data the RMS crossover discrepancy was  $\pm 2.86\text{m}$  (Geos-3/Seasat) and  $\pm 3.25\text{m}$  (Geos-3/Geos-3). After the adjustments the crossover discrepancies were  $\pm 0.40\text{m}$  (Geos-3/Seasat) and  $\pm 0.41$  (Geos-3/Geos-3). These values varied little from region to region. This a-posteriori crossover discrepancy of about  $\pm 40$  cm should be compared to a value of about  $\pm 28$  cm found when just the Seasat data was adjusted.

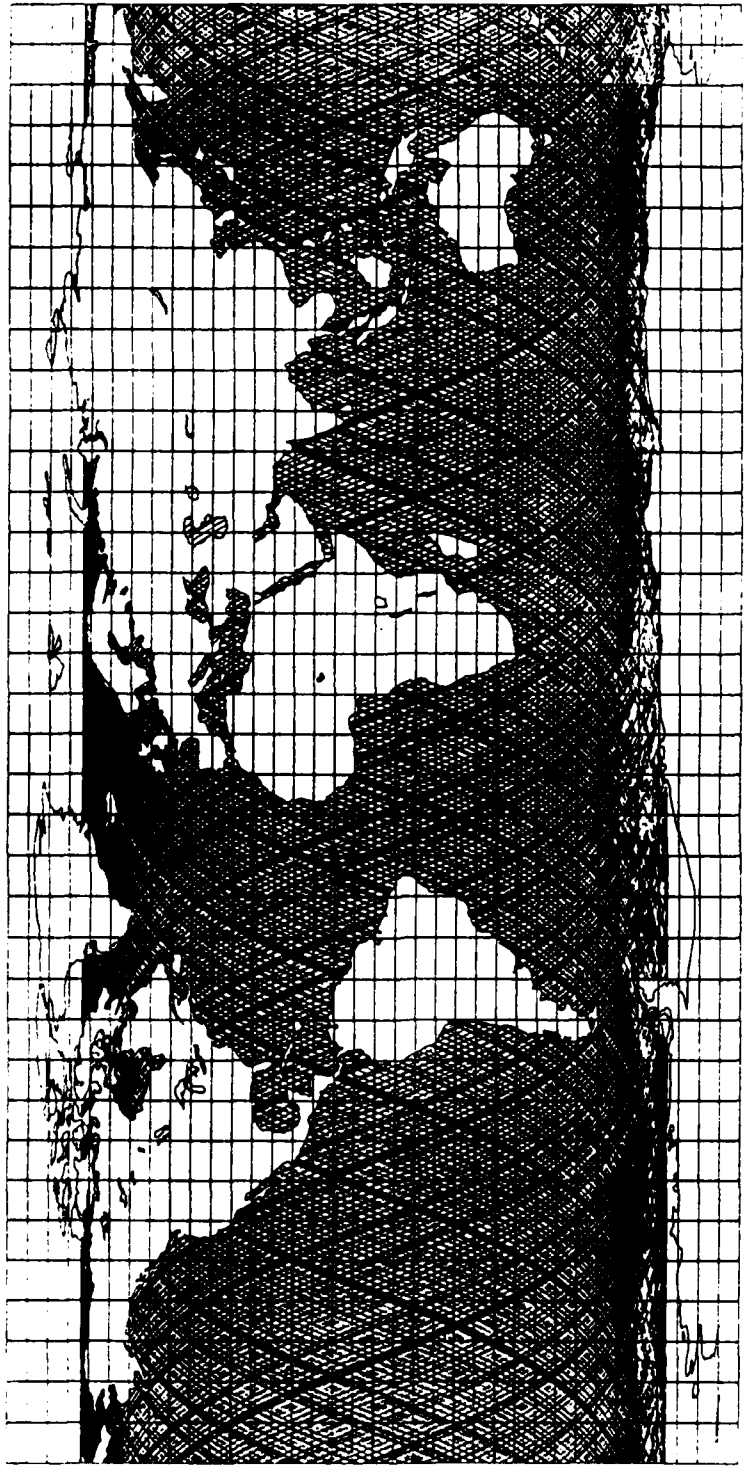


Figure 21  
The Adjusted Seasat Data Base



Figure 22  
Distribution of the Adjusted Arcs From the 3.5 Year GEOS-3 Data

One last modification was made to our primary arc Seasat data base before our final data set was created. Even after our second Seasat adjustment we noticed 53 arcs where the RMS crossover discrepancy was greater than  $\pm 40$  but less than  $\pm 62$  cm. We felt that this larger discrepancy was due to a bias and tilt adjustment being applied to arcs whose length was too long. In order to form as consistent a data base of altimeter data as possible we decided to isolate those primary arcs on an arc by arc basis. The newly adjusted data then replaced the second adjustment sea surface heights. The typical crossover discrepancies of a "bad" arc with other "good" arcs was on the order of  $\pm 36$  cm after the second adjustment. At the completion of the special arc by arc adjustment the new crossover discrepancies for these arcs were on the order of  $\pm 22$  cm, a considerable improvement. A complete discussion of this special arc by arc adjustment was prepared by Liang and is in Appendix A.

At this point the Geos-3 and Seasat data existed on separate tapes and files representing the individual regional adjustment areas. Although close in geographic proximity, the regional adjustment borders did not match between the Geos-3 and Seasat data. For convenience in carrying out our prediction estimation, merged (Geos-3/Seasat) data files were created in convenient geographic blocks. All the altimeter data was referred to an ellipsoid such that  $a=6378136$  m with no sea surface topography corrections being made at this point.

#### Sea Surface Topography Considerations for Production Computations

In an earlier section we described how a sea surface topography model was created for test purposes by interpolation from the Levitus estimate after removal of a mean value. We now consider the determination of sea surface topography from our Seasat altimeter data and the gravity field described by the potential coefficient set of Rapp (1981). A discussion of several estimations of sea surface topography is given in Appendix B prepared by Engelis. In this Appendix an SST data set based on Levitus' oceanographic estimates is described as well as estimates based on using Seasat data and the GEM2 gravity field (Engelis, 1984). In addition a spherical harmonic development to degree 20 of SST is computed combining the Seasat/GEM2 results to degree 6 with coefficients from the harmonic analysis of the Levitus data. We have compared the Levitus estimates (from linear interpolation of values on a  $1^\circ \times 1^\circ$  grid) to estimates from the spherical harmonic expansion to degree 20 of SST, and the estimates from Seasat minus the geoid undulations implied by the 180 spherical harmonic expansion of Rapp (1981). The average values were computed in  $40^\circ \times 30^\circ$  and  $40^\circ \times 40^\circ$  areas. The results are shown in Figure 23.

In some cases the Levitus values agree quite well with those values derived from altimetry and gravity field information. See, for example, the blocks whose northwest corner are:  $0^\circ, 160^\circ\text{W}$ ;  $0^\circ, 4^\circ\text{W}$ ;  $-40^\circ, 169^\circ\text{W}$ ;  $-40^\circ, 120^\circ\text{W}$ ;  $-40^\circ, 80^\circ\text{W}$ ;  $-40^\circ, 40^\circ\text{W}$ ;  $-40^\circ, 0^\circ$ ;  $-40^\circ, 40^\circ$ ;  $-40^\circ, 80^\circ$ ;  $-40^\circ, 120^\circ$ . There are blocks where the agreement is poor:  $40^\circ, 80^\circ\text{W}$ ;  $40^\circ, 40^\circ\text{W}$ ;  $70^\circ, 160^\circ$ ;  $40^\circ, 120^\circ$ ;  $40^\circ, 160^\circ$ . The mean difference and standard deviation between A and B (Levitus) is  $14 \pm 42$  cm. The corresponding values for A and C (the spherical harmonic representation of the SST) is  $17 \pm 15$  cm. A and C agrees better than A and B because C was derived from the Seasat altimeter data.

A = Seasat - Dec81 180 field  
 B = Estimate from Levitus  
 C = Estimate from spherical harmonic expansion to degree 20 from Engelis (Appendix B)

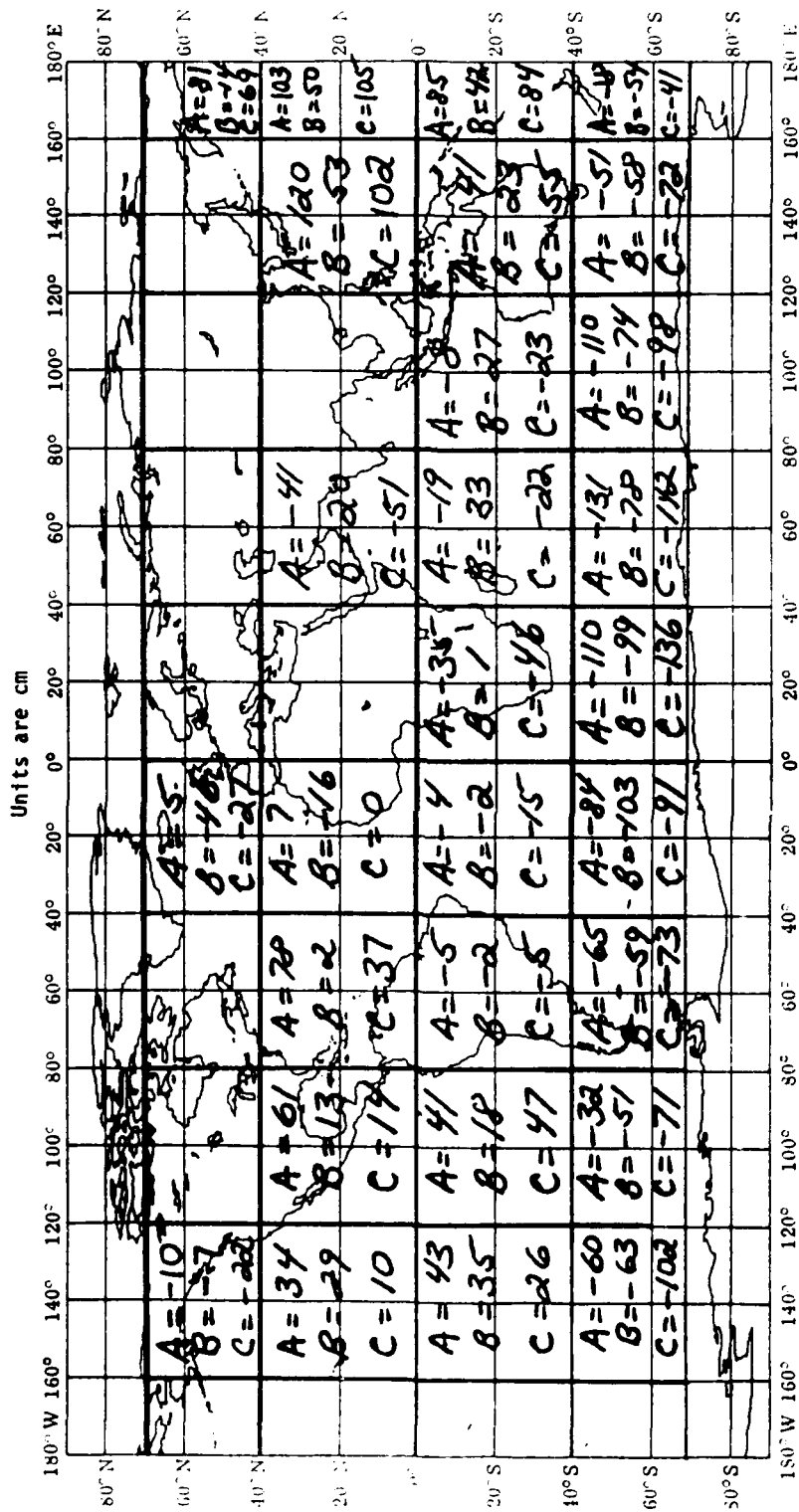


Figure 23  
 Mean Sea Surface Topography Estimates



It is apparent from Figure 23 that the mean sea surface topography effects can be substantial. The most negative value is -131cm and the most positive value is 120cm based on the Seasat/Dec 81 computation.

In order to obtain the geoid, our computed sea surface heights should be corrected by subtracting the sea surface topography defined by the spherical harmonic expansion given by Engelis in Appendix B. The predicted sea surface represents a mean surface defined by the Geos-3 and Seasat data. Certain short wavelength oceanographic features (such as cold rings) will be averaged out in the process. However, globally the long wave length signal will remain in the final estimate of the sea surface heights.

The gravity anomalies derived from the sea surface heights will be in error due to the fact that the heights were not corrected for sea surface topography. Since this error should be long wavelength one estimate of the anomaly error has been obtained from the spherical harmonic representation of sea surface topography. A contour map of the anomaly correction is shown in Figure B6 in the appendix. The maximum correction reaches -1.25 mgal with the rms value of about  $\pm 0.4$  mgal.

A series of tests were run separately to see the effect of sea surface topography on gravity anomaly predictions. These were done using our collocation procedures, as before, but now correcting the sea surface height for the sea surface topography. Predictions were made in three  $12^\circ \times 12^\circ$  areas where  $1/8^\circ \times 1/8^\circ$  grid predictions were made using uncorrected and corrected sea surface heights. The three areas were selected on the basis of the behavior of sea surface topography as seen in Figure B6. Area 1 (in the eastern South Pacific Ocean) was selected because of its fairly large gradient of SST. Area 2 (in the northwest Pacific Ocean) was selected because of the large magnitude (about 130 cm) of SST. Area 3 (in the North Atlantic Ocean) was selected because of the nominal magnitude (about 30 cm) of SST. The results of the comparisons of the two predicted anomaly sets in given in Table 11 for the 9216 points in each area.

Table 11  
Predicted Anomaly Difference<sup>+</sup> Due to Sea  
Surface Topography Effects  
(mgals)

Area	Geographic Limits	Ave Diff	RMS Diff	Std.	Max Diff
1	-48° $\phi$ -60° 240° $\lambda$ 252°	-1.8	$\pm 1.9$	$\pm 0.7$	-4.3
2	36° $\phi$ 48° 160° $\lambda$ 180°	2.1	$\pm 2.2$	$\pm 0.5$	3.7
3	24° $\phi$ 36° 303° $\lambda$ 315°	0.5	$\pm 0.6$	$\pm 0.4$	1.4

<sup>+</sup> Results from uncorrected sea surface heights minus results from corrected sea surface heights.

From Table 11 we see that the rms (root mean square) difference is on the order of  $\pm 2$  mgal which is much below the accuracy of the anomaly prediction. However the effect is systematic and can cause long wavelength error in the recovered anomalies. The average difference results given in Table 11 do not agree with the smaller values of the corrections implied by Figure B6 in the Appendix. The reason for the discrepancy is not clear. It is clear that the collocation solution can be very sensitive to sea surface topography estimates depending on the degree of the reference field. The higher degree the field, the better the fit to the observation. The resulting residuals will be small and may be primarily due to SST if not otherwise corrected.

Our computations will be for sea surface heights and gravity anomalies from uncorrected sea surface heights from altimetry. To obtain the geoid from our sea surface heights, we must apply sea surface topography corrections. There is no easy way to obtain corrected anomalies using our procedures. Acceptance of the predicted values relies on the  $\pm 2$  mgal error estimate obtained from the dual prediction tests.

#### Operational Data Selection and Production Runs

The testing of anomaly production procedures described earlier indicated that approximately 300 data points were sufficient for the prediction in a  $3^\circ \times 3^\circ$  area. We started our production procedures with this approach with the data being selected from our complete adjusted altimeter data tapes. There were 2,272,307 Seasat and 3,648,133 Geos-3 values on this tape. The data was first selected in the area of interest. This set was then reduced to approximately 300 data points through a selection of Geos-3/Seasat data in the same proportion that existed in the complete data set for the area. From this data we computed the mean residual of  $(N(\text{altimeter}) - N(180))$  and its standard deviation. We then deleted any point where the residual minus the mean exceeded 2.5 times the standard deviation. This process would delete a few bad points that still remained in the data set. Most of these points were from the Seasat data.

The results of the above process were not satisfactory because some track error that was still present in our data gave very clear signatures in the anomaly field with much less signature in the sea surface height maps. An example of this is seen in Figure 24. Systematic anomaly trends along the altimeter arc are clearly apparent. The track causing this error was identified. The predictions were then repeated and the revised values used in our final set.

This pattern structure occurred in a number of areas, but mainly in the Pacific Ocean. In order to reduce this problem a different data selection method was used. Specifically a "thinned" data set was created from the complete altimeter file. The basis of the thinned data base was the selection of one altimeter measurement in every  $10' \times 10'$  area in the oceans where the altimeter data was available. When there was more than one data point in the  $10' \times 10'$  area, the sea surface heights were meaned and the single point closest to the mean was selected for retention in the thinned data file. The retention was independent of the altimeter type (i.e. Seasat or Geos-3). The purpose of

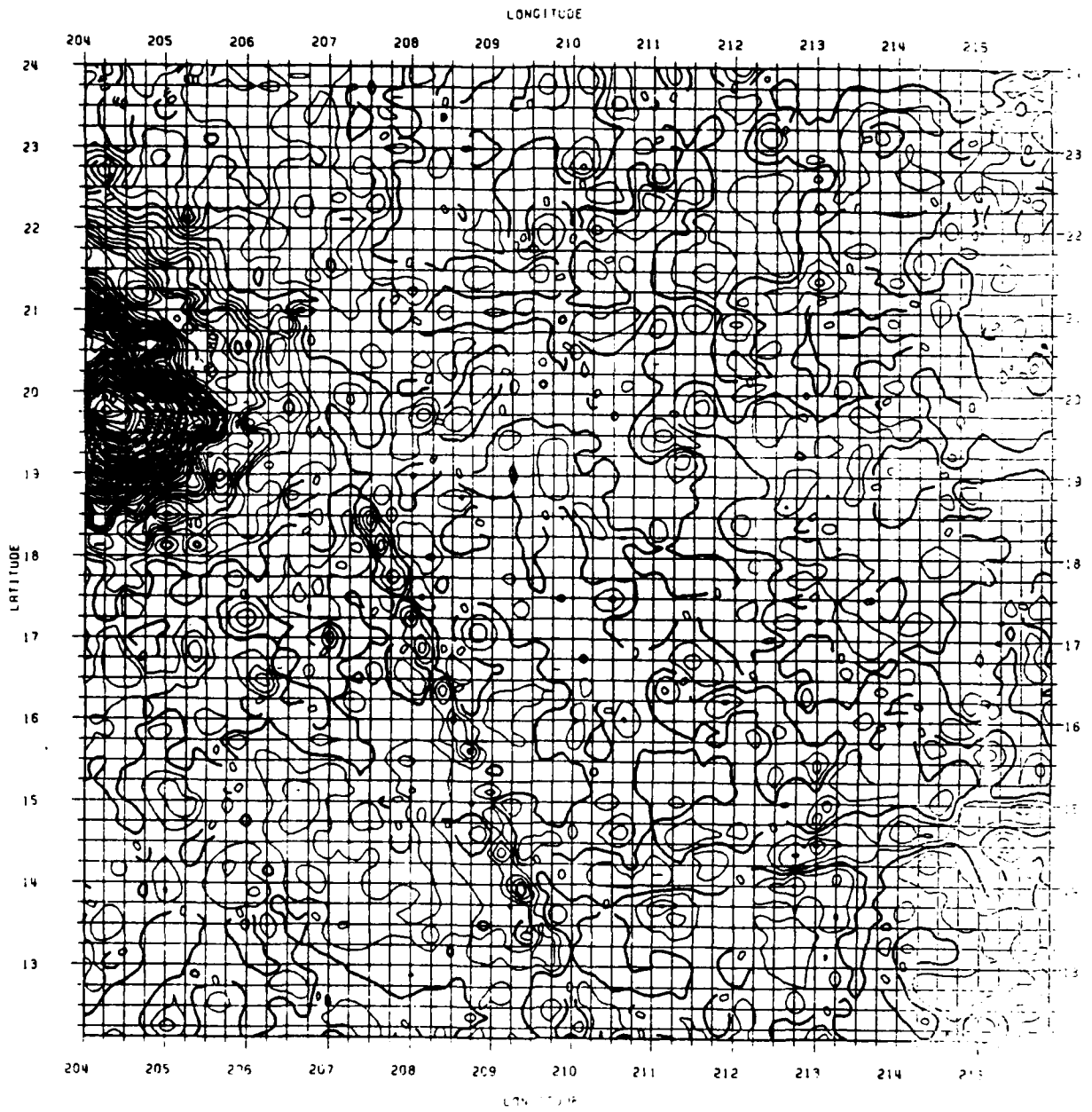


Figure 24  
Anomaly Contour Map Showing Structures Caused by Unremoved Track Error  
(Contour Interval is 10 mgal)

the thinning is to remove (as much as possible) data that would be associated in a sequential way, with a specific track.

Our final production predictions used the thinned data tape that contained 522,259 Seasat and 553,044 Geos-3 measurements. The maximum number of points available for the predictions in a 3°x3° block would be 576. Where the number exceeded 300, the actual points used were reduced to 300. The standard deviation check was then applied to the selected data with "bad" points being removed. Where the altimeter data was sparse the number of available points could be much less than 300. In no case were predictions made if there were fewer than 75 data points within the 3°x3° prediction block and its 0.5 borders.

The actual predictions were carried out in a systematic way. Generally a single run predicted the anomalies and sea surface heights in 16 3°x3° blocks. The execution time for a single run depends on the data available, but a typical time was 3.5 minutes on an Amdahl 470 V/8. Predictions near the coast lines required different size prediction blocks. In coastal areas predictions would also be made in land areas near the coast. Such values are not to be considered reliable. In those areas in which sufficient altimeter data was not available the anomaly and sea surface height were taken from the Dec 1981 potential coefficient set to degree 180.

At the completion of each run an anomaly and sea surface height contour map were automatically prepared. These maps were checked for track error signal and bad data point effects. The maps were also visually compared to the GEBCO bathymetric charts, and to anomaly maps available to us in the ocean regions. These comparisons were made to verify unusual features or to locate possible substantial errors in our predictions. In a number of cases we found signals in the predictions that were caused by track error or bad data points. Most of the errors were found from the examinations of the anomaly maps and not the sea surface height maps. This is because the effect of sea surface height errors is greatly magnified in going to the anomaly domain.

Our response to the obvious errors was the identification and removal of bad data arcs or data points with the prediction runs repeated. In some cases we repeated our computation with just "unthinned" Seasat data and Geos-3 data. This was done to check the reliability of the determination of an unusual feature. If the feature was implied by both data sets, it was considered verified. In some cases it was not possible to identify specific tracks for deletion. However, almost all remaining track error was in the Seasat data so that the predictions in some areas with clear track error was made only with Geos-3 data.

Some prediction problems were noticed in coastal areas and in areas below -60° to -65° in latitude. In such areas the sea surface height maps were not unreasonable but the anomaly values could change quite rapidly. The problem in the southern most latitudes was primarily related to the measurements on the ice by Seasat. Such values were clearly not edited out of our data set. We do not consider reliable any anomalies below ±-65°. In coastal regions the anomalies could be effected by the lack of data on the coast side of the prediction area. Predictions could be especially erratic in bays and narrow

waterways. We do not consider reliable any anomalies predicted within about 50 km of a coast.

Our last test for substantial track error was made by preparing color contour anomaly maps on a Tetronix 4115B terminal. It is much easier to identify track problems on a color display than thru examinations of contour maps. A few track errors still present were removed by the visual means. However, track error is still represented in our final data set. This error shows up as narrow structures in the anomaly map. These features are due to small (10 mgal) effects of unremoved track error. They are most clearly seen in the south Pacific where the anomaly field is quite mild and the track error effects stand out. An example of this is shown (unfortunately not in color) in Figure 25.

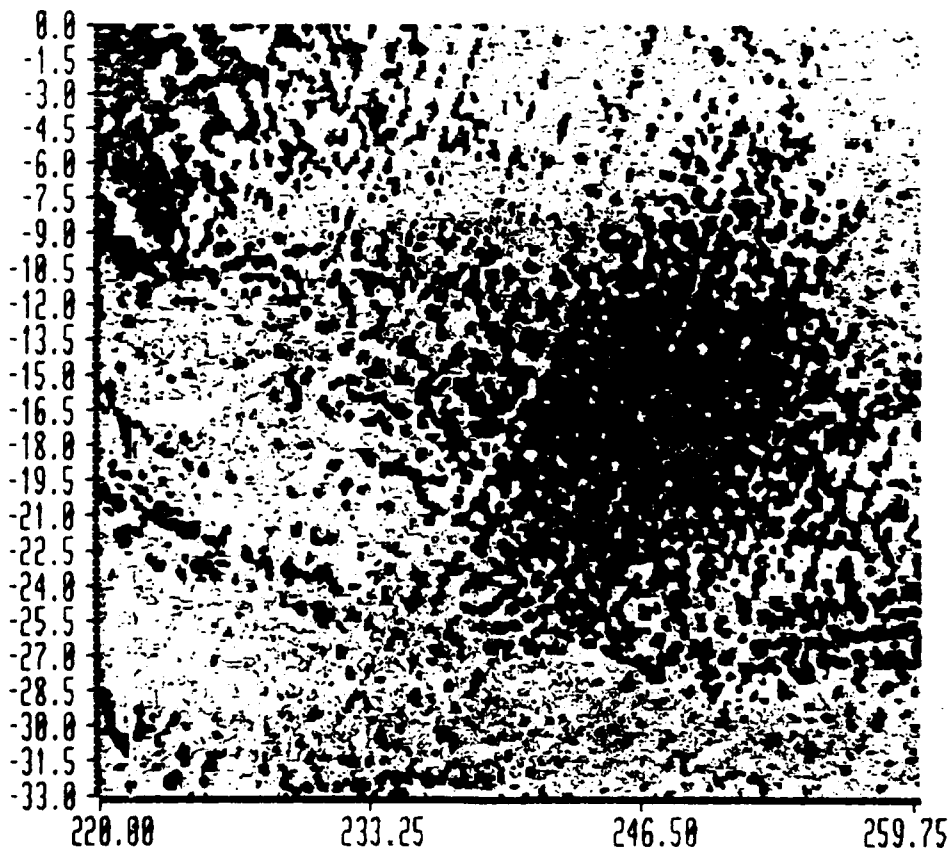


Figure 25  
Image of Gravity Anomalies Recovered in the South Pacific  
Showing Linear Features Caused by Residual Track Error  
Color Spacing Interval was 10 mgals

The track error remaining in the anomaly field can be filtered out in several different ways. One procedure tried with this data was to form a weighted average of points selected to be perpendicular to the direction of the satellite track. A five point average was tested by Engelis in the same area as Figure 25 with the results shown in Figure 26. Although much of the apparent track error is removed some remains. However, it is also clear that high frequency information is very lost. Although we could have created a point data set that had the track error removed by smoothing we chose not to because of the possible loss of high frequency data. Additional study needs to be carried out to develop procedures to filter out features of a linear type that are specifically in the direction of the altimeter ground track. A procedure that was applied to terrestrial data by Forton (1984) may also be applicable to this problem.

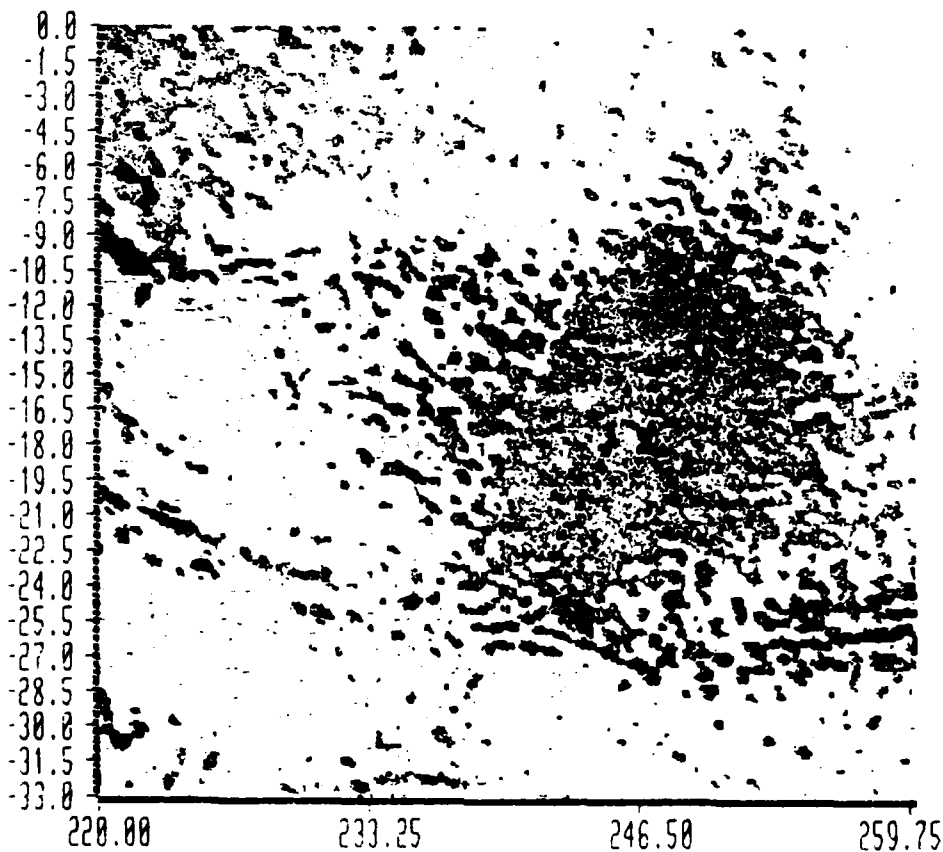


Figure 26  
Image of Gravity Anomalies with Smoothing  
To Reduce Features Caused by Track Error

### The Standard Deviations of the Predicted Quantities

As discussed in an earlier section, we did not compute specific accuracy estimates for each predicted point. Instead a uniform standard deviation was assigned using a covariance scaling technique. However, this value does not take into account the distribution of the altimeter data used in the prediction. To consider this we used an empirical technique that was based on the number (N) of altimeter measurements in the 0°.5x0°.5 block in which the point fell. Specifically we used:

$$SD(\text{New}) = SD(\text{Old}) \sqrt{\frac{5}{N}} \quad (21)$$

If N were zero, the factor multiplying SD(old) was set to be 2.5. The location of the 0°.5x0°.5 blocks in which there is no data is shown in Figure 27. If no predictions were made in a 3°x3° region because of too few points the anomalies and geoid undulations from the Dec 81 180 potential field were used. In this case the assigned standard deviations of 99.0 mgals were used, primarily to identify the values as being from a spherical harmonic field. In two regions close to land areas the anomalies were very erratic and unrealistic. The anomalies in these areas had their standard deviations set to 100.0 mgals. The two regions were 60°E ♦ E 54°, 8°E λ E 12°, and 66°E ♦ E 57°, 291°E λ E 297°.

The location of 0°.5x0°.5 blocks where at least one point value has a standard deviation greater than 30 mgals is shown in Figure 28. Many of the areas represent land areas in which the predictions were automatically done.

### Statistical Analysis of the Point Predictions

The total number of predicted anomalies and sea surface heights was 2,399,833. However 223,065 of these values had standard deviations greater than 30 mgals which would indicate unreliable estimates. (Most of these values were on land as seen from Figure 28). We therefore computed statistics only for those values where the standard deviation was E 30 mgals. In this case the mean value(uncorrected for the effect of the atmosphere) was -0.77 mgals; the root mean square value was E 28.6 mgals; the maximum value was 396 mgals and the minimum value was -360 mgals. The frequency distribution of these anomalies is shown in Table 12.

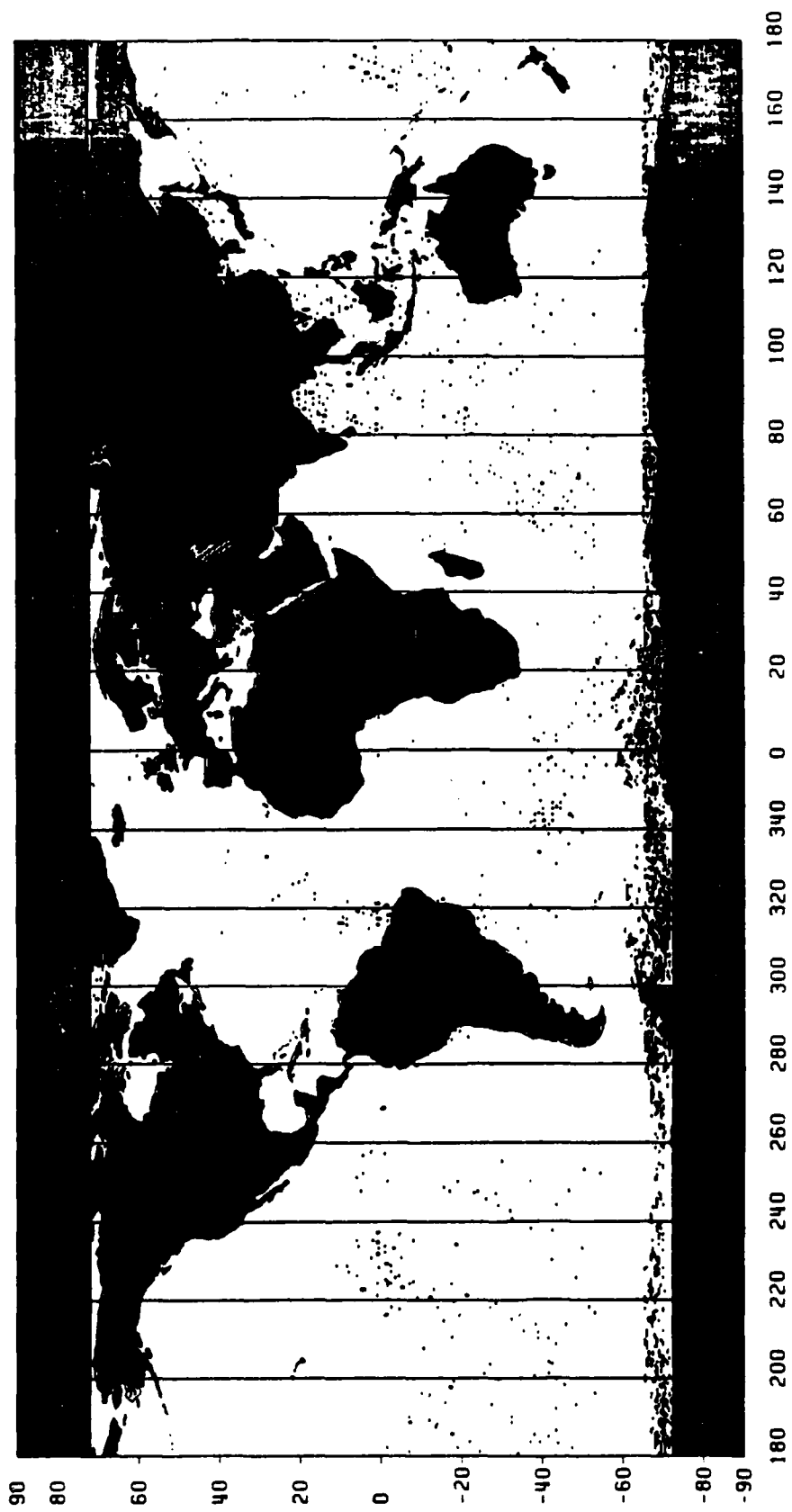
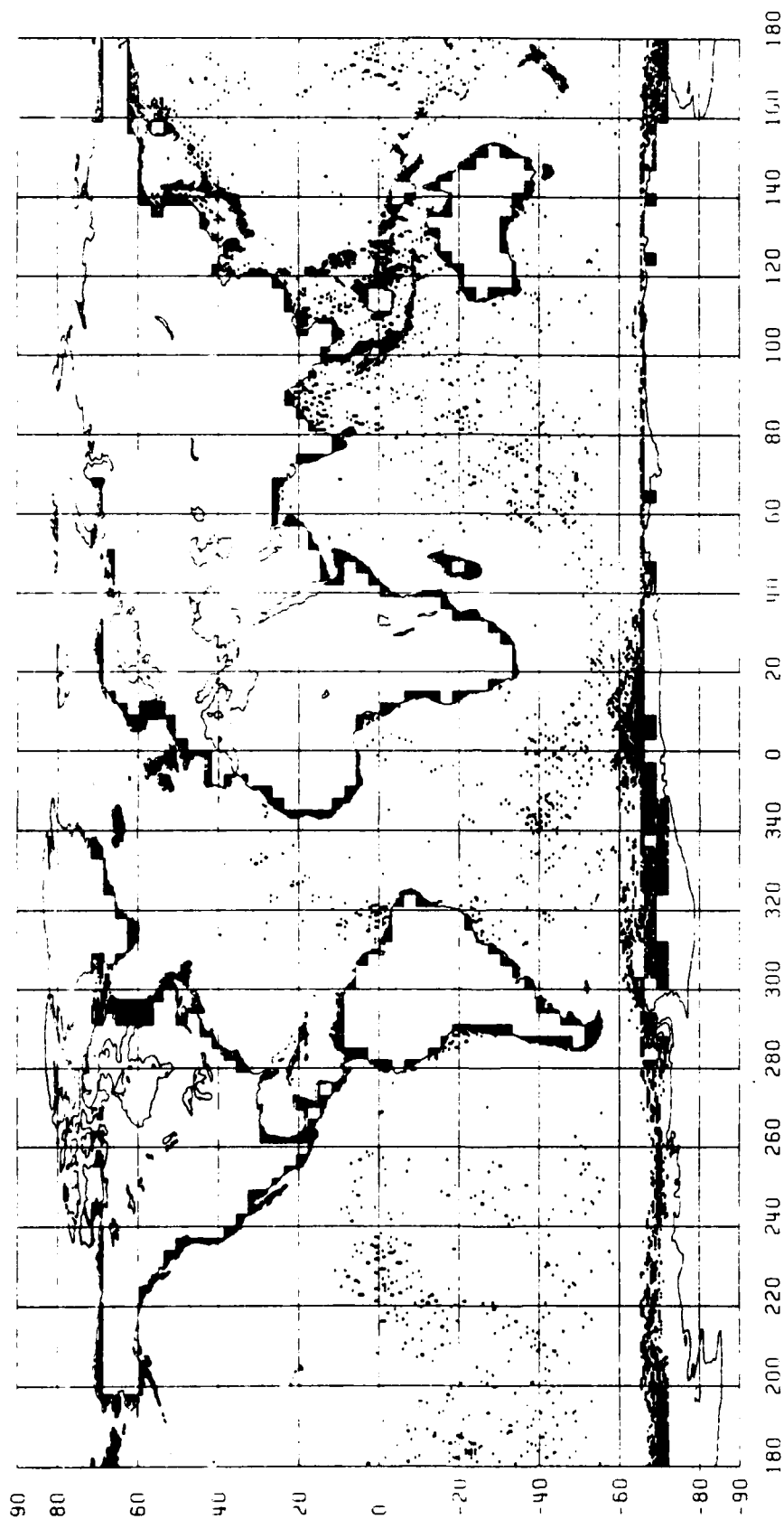


Figure 27  
Location of 0.5x0.5 Blocks in Which No Other Data Exists





**Figure 28**  
**Location of 0.5x0.5 Blocks Where One or More Point Anomaly Values Have Standard Deviations Greater Than 30 mgals**

Table 12  
 Frequency Distribution of Predicted Gravity Anomalies

Range (mgal)	Number
-400 to -350	5
-350 to -300	93
-300 to -250	421
-250 to -200	1493
-200 to -150	4044
-150 to -100	8676
-100 to -50	54603
-50 to 0	1074079
0 to 50	962535
50 to 100	60100
100 to 150	8156
150 to 200	2069
200 to 250	408
250 to 300	61
300 to 350	17
350 to 400	8

The mean value of the predicted standard deviation was  $\pm 12.2$  mgals; the root mean square standard deviation was  $\pm 12.7$  mgals; the minimum value was  $\pm 10$  mgals. The maximum standard deviation of the original data set was 99 mgals.

The location of the  $0.5 \times 0.5$  blocks in which anomalies exceeded 100mgals in absolute value (and standard deviations were less than 30 mgals) are shown in Figure 29. Clearly these values generally follow well known trench structures in the oceans. A number of these values occur below  $-60^\circ$  latitude. Such values are primarily due to altimeter measurements on ice. We were unable to completely edit altimeter measurements that were contaminated by ice effects. The sea surface heights in such areas did not show clear problems, but the anomalies computed from such data were quite erratic. Generally we should view carefully, any anomalies below  $-60^\circ$  latitude, and completely discard any anomaly values below  $-65^\circ$  latitude.

The maximum anomaly that was predicated (i.e. 396 mgals) occurred at  $\phi=19^\circ.5$ ,  $\lambda=204^\circ.5$  which is just at the eastern edge of Hawaii. Another group of large anomalies (374 mgals) occurred in the western Pacific over the Ogasawara Ridge,  $\phi=28^\circ.00$ ,  $\lambda=142^\circ.00$ . The Ridge is located just to the west of the Izu Trench. Over the trench the anomalies are very negative. For example, at  $\phi=28^\circ.00$ ,  $\lambda=143^\circ.375$ , the anomaly is -141 mgals. This yields an average horizontal gradient of 3.8 mgals/km.

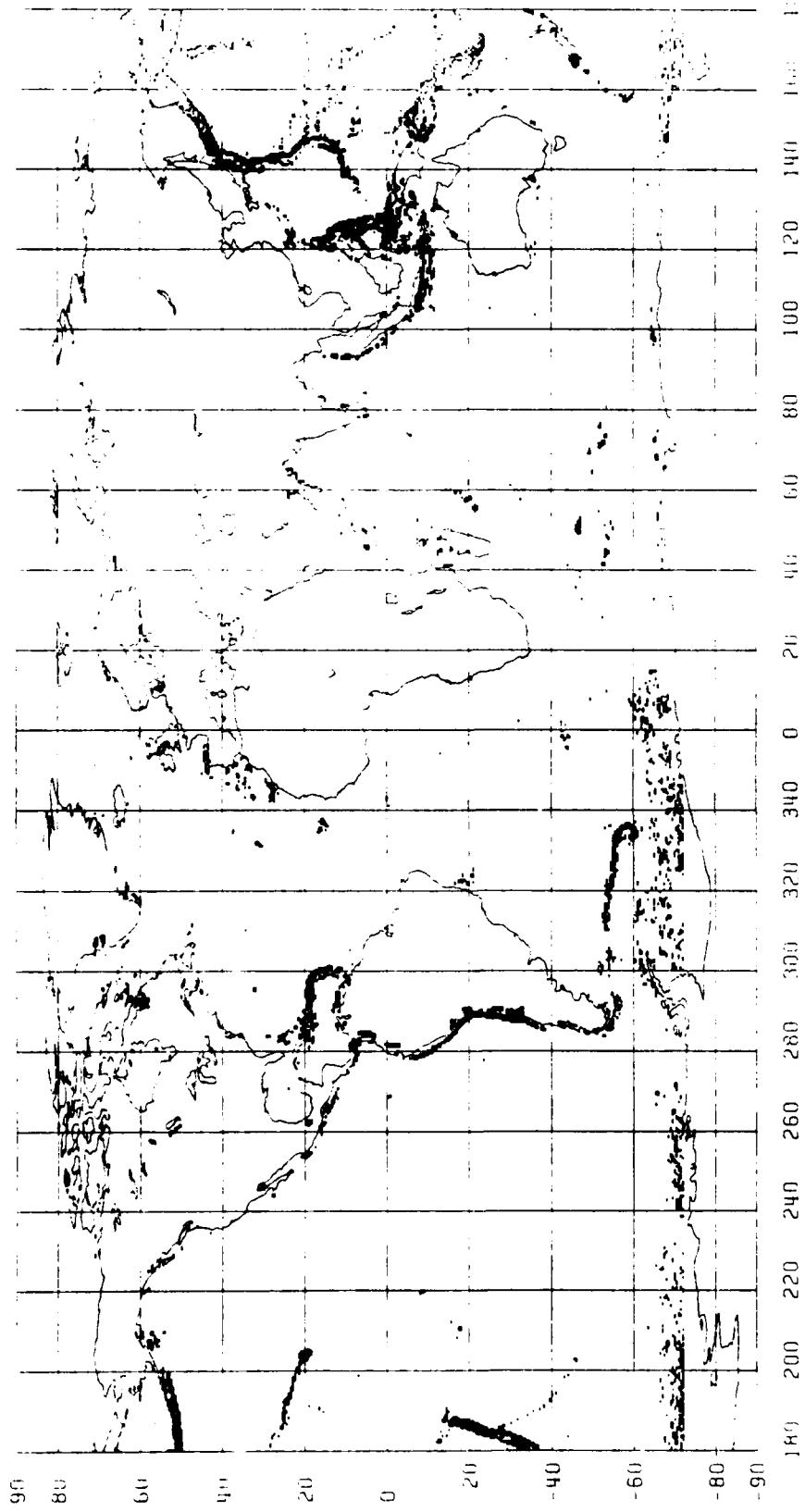


**Figure 29**  
**Location of 0:5x0:5 Blocks in Which a Point Anomaly Exceeded 100 mgals in Absolute Value**

The most negative anomaly (-361 mgals) in the eighth degree data occurs at  $\phi=19^{\circ}.5$ ,  $\lambda=293^{\circ}.50$  over the Puerto Rican Trench. Considering the positive anomalies 100 km to the north, the horizontal anomaly gradient in this case is approximately 3.6 mgals/km.

For the points in which the anomaly standard deviation was  $\pm 30$  mgals the mean sea surface height was 1.69 m; the root mean square value was  $\pm 31.1$  m. The maximum sea surface height was 83.8 m while the minimum was -107.1 m. The mean standard deviation was 0.13 m. The mean value of 1.69 m implies that the mean geoid undulation in the ocean areas must be on the order of -1.65 m since the mean sea surface topography i.e. ( $\zeta-N$ ) was shown earlier (see Figure 23) to be approximately 4 cm.

### Selected Anomaly and Sea Surface Height Maps

The predicted anomalies and sea surface heights provide a uniform data set for almost all ocean areas. The anomalies have a predicted accuracy on the order of  $\pm 13$  mgals. The accuracy deteriorates near coastal regions and in the south polar regions. In most other areas the data provides a large amount of detailed gravity field data. To demonstrate this, we selected a number of areas in which to make contour maps from the 0.125 data.

Figure 30 shows a perspective view of the relative sea surface in the area of the Magellan Seamounts near the Bonin and Mariana Trenches. The value shown is the predicted sea surface height minus the undulation implied by the GEM9 potential coefficients to degree 20. The removal of the most systematic part of the sea surface clearly reveals the signatures of the sea mounts and trenches in this area. Figure 31 shows the gravity anomalies in the same area. The gravity anomalies shown in Figure 31 range from -256 mgals to 185 mgals. The most positive anomaly occurs at  $\phi=15^{\circ}.5$ ,  $\lambda=155^{\circ}.2$  which is at the center of a large seamount in the East Mariana Basin. It is also clear that the anomaly gradients can be quite large reaching 80 mgals in 13 km.

A second area that is of interest is near the Aleutian Trench. The sea surface heights, in perspective view are shown in Figure 32. This view clearly shows the trench, Bowers Ridge and Basin, the Shirshov Ridge and the start of the Emperor Seamount chain. The corresponding gravity anomaly map is shown in Figure 33.

Another area showing large anomaly variations is the area of the Sula Islands in the Molocca Sea. The anomalies are shown in Figure 34. The predicted anomalies range from -256 mgals to 229 mgals in a distance of approximately 170 km or an anomaly gradient of 2.8 mgal/km. These large variations may be compared to similar large changes on the terrestrial map by Watts and Bodine (1978).

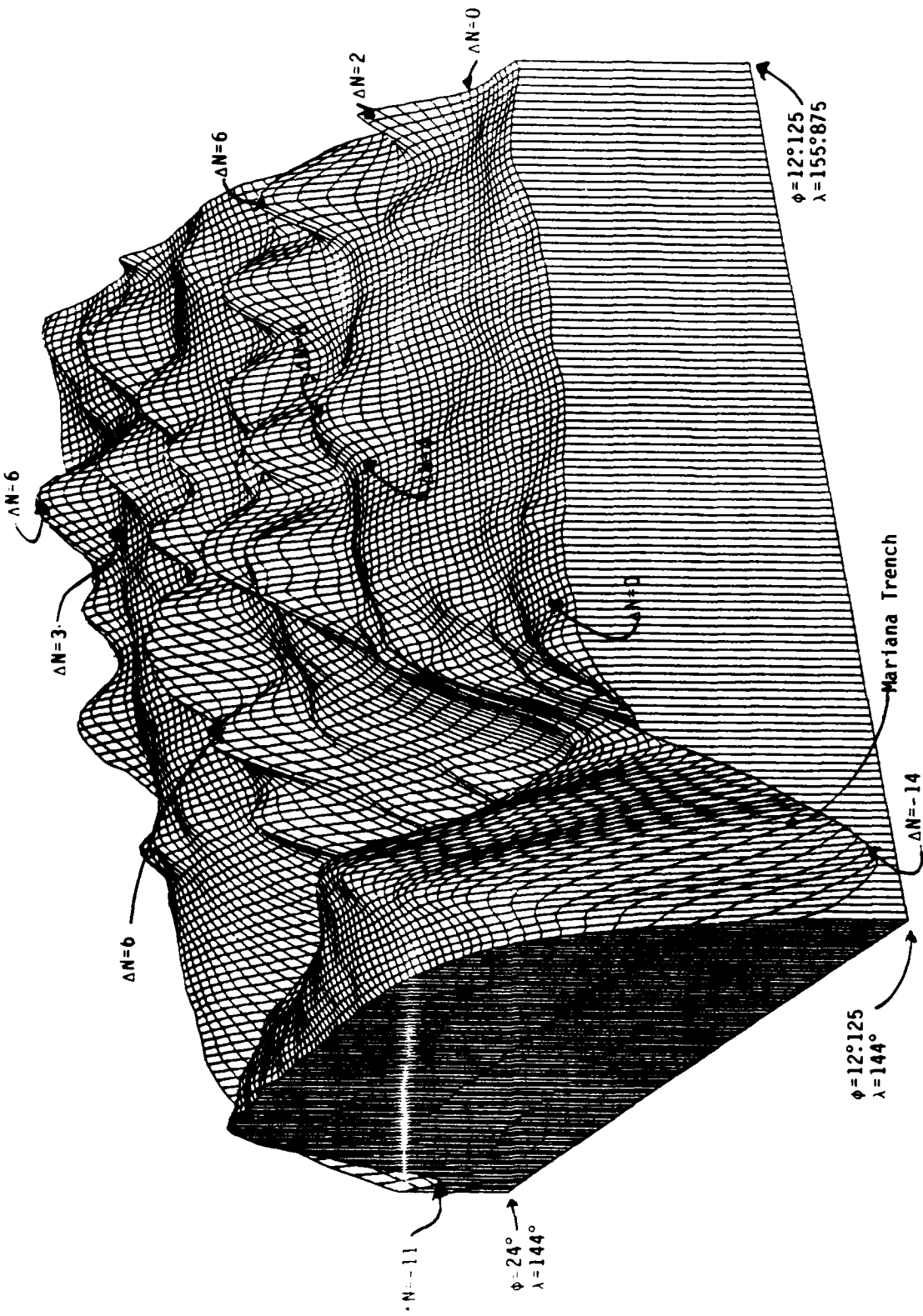


Figure 30  
 Sea Surface Heights From GEOS-3 and Seasat Altimeter Data Minus GEM9 Undulations in the Area of the Magellan Sea Mounts (units are meters)

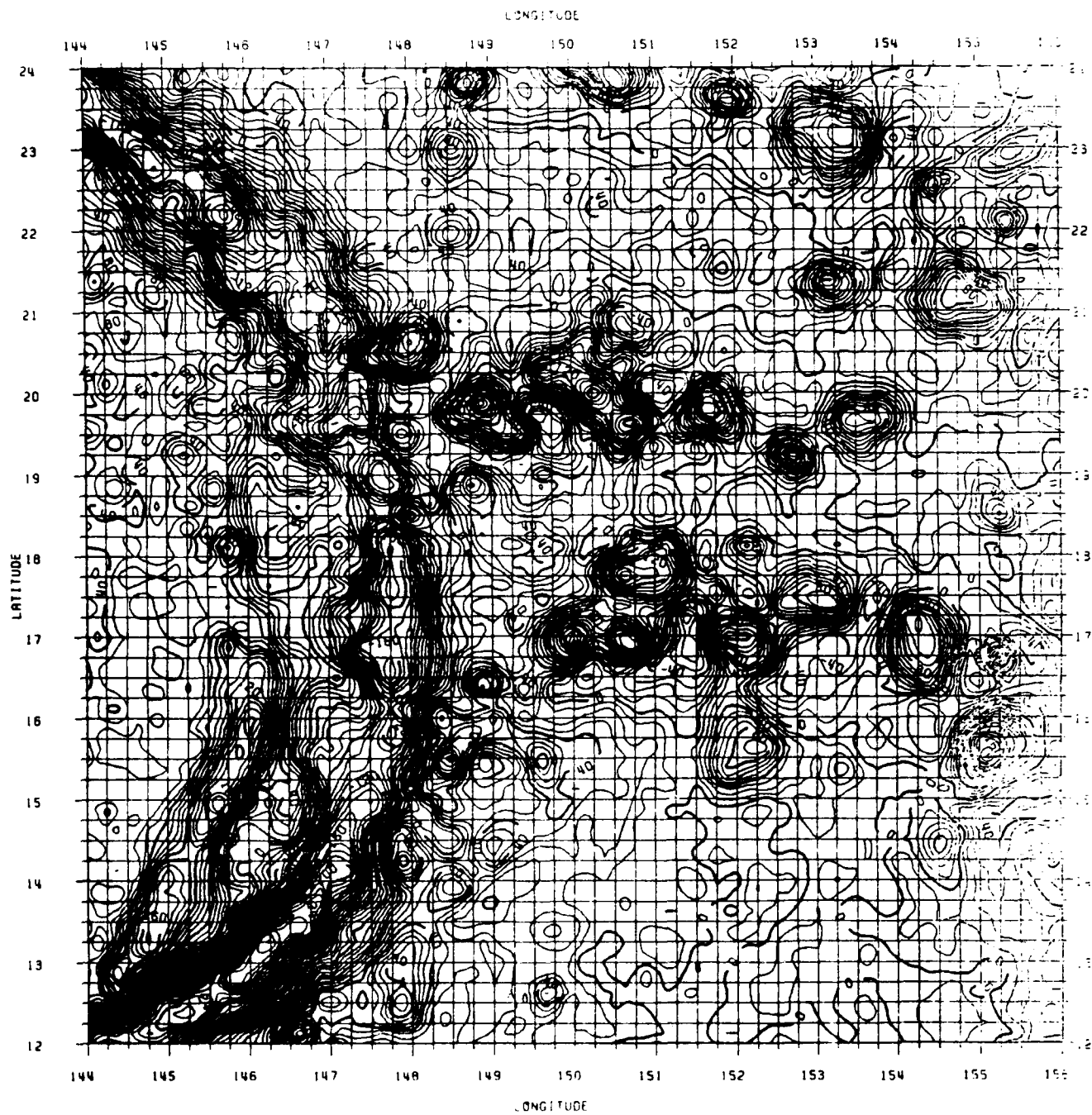


Figure 31  
Gravity Anomalies in the Area of the Mariana Trench and Magellan Seamounts  
(Contour Interval is 10 mgals)

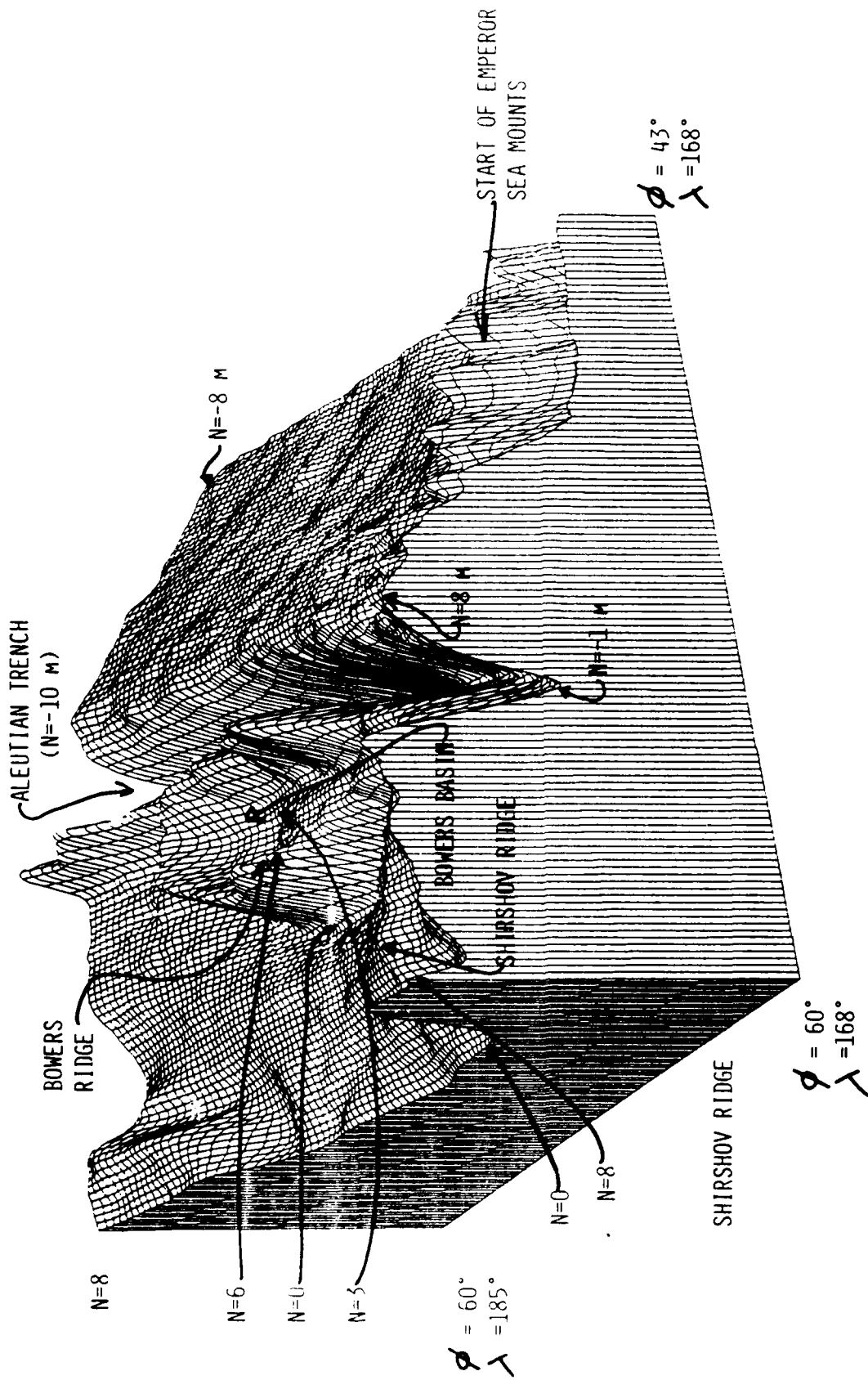
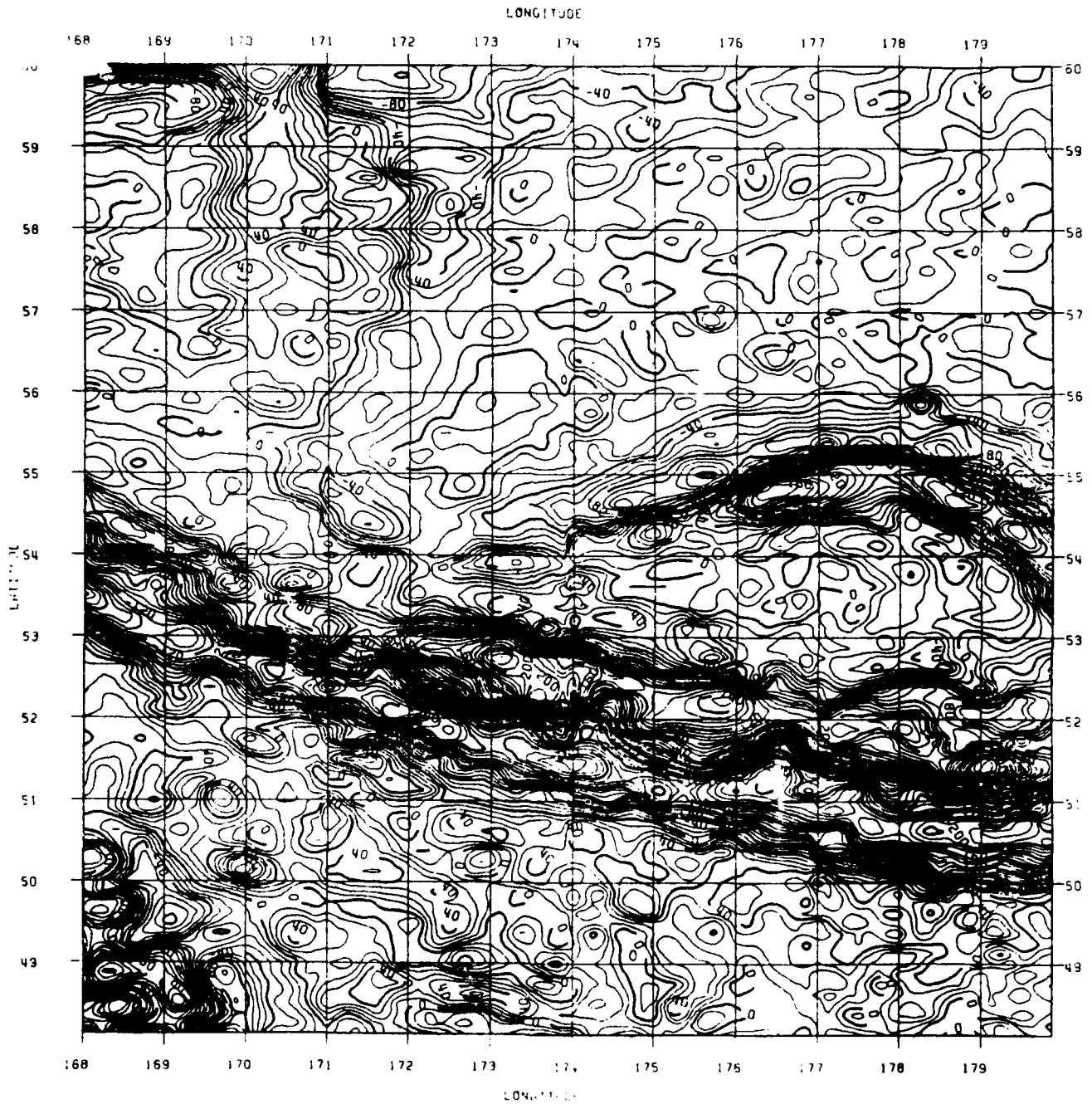


Figure 32  
 Perspective View of the Sea Surface Heights Across a Portion of the Aleutian Trench



**Figure 33**  
**Gravity Anomaly Map Over a Portion of the Aleutian Trench**  
 (Contour Interval is 10 mgals)



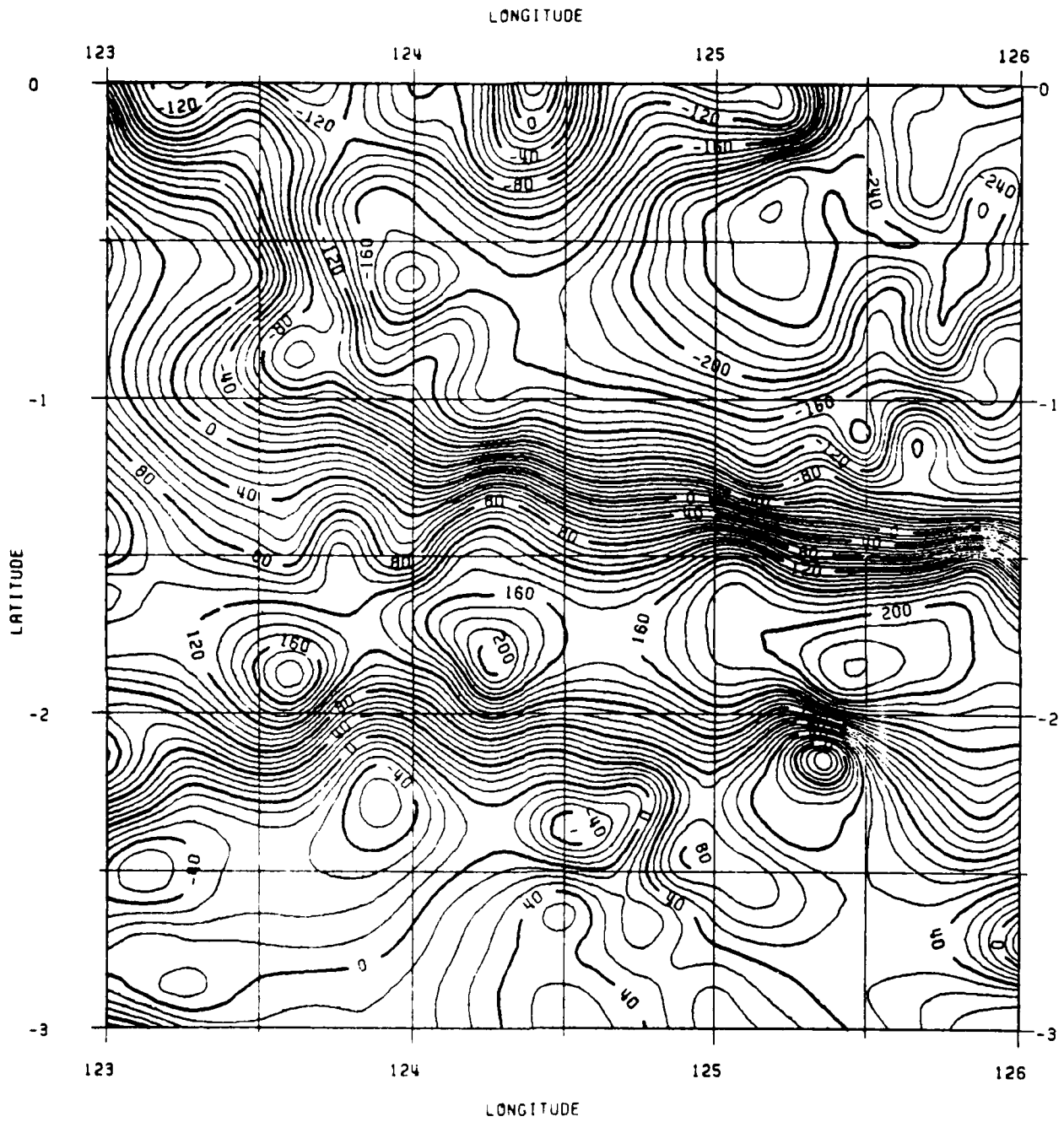


Figure 34  
 Predicted Gravity Anomalies in the Area of the Sula Islands in the Malacca Sea  
 (Contour Interval = 20 mgals)

Another area showing significant seamount signature is in the south west Indian Ocean. A perspective map showing several sea mounts including the Lena and Ob seamount is shown in Figure 35 where the sea surface height minus the geoid undulation from the GEM9 potential coefficients is displayed. The view looks in a south east direction.

Another area that shows the detail in the predicted data is that related to the Mendocino Fracture Zone in the north east Pacific Ocean. The signature of this structure is clear in Figure 36 which is a perspective view of the sea surface heights minus the undulations computed from the GEM9 potential coefficients. The step structure across the Mendocino Fracture Zone is clear as well as a smaller step across the Murray Fracture Zone.

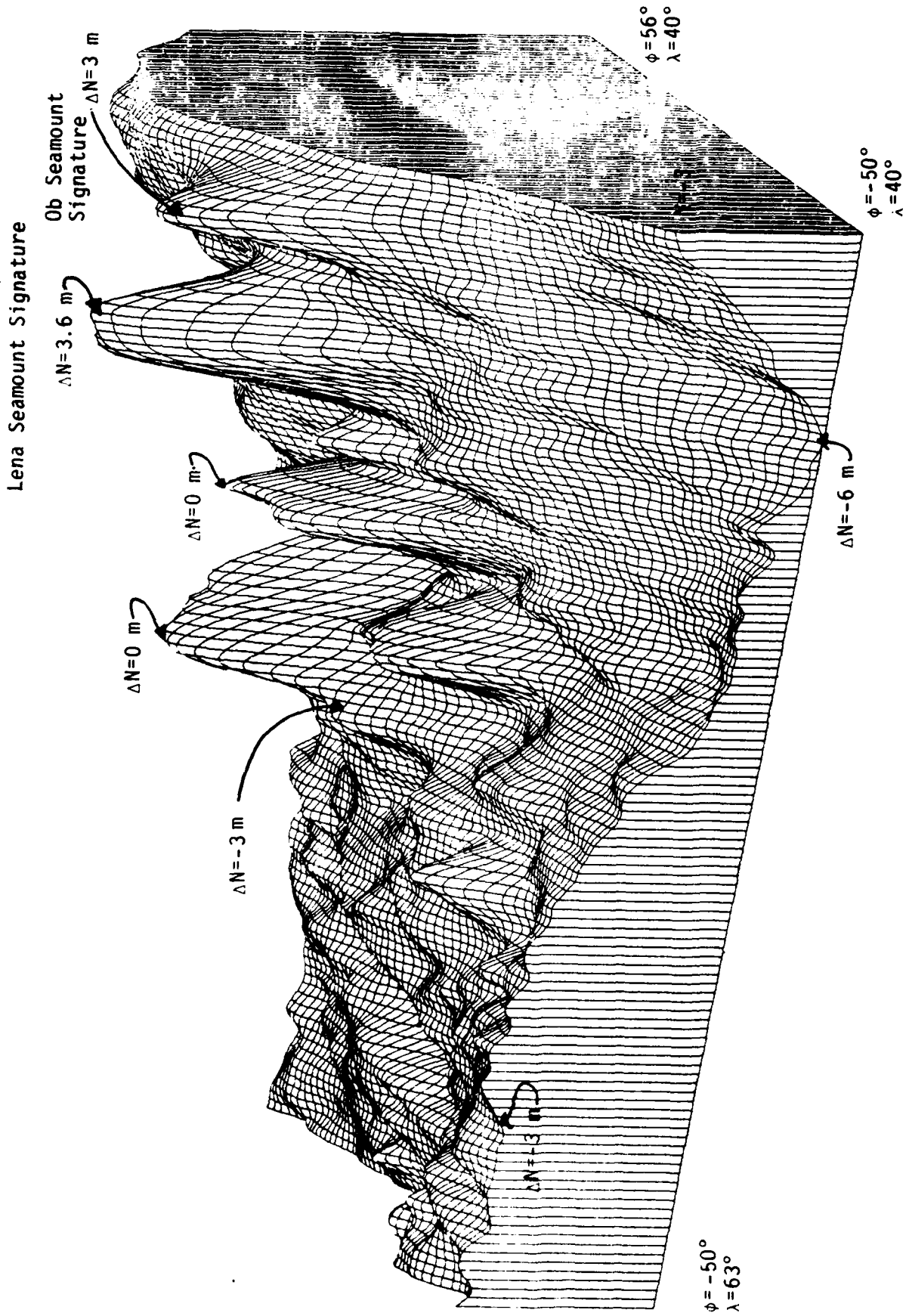


Figure 35  
 Perspective View of N-N(GEM9) in the Area of the Lena and Ob Seamounts  
 (Units are meters)

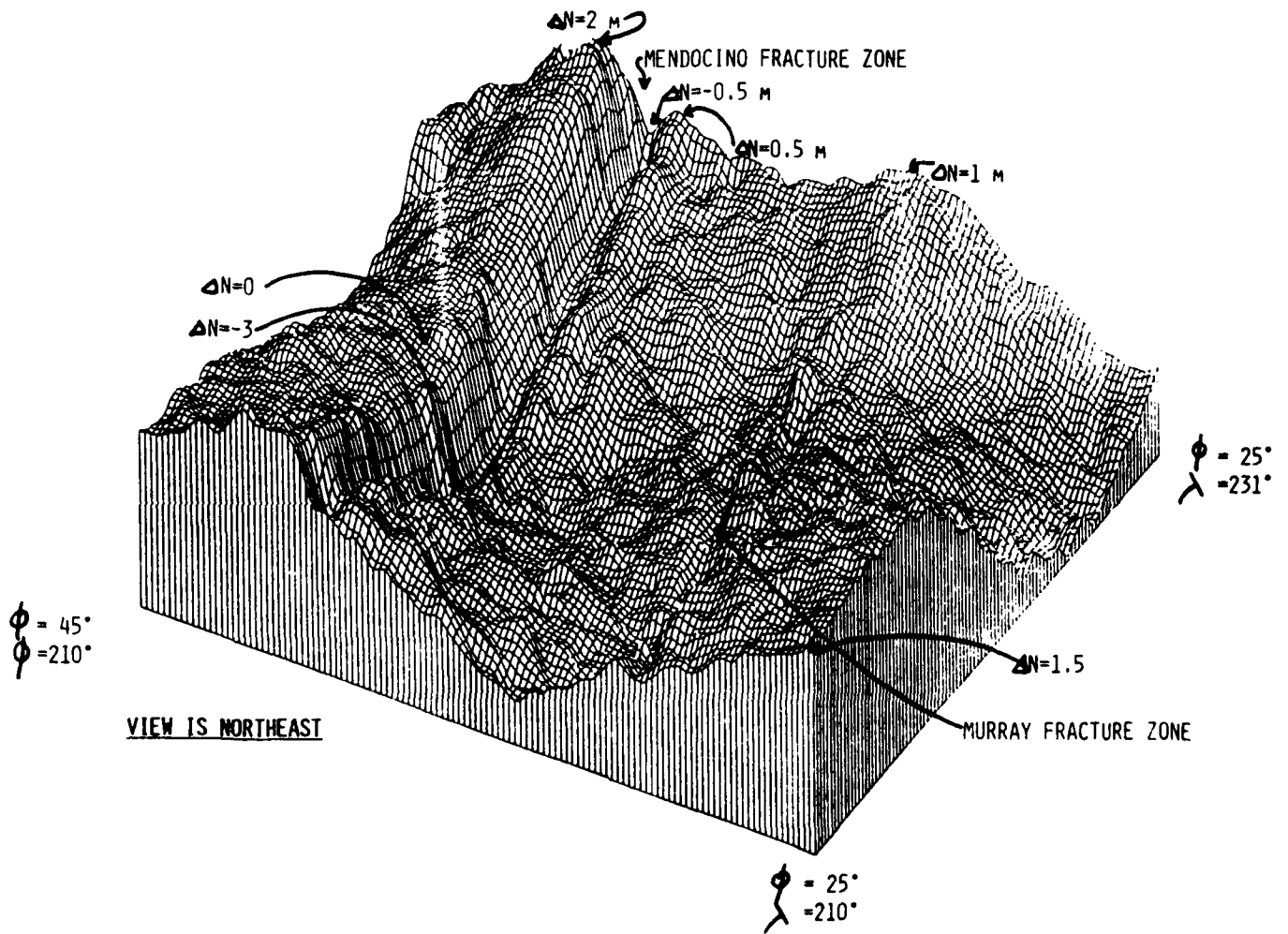


Figure 36  
 Perspective View of N-N(GEM9) in the Area of the Mendocino Fracture Zone

For our last group of graphical displays of the 0:125 data set we look at anomaly signatures in three relatively small areas. The first area is in the north Pacific in the area of Johnston Island which is located at  $\phi=16^{\circ}6'$ ,  $\lambda=190^{\circ}4'$ . The gravity anomalies and sea surface heights in the vicinity of this island are shown in Figure 37.

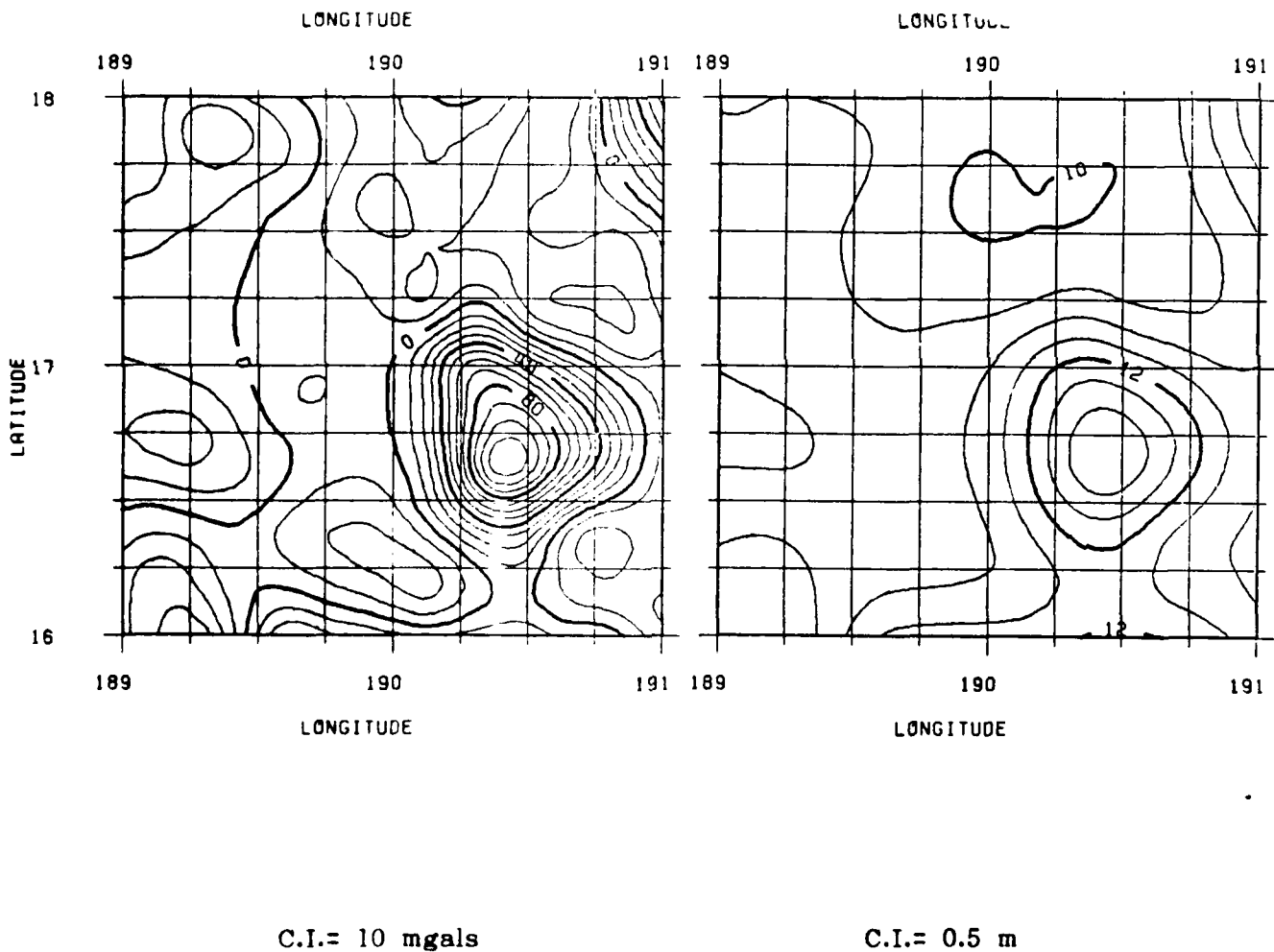


Figure 37  
Gravity Anomalies and Sea Surface Heights  
In the Vicinity of Johnston Island

The anomalies in the area of the island are quite positive being inconsistent with some 1°x1° mean anomaly estimates for the block containing the island. However the altimeter result is believed to be the more reliable value based on independent estimates.

The next area of interest is the Discovery Seamounts located in the South Atlantic Ocean. As judged by the map of Kogan and Watts (1983) terrestrial gravity measurements are available over the seamount only which is located at  $\phi=42^{\circ}.0$ ,  $\lambda=0^{\circ}$ . Figure 38 clearly shows the seamount where the anomaly maximum is 145 mgals. A number of other sea mounts are also present with the largest anomaly reaching 160 mgals at  $\phi=-43^{\circ}.7$ ,  $\lambda=358^{\circ}.6$ .

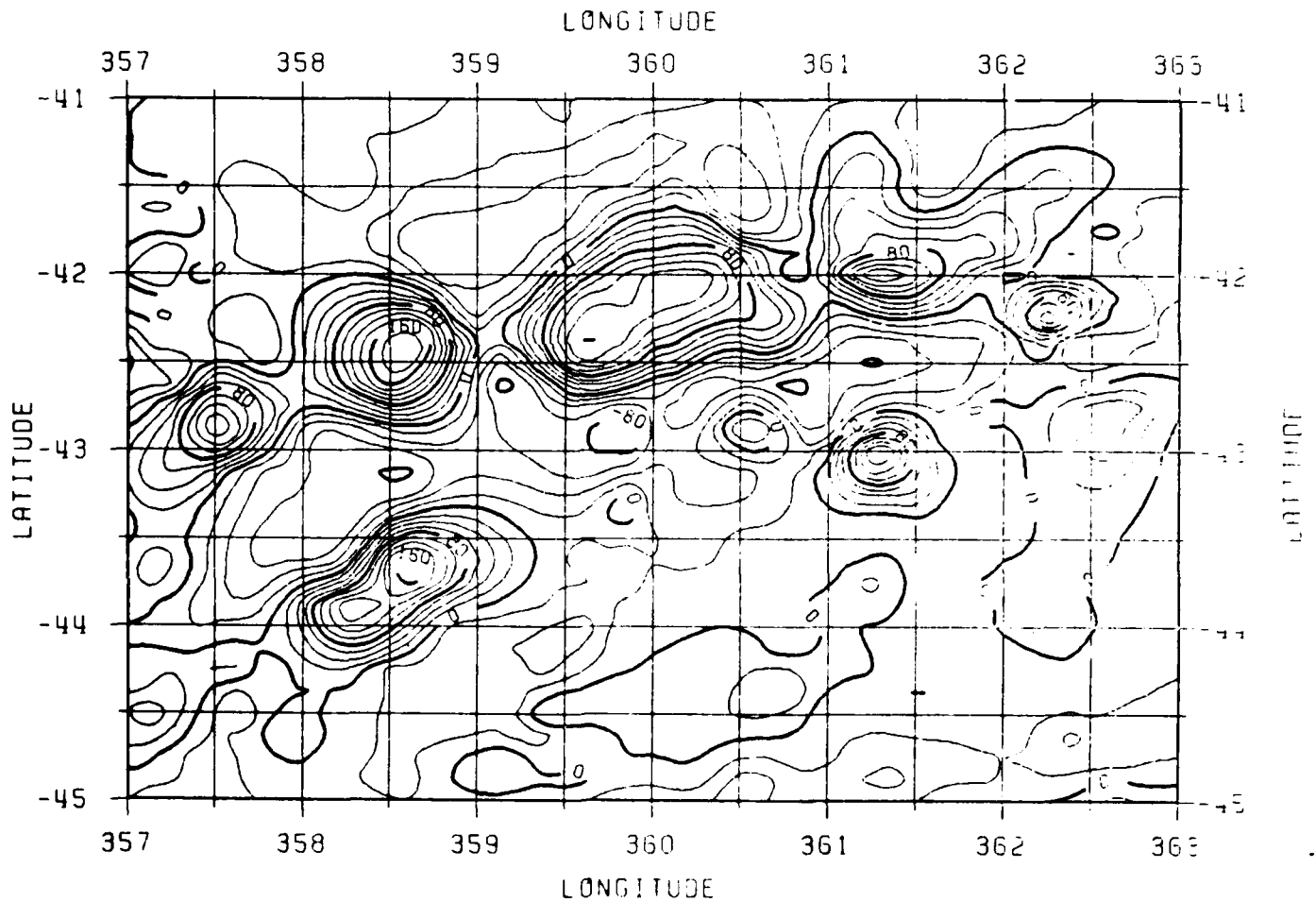


Figure 38  
Gravity Anomalies in the Discovery Seamount Area  
(Contour Interval is 20 mgals)

The last area to be considered is in the North Atlantic over a part of the New England Seamounts. With our original predictions the gravity anomalies over a portion of the sea mounts are shown in Figure 39.

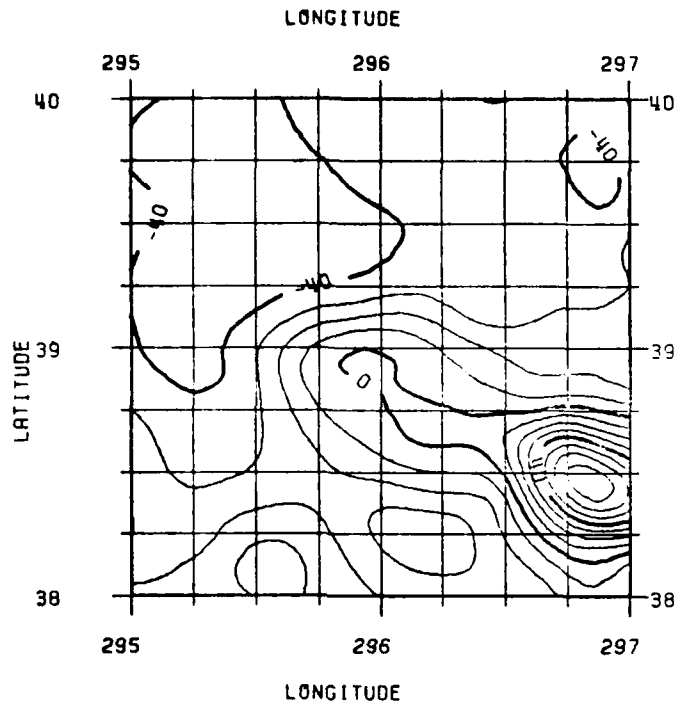
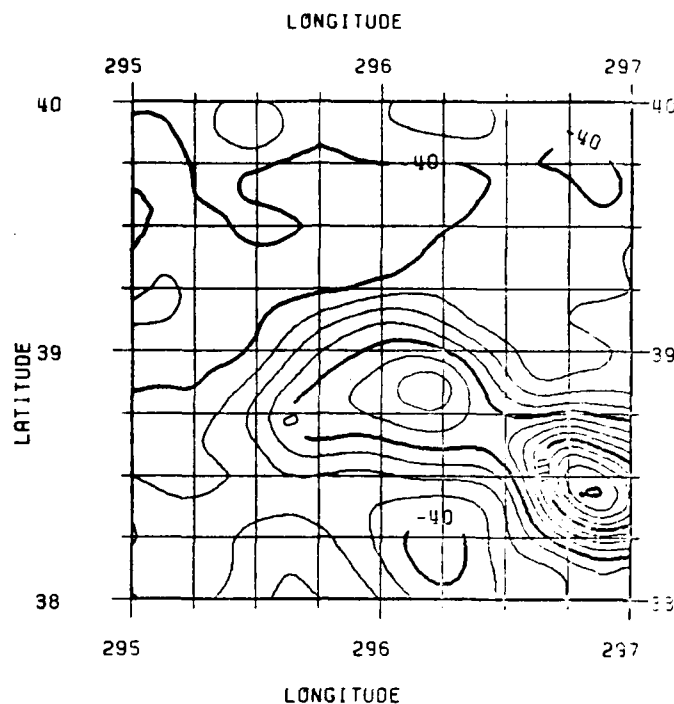


Figure 39  
Gravity Anomalies in New England Seamount Area  
Based on Production Data Selection Method

From bathymetry and previous studies (Rapp, 1984) we know that there is a seamount at  $\phi=38^{\circ}.8$  and  $\lambda=296^{\circ}.2$ . It is clear from Figure 38 that no significant seamount signature is seen. Examinations of the altimeter data used in the prediction run showed no points selected in the immediate vicinity of the known seamount. A second prediction run was made using 500 data points in a  $2^{\circ} \times 2^{\circ}$  area surrounding the seamount. The anomaly map is shown in Figure 40.



**Figure 40**  
**Gravity Anomalies in the New England Seamount Area**  
**Using 500 Altimeter Points in a 2°x2° Area Plus Border**

We now start to see the seamount signature in the expected location with a maximum gravity anomaly of about 23 mgals. This magnitude was less than expected so that a third prediction was made using 300 data points in and around the 1°x1° centered about the seamount. The results of this prediction are shown in Figure 41. Now a very strong signature is seen that reaches 62 mgals. In fact the 180 reference field is negative (about -20 mgals) in the area so that the correction to the reference field reaches 85 mgals.

The point of the above discussion is to show how we can miss the signal association with a high frequency phenomenon using the data selection and prediction procedures that we have used. Based on a general analysis we feel that much detail has been detected. However based on this example we know some could have been missed. The data stored in our final data tape was that associated with Figure 39. This was done for consistency of the predictions with the surrounding regions.

The primary intent of this graphical presentation of the results has been to indicate the detail that is present in the 0.125 data set. This detail is seen more readily in the gravity anomaly field than in the sea surface height field. However, at this point we have no quantitative statement of the information content or spectral limit of the data. We turn to this in the next section.



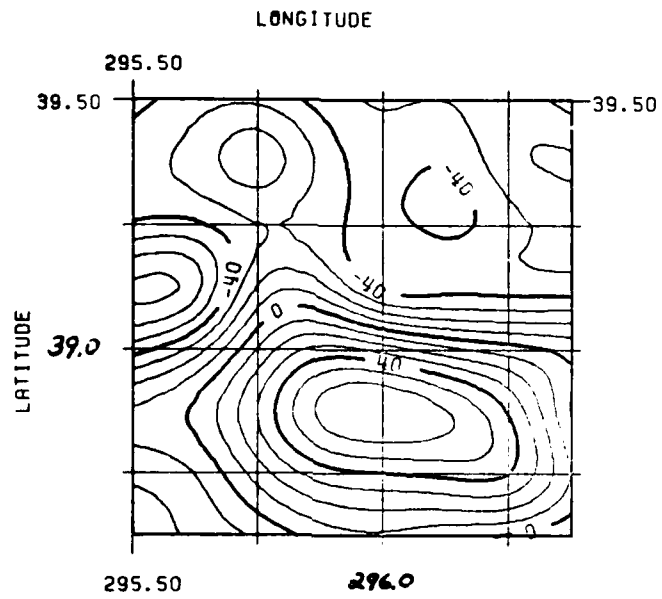


Figure 41  
Gravity Anomalies in the New England Seamount Area  
Using 300 Altimeter Points in a 1°x1° Area Plus Border

### Spectral Content of the $0^{\circ}.125 \times 0^{\circ}.125$ Predicted Values

The  $0^{\circ}.125$  grid interval was originally chosen so that no information would be lost in the prediction/gridding process. In principle we wanted to retain as much high frequency information in our final data set that is consistent with the original data and our computational resources. We now must see if our gridding is in fact a reasonable one, or should we have chosen a larger interval such as  $0^{\circ}.25$ .

The original data was given at one second intervals implying along track spacing of 7 km. Brammer and Sailor (1980) estimated the resolution limit of the SEASAT data to be on the order of 25 to 40 km. A lower resolution could be expected from the GEOS-3 data because of the poor noise quality. In addition we must be aware of the variable track spacing of the altimeter data which can vary from 10 km to 100 km depending on geographic area.

In addition our predicted quantities have a frequency cut off implied by the data selection process. For most of our predictions we selected 300 data points in a  $4^{\circ} \times 4^{\circ}$  block. This implies one data point per  $26 \times 26$  km block which could form a resolution limit of our data which would be on the order of  $0^{\circ}.23$  which would correspond to a spherical harmonic expansion to about degree 780.

A second approach to this problem is to carry out a power spectrum analysis of the data using Fast Fourier Transform technique. For our test eight profiles whose length is  $60^{\circ}$  (i.e. 481 points) were chosen in different parts of the oceans. An FFT analysis was performed by T. Engelis. Adopting a somewhat arbitrary criterion that 99.7% of the power in the spectrum defines the maximum wave number ( $m$ ) present in the profile, the value of  $m$  varied from 134 to 202 with an average value of 155 where the fundamental frequency is 1 cycle/60 degrees. Using equation c11 (in Appendix C) these wave numbers correspond to spherical harmonic degrees of 802, 1204, and 928 respectively. In terms of resolution this corresponds to 24.9 km to 16.5 km, or an average 21.5 km which corresponds to  $0^{\circ}.19$ . (This resolution is somewhat smaller than the 17 km resolutions from Seasat data estimated by Brammer and Sailor (1980)). On the basis of this analysis the approximate prediction interval would have been  $0^{\circ}.19$  so that using  $0^{\circ}.125$  can not be completely justified. However, it is clear information is lost if a  $0^{\circ}.25$  grid is used. In addition the computation of the values on the  $0^{\circ}.125$  grid has been done in a consistent manner considering a collocation estimation and such values can be helpful in areas where the gravity field is changing rapidly.

### $1^{\circ} \times 1^{\circ}$ Mean Anomaly Determinations and Comparisons with Terrestrial Data

Our past work with anomaly recovery from altimeter data has primarily been for  $1^{\circ} \times 1^{\circ}$  anomalies (Rapp 1979). Many of the computed values can be compared to terrestrial estimates for accuracy checks or for the identification of significant errors in one set of (primarily terrestrial) anomalies.

Using the  $0^{\circ}.125$  gridded data a set of  $1^{\circ} \times 1^{\circ}$  anomalies was computed. The computations involved the straight mean of all available points (usually 81) that

fell in and on the borders of the block. The disadvantage of this procedure is that it causes a small error correlation between adjacent blocks due to using some of the same data points in the mean anomaly estimations. Between latitude limits  $\pm 72^\circ$ , 37419  $1^\circ \times 1^\circ$  values were computed. Of these, 2364 were on land and are considered unreliable. The more reliable means were obtained between the latitude limits of  $\pm 65^\circ$  where there were 34914 values 1961 of which were on land. The accuracy of each of the mean  $1^\circ \times 1^\circ$  anomalies was computed from the following expression:

$$m(1^\circ \times 1^\circ) = \frac{\sum_{i=1}^n m_i}{n} \cdot \frac{81}{n} \cdot \frac{1}{2.27} \quad (22)$$

where  $n$  was the number of points used in forming the mean,  $m_i$  is the standard deviation of the point value, and 2.27 was an empirical factor defined to give values of  $m(1^\circ \times 1^\circ)$  that were consistent with more rigorously derived estimates. No mean value was estimated if  $n$  was less than 40. To identify such blocks a  $m$  value of 999.0 was assigned. The location of 29880  $1^\circ \times 1^\circ$  values where the standard deviation is  $\leq 6$  mgals is shown in Figure 42.

The altimeter derived  $1^\circ \times 1^\circ$  mean anomalies were compared to our most recent set of  $1^\circ \times 1^\circ$  anomalies based on terrestrial data (the January 1983 set) which is described by Rapp (1983). Several comparisons have been made that vary with the following criteria: maximum standard deviation of altimeter anomaly; maximum standard deviation of terrestrial anomaly and the limit on the maximum difference allowed in the comparisons. The results of these comparisons are given in Table 13. No comparisons are made if a block is on land. Comparisons are only made between the latitude limits  $\pm 65^\circ$ .

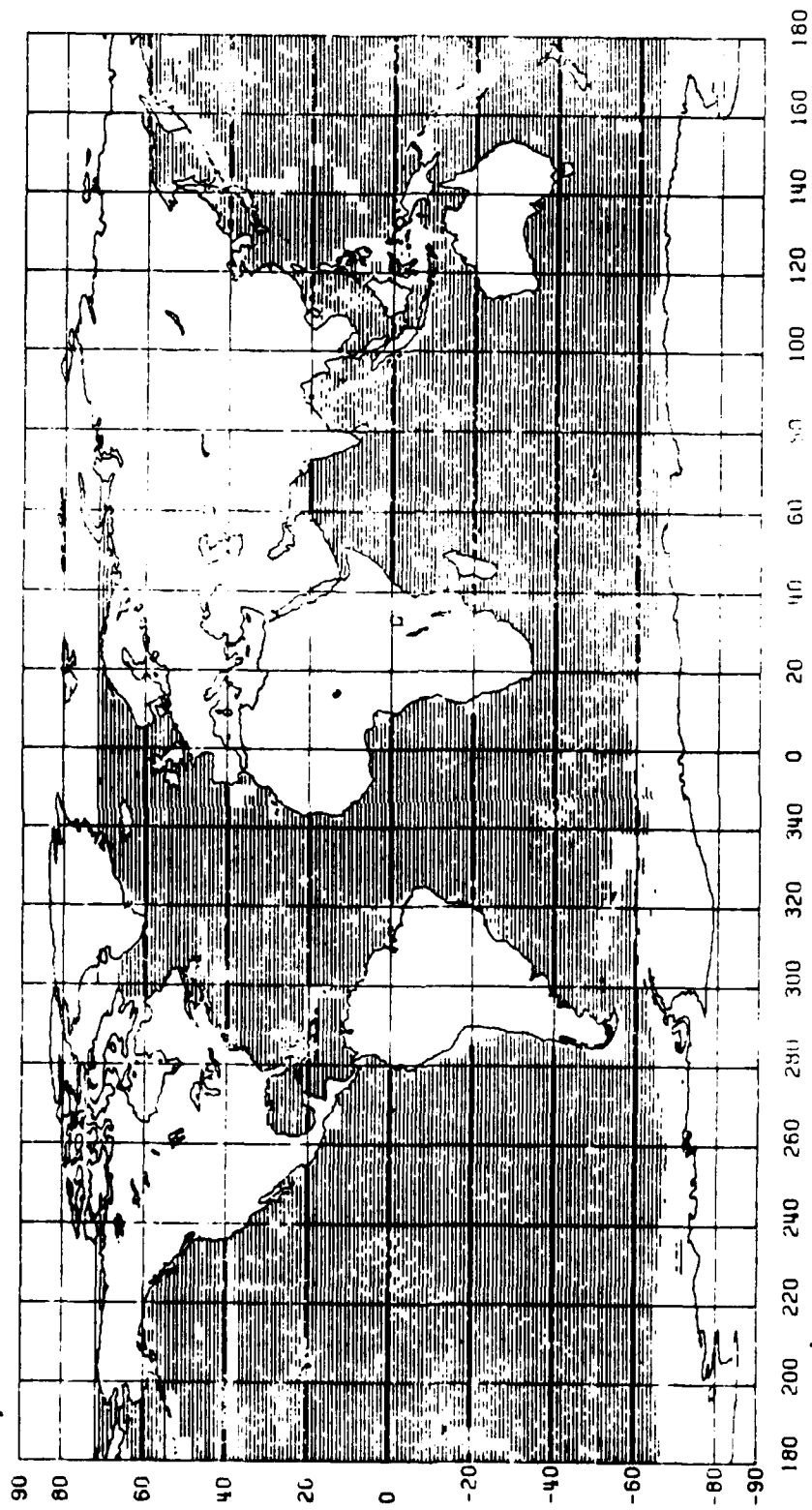


Figure 42  
Location of 29880 Altimeter Derived 1°x1° Anomalies with Standard Deviations  $\leq$  6 mgals

Table 13  
 Comparison of Altimeter Derived 1°x1° Anomalies to Terrestrial Estimates  
 (January 1983 Data; All anomaly values are in mgals)

Solution Criteria					
SD Alt "	—	12	12	12	7
SD Terr "	—	20	15	15	15
Diff "	—	—	—	25	25
<b>Quantity</b>					
Num of Diff	21933	19419	11463	11183	10139
Min Val (Alt)	-259	-259	-259	-259	
Min Val (Terr)	-282	-282	-282	-282	
Max Val (Alt)	167	167	167	167	
Max Val (Terr)	192	192	192	192	
RMS Val (Alt)	24.5	24.5	27.8	27.5	23.2
RMS Val (Terr)	27.2	27.0	29.7	28.8	24.5
Mean (A-T)	0.1	0.1	0.5	0.4	0.4
RMS Diff	*11.7	*10.7	*9.3	*7.7	*7.3
RMS SD (Alt)	5.4	5.2	5.4	5.3	4.8
RMS SD (Terr)	15.4	14.2	10.9	10.9	10.9
Max SD (Alt)	28	12	12	12	7
Max SD (Terr)	65	20	15	15	15
Min SD (Alt)	4	4	4	4	4
Min SD (Terr)	1	1	1	1	1
Min Diff (A-T)	-131	-131	-86	-25	
Max Diff (A-T)	130	88	88	24	

Figure 43 shows the location of 905 values where the difference between the altimeter derived anomalies (with standard deviation less than or equal to 12 mgals) and the terrestrial values of the January 1983 tape (with no standard deviation limit on the terrestrial value) exceeded 25 mgals. A total of 21054 anomalies were compared in this analysis.

Many of these disagreements are due to errors in the terrestrial data. We have estimated a number of new 1°x1° terrestrial values using data not available in the January 1983 up date. A summary of some of these comparisons is given in Table 14.

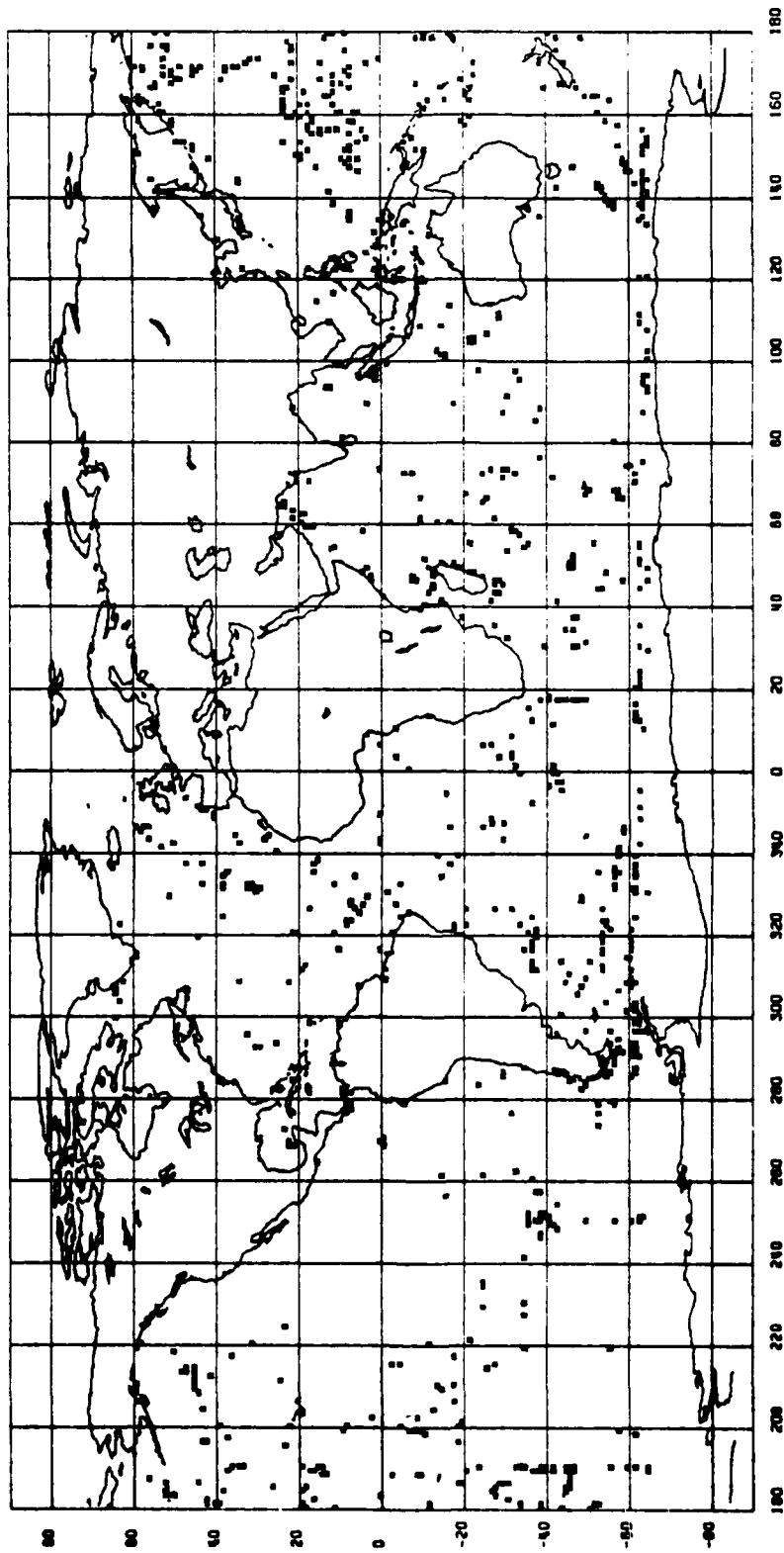


Figure 43  
Location of 1°x1° Anomalies When the Differences Between the Altimeter Derived Values and Terrestrial  
Estimates Exceeds 25 mignals

Table 14  
 Selected Comparisons of 1°x1° Anomalies from Altimeter Estimates,  
 January 1983 Data Tape, and New Terrestrial Estimates  
 (units are mgals)

◆	λ	Δg Altimeter	Δg January 83	Difference	New Estimate	Source
52	175	-22±9	70±24	-92	-66±25	A
44	350	18±7	-40±11	58	35±15	B
43	350	39±8	-13±14	52	33±10	B
31	292	-17±4	-105±13	88	-20±10	C
30	292	-18±4	-73±15	55	-25±10	C
23	268	-8±5	-75±15	67	-13±20	D
1	6	22±7	108±15	-86	-5±10	E
-3	327	2±5	58±16	-56	-10±10	E
-5	147	21±6	-23±6	44	4±10	F
-6	325	0±5	54±8	-54	-20±20	E
-15	354	6±5	46±15	-40	-15±20	E
-31	326	16±6	-55±24	-71	20±15	E
-32	1	7±4	62±16	-55	22±10	E
-34	316	-17±5	42±24	-59	-25±10	E
-38	172	9±4	-49±14	58	11±14	G
-38	173	22±5	-26±18	48	21±8	G
-38	180	29±5	-11±21	40	35±8	G
-38	181	31±4	-22±17	53	33±8	G
-38	189	-2±5	-45±19	43	10±8	G
-41	0	-10±7	65±20	-75	19±20	E
-41	359	-31±5	72±25	-103	19±20	E
-51	181	-19±5	64±19	-83	-18±7	G

The sources of the new anomaly data are as follows:

- A: Watts, A., Gravity Field of the Northwest Pacific Ocean Basin and It's Margin, Chart MC-10, Geological Society of America, Boulder, Colorado, 1975
- B: Torge, W., et al., 6'x10' Free Air Anomalies of Europe Including Marine Areas, Geophysical Researchers, Vol. 7, Nos. 1/2, 1984
- C: Watts, A., (Ship data, private communication, 1983)
- D: Dehlinger, P., Marine Gravity, Elsevier Oceanography Series, 1978
- E: Kogan M.G., and A. Watts, Free Air Gravity Field of the South Atlantic Ocean, map published under the auspices of the USSR Academy of Sciences, 1983

F: Watts, A, J. Bodino, C. Bowin, A Geophysical Atlas of the East and Southeast Asian Seas, Free Air Gravity Field, Chart MC-25, The Geological Society of America, Boulder, Colorado, 1978

G: Davey, F. and A. Watts, Free-Air Gravity Field of the New Zealand Area, Chart MC-48, The Geological Society of America, Boulder, Colorado, 1983

Inspection of Table 14 clearly shows that the new altimeter estimates agree much better with the new terrestrial estimates than with the values available in the January 1983 terrestrial data tape.

If we consider Table 13, the best agreement between the terrestrial data and the altimeter data is  $\pm 7.3$  mgals which is for the case when unreliable values in both data sets are discarded. This value is substantially smaller than the expected value of  $\pm 11.9$  mgals based on the average accuracy of the altimeter anomalies and the terrestrial anomalies.

#### 0.5x0.5 Mean Anomaly Determination

For future applications in the development of high degree spherical harmonic expansions we will need 0.5x0.5 mean gravity anomalies. Such values can easily be computed from our point grid data in a manner analogous to the 1°x1° mean value computation. In this case all available points in the 0.5 block were meaned. The maximum number of points would be 25. The minimum number of points for which a mean was determined was 13. The 0.5x0.5 means were determined for the northern hemisphere, the southern hemisphere and then merged. Some basic statistics on this set are given in Table 15 for two cases selected on the basis of the anomaly standard deviation. In making the statistics we have no easy way to eliminate land values. We know from our 1°x1° data set that there were 2364 1°x1° anomalies on land or about 9456 0.5x0.5 mean values. The RMS value of  $\pm 26.4$  mgals is slightly smaller than the RMS value of the point anomalies ( $\pm 28.6$  mgals) and higher than the RMS value of all the 1°x1° mean anomalies ( $\pm 22.8$  mgals).

The 0.5 anomalies computed from the point predictions were compared to terrestrial estimates for the areas described earlier in this report: Japan Trench, Puerto Rico Trench and the Blake Plateau. (See Tables 2, 3, and 4). No substantial difference was found between the new results and the ones described in these tables.

The accuracy estimates of the 0.5 anomalies were computed in an empirical way similar to that done for the 1°x1° anomalies. The overall accuracy of  $\pm 8$  mgals may be somewhat smaller than expected from a more rigorous treatment of the prediction process.



Table 15  
Basic Statistics on 0:5x0:5 Mean Anomalies Derived from the Altimeter Data  
(units are mgals)

	Northern Hemisphere	Southern Hemisphere	Globally
Number*	59706	89964	149670
RMS Ag	30.04	23.6	26.4
Max Ag	319	203	319
Min Ag	-286	-241	-286
Max SD	55	52	55
Min SD	4	4	4
RMS SD	8.0	8.0	8.0
Number†	59346	89481	148827
RMS Ag	29.8	23.3	26.1
Max Ag	319	193	319
Min Ag	-286	-241	-286
Max SD	30.0	30.0	30.0
Min SD	3.7	4.4	3.7
RMS SD	7.5	7.7	7.6

\* All values are considered

† Only values where the standard deviation  $\leq$  30 mgals are considered

In making these statistics we have no easy way to eliminate land values. We know from our 1°x1° data set that there were 2364 1°x1° anomalies on land or about 9456 0:5x0:5 mean values. The RMS value of  $\pm$  26.4 mgals is slightly smaller than the RMS value of the point values ( $\pm$  28.6 mgals) and higher than the RMS value of all the 1°x1° mean anomalies ( $\pm$  22.8 mgals).

The 0:5 anomalies computed from the point predictions were compared to terrestrial estimates for the areas described earlier in this report: Japan Trench, Puerto Rico Trench and Blake Plateau. (See Tables 2, 3, and 4). No substantial difference was found between these new results and the ones described in these tables.

The accuracy estimates of the 0:5 anomalies was computed in an empirical way similar to that done for the 1°x1° anomalies. The overall accuracy of  $\pm$  8 mgals may be somewhat smaller than expected from a more rigorous treatment of the prediction process.

#### Potential Coefficient Behavior

The eighth of a degree data set can provide information on the behavior of potential coefficients used to describe the earth's gravitational potential. This is done by examining the power spectra determined in local areas using Fourier

analysis procedures (Forsberg, 1984). Let the disturbing potential  $T$  be represented in fully normalized potential coefficients  $\bar{C}_{\ell m}$ ,  $\bar{S}_{\ell m}$  as follows:

$$T(r, \bar{\phi}, \lambda) = \frac{kM}{r} \sum_{\ell=2}^{\infty} \left(\frac{a}{r}\right)^{\ell} \sum_{m=-\ell}^{\ell} \bar{C}_{\ell m} \bar{Y}_{\ell m}(\bar{\phi}, \lambda) \quad (23)$$

where 
$$\bar{Y}_{\ell m}(\bar{\phi}, \lambda) = \begin{cases} \bar{P}_{\ell m}(\sin \bar{\phi}) \cos m\lambda; & m \geq 0 \\ \bar{P}_{\ell m}(\sin \bar{\phi}) \sin m\lambda; & m < 0 \end{cases}$$

The potential degree variances of  $T$  are designated  $\sigma_{\ell}$ :

$$\sigma'_{\ell} = \left(\frac{kM}{r}\right)^2 \left(\frac{a}{r}\right)^{2\ell} \sum_{m=-\ell}^{\ell} \bar{C}_{\ell m}^2 \quad (24)$$

where  $\sigma_{\ell}$  is formally the spectrum at radius  $r$ . The units of  $\sigma_{\ell}$  will be in some geopotential unit such as (1 kgal m = 1gpu). The unitless degree variances are defined as  $\sigma_{\ell}$ :

$$\sigma_{\ell} = \left(\frac{a}{r}\right)^{2\ell} \sum_{m=-\ell}^{\ell} \bar{C}_{\ell m}^2 \quad (25)$$

Comparing (24) and (25) we have:

$$\sigma'_{\ell} = \left(\frac{kM}{r}\right)^2 \sigma_{\ell} \quad (26)$$

Gravity anomalies are related to the disturbing potential by the following spherical approximation:

$$\Delta g(r, \bar{\phi}, \lambda) = -\frac{\partial T}{\partial r} - \frac{2}{r} T \quad (27)$$

Using (23) in (27) we can write:

$$\Delta g(r, \bar{\phi}, \lambda) = \frac{kM}{r^2} \sum_{\ell=2}^{\infty} (\ell-1) \left(\frac{a}{r}\right)^{\ell} \sum_{m=-\ell}^{\ell} \bar{C}_{\ell m} \bar{Y}_{\ell m}(\bar{\phi}, \lambda) \quad (28)$$

The anomaly degree variances on a sphere of radius  $a$  would be:

$$c_{\ell} = \left(\frac{kM}{a^2}\right)^2 (\ell-1)^2 \sigma_{\ell} \quad (29)$$

or

$$c_{\ell} = \frac{(\ell-1)^2}{a^2} \sigma_{\ell} \quad (30)$$

Since  $kM/a^2 \approx \gamma$  (an average value of gravity taken as 979.8 gals) we can also write (29) as:

$$c_{\ell} = \gamma^2 (\ell-1)^2 \sigma_{\ell} \quad (31)$$

We can also talk of spatial covariance function  $K(\psi, r_p, r_q)$  involving the disturbing potential. In the planar case we can write  $K(s, z_p, z_q)$  where  $s = \psi R$  and  $z$  are elevations above a reference plane. Given the covariance function  $K(s)$  (we assume  $z_p = z_q = 0$ ) the power spectrum (or power spectral density) can be written as (Forsberg, eq (2.28), 1984):

$$\phi_{TT}(\omega) = 2\pi \int_0^{\infty} sK(s)J_0(\omega s)ds \quad (32)$$

where  $\omega$  is a continuous frequency function and  $J_0$  is the Bessel function of zero order. The integral defines the Hankel transform ( $\phi_{TT}(\omega)$ ) of  $K(s)$  (Papoulis, p. 140, 1981). This is equivalent to a Fourier Transform when circular symmetry is assumed, as we do for covariance functions. If  $K(s)$  is given in potential units squared (e.g.  $\text{gpu}^2$ ) and if  $s$  is given in angular degrees the units of  $\phi_{TT}(\omega)$  will be  $\text{gpu}^2 \text{deg}^2$ . Forsberg (ibid) shows that:

$$\sigma_{\ell} = (\ell + \frac{1}{2}) \frac{1}{R^2} \frac{1}{2\pi} \phi_{TT}\left(\omega = \frac{\ell + \frac{1}{2}}{R}\right) \quad (33)$$

where  $R$  is a mean earth radius. The anomaly degree variances,  $c_{\ell}$ , can also be found from the psd of the anomaly covariance function:

$$c_{\ell} = (\ell + \frac{1}{2}) \frac{1}{R^2} \frac{1}{2\pi} \phi_{gg}\left(\omega = \frac{\ell + \frac{1}{2}}{R}\right) \quad (34)$$

where the units of  $\phi_{gg}$  would be  $\text{mgal}^2 \text{deg}^2$  if the anomalies are in  $\text{mgal}$  and  $s$  is in degrees. The value of  $\sigma_s$  can be found using (29) and (34):

$$\sigma_s = \frac{1}{\left(\frac{\text{km}}{a}\right)^2} \frac{(s+\frac{1}{2})}{(s-1)^2} \frac{1}{2\pi} \phi_{gg} \left(\frac{s+\frac{1}{2}}{R}\right) \quad (35)$$

Assuming  $\phi_{gg}$  is given in  $(\text{mgal deg})^2$  and  $1^\circ$  angular degree corresponds to 111 km, (29) becomes:

$$\sigma_s = 5.02 \times 10^{-17} \frac{s+\frac{1}{2}}{(s-1)^2} \left\{ \phi_{gg} \left(\frac{s+\frac{1}{2}}{R}\right) (\text{mgal deg})^2 \right\} \quad (36)$$

Our problem now is to estimate the anomaly covariance function and then compute its psd and then compute  $\sigma_s$  from (36). This procedure can be carried out in local areas using our eighth degree data set. We have done this using a program prepared by Forsberg that takes an input grid and carries out a 2 dimensional Fourier analysis. The individual spectra are then averaged to obtain a specific set of values for  $\phi_{TT}$  and  $\phi_{gg}$ .

For our application we decided to compute  $\sigma_s$  for  $15^\circ \times 15^\circ$  areas using the eighth degree data. To reduce spectral leakage we removed from our anomalies the anomalies implied by the GEM9 potential coefficients taken to degree 20. If NN is the number of points in one direction of the grid with a spacing of DFI (in degrees) the frequency spacing,  $\Delta f$  is:

$$\Delta f = \frac{1}{(NN)(DFI)} \quad (37)$$

The frequencies that can be determined will be  $i\Delta f$  where  $1 \leq i \leq (NN/2)$ . The corresponding spherical harmonic degrees are:

$$s_i = i \ 360^\circ \ \Delta f \quad (38)$$

Equation (38) is the same as (c11) in Appendix C. In our specific case  $NN = 481$ ,  $DFI = 0.125$  so that  $s = 6i$ . The highest spherical harmonic degree of possible interest could be 1440 (i.e.  $6(481/2)$ ). However earlier discussion showed that we should restrict our analysis to maximum  $s$ 's on the order of 900.

The first set of spectrum calculations were made for the eight geographic areas shown in Figure 44 where there are a total of 104 spectra.

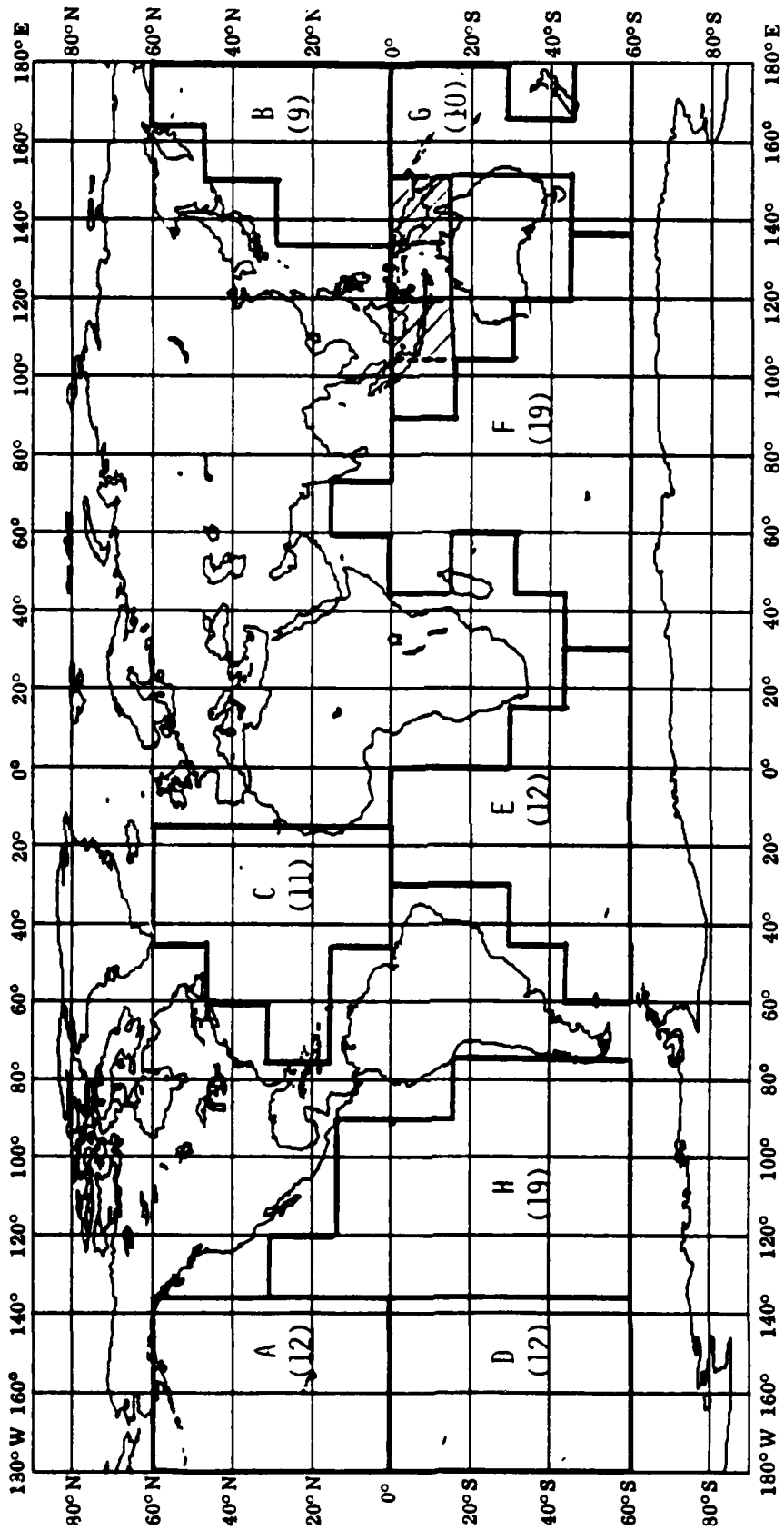


**Figure 44**  
 Location of Areas in Which Local Spectra Were Computed. Number Below Letter is the Number of Spectra Computed for Each Area.

The spectra from each 15°x15° run were computed and the results meaned. The results for each area are plotted in Figure 45. Also plotted in this figure is the spectrum due to Kaula's Rule on the potential coefficient decay and the spectra implied by the anomaly degree variance model of Tscherning and Rapp (1974). The Kaula rule spectrum is:

$$\sigma_{\ell} = (2\ell+1) \left( \frac{10^{-5}}{\ell^2} \right)^2 \quad (39)$$

The Tscherning/Rapp spectrum is:

$$\sigma_{\ell} = \frac{A}{(\ell-1)^2 \gamma^2} \frac{(\ell-1)}{(\ell-2)(\ell+24)} s^{\ell+2} \quad (40)$$

where  $A = 425.28 \text{ mgal}^2$  and  $s = 0.999617$ .

The spectrum with the most power is that of Area G. This area is dominated by anomalies associated with trenches. Area H is the area that has the least power. This area is characterized by small, slowly changing, gravity anomalies. The other areas have spectra that fall between the two extremes. The dispersion between the spectra is the greatest out to about degree 360 after which six of the eight areas have spectra that agree quite well. The spectra implied by the two models represent well the actual spectra in area B and G out to about degree 300 after which the models contain too much power.

Next the 104 spectra were divided into three categories that were selected to describe the variability of the anomaly field. To do this the range of the standard deviations (SD) of the anomalies with respect to GEM9 was divided by three to yield the following categories: Rough Area ( $43 < \text{SD} \leq 59 \text{ mgals}$ ); Mild Area ( $23 < \text{SD} \leq 43 \text{ mgals}$ ); Smooth Area ( $4 \leq \text{SD} \leq 23 \text{ mgals}$ ). The number of spectra in each area was: Rough (9), Mild (17), Smooth (78). The mean SD for each area was: Rough ( $\pm 52.1 \text{ mgals}$ ); Mild ( $\pm 29.5 \text{ mgals}$ ); Smooth ( $\pm 12.9 \text{ mgals}$ ). The location of the rough, mild, and smooth spectra is shown in Figure D1 in Appendix D.

The spectra from each group were then plotted as shown in Figure 46 along with the Kaula and Tscherning/Rapp models. The mean of the 104 spectra is also shown. It is clear that the mean spectrum is considerably smaller than expected from the two models. For more meaningful comparisons we computed the RMS coefficient ( $\bar{\sigma}$ ) from the various spectra. We have

$$\bar{\sigma}_{\ell}(C, S) = \sqrt{\frac{\sigma_{\ell}}{2\ell+1}} \quad (41)$$

Values of  $\bar{\sigma}_{\ell}$  are compared in Table 16.

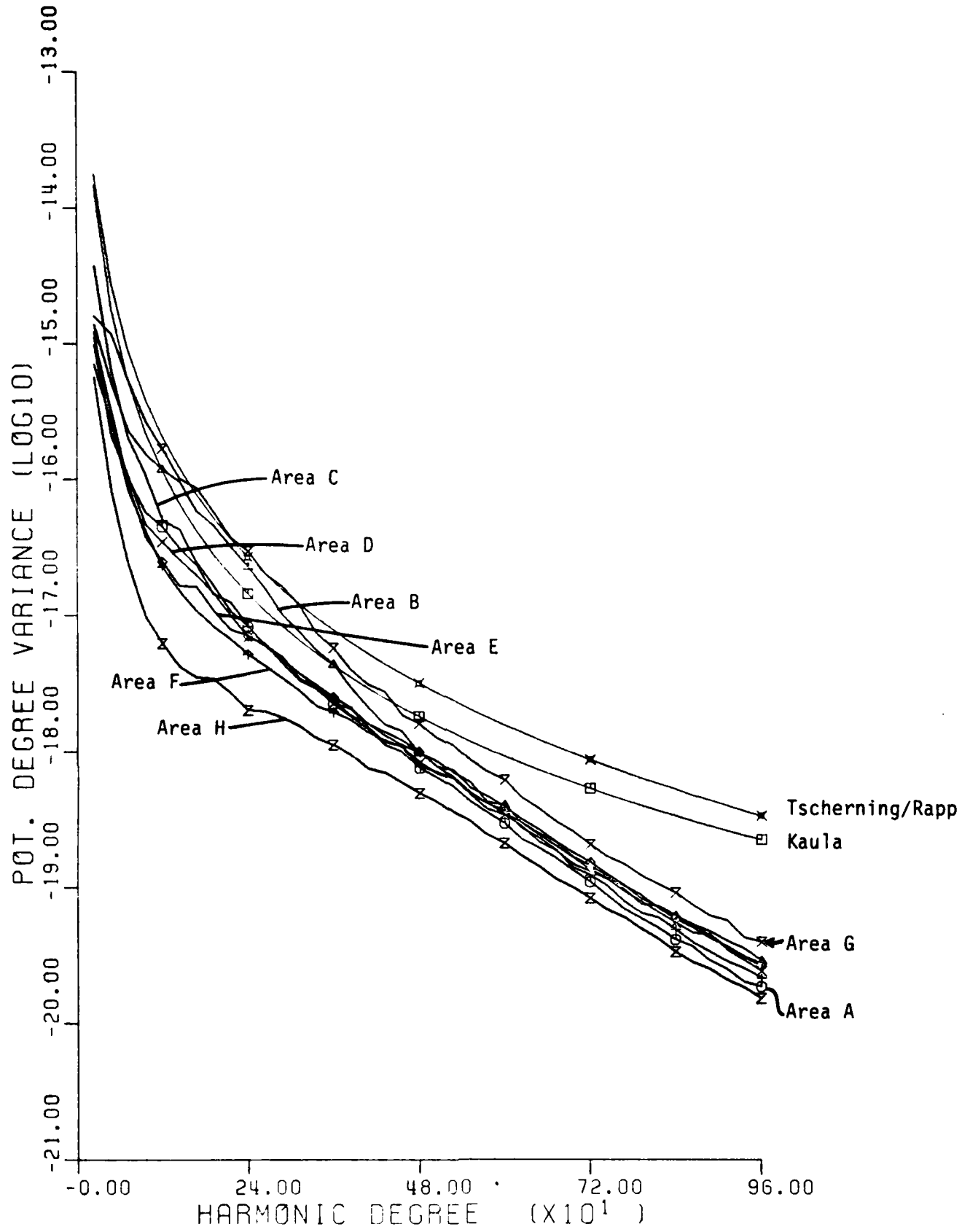


Figure 45  
 Geopotential Spectra for Eight Areas Based on the Eighth Degree Anomaly  
 Data Set

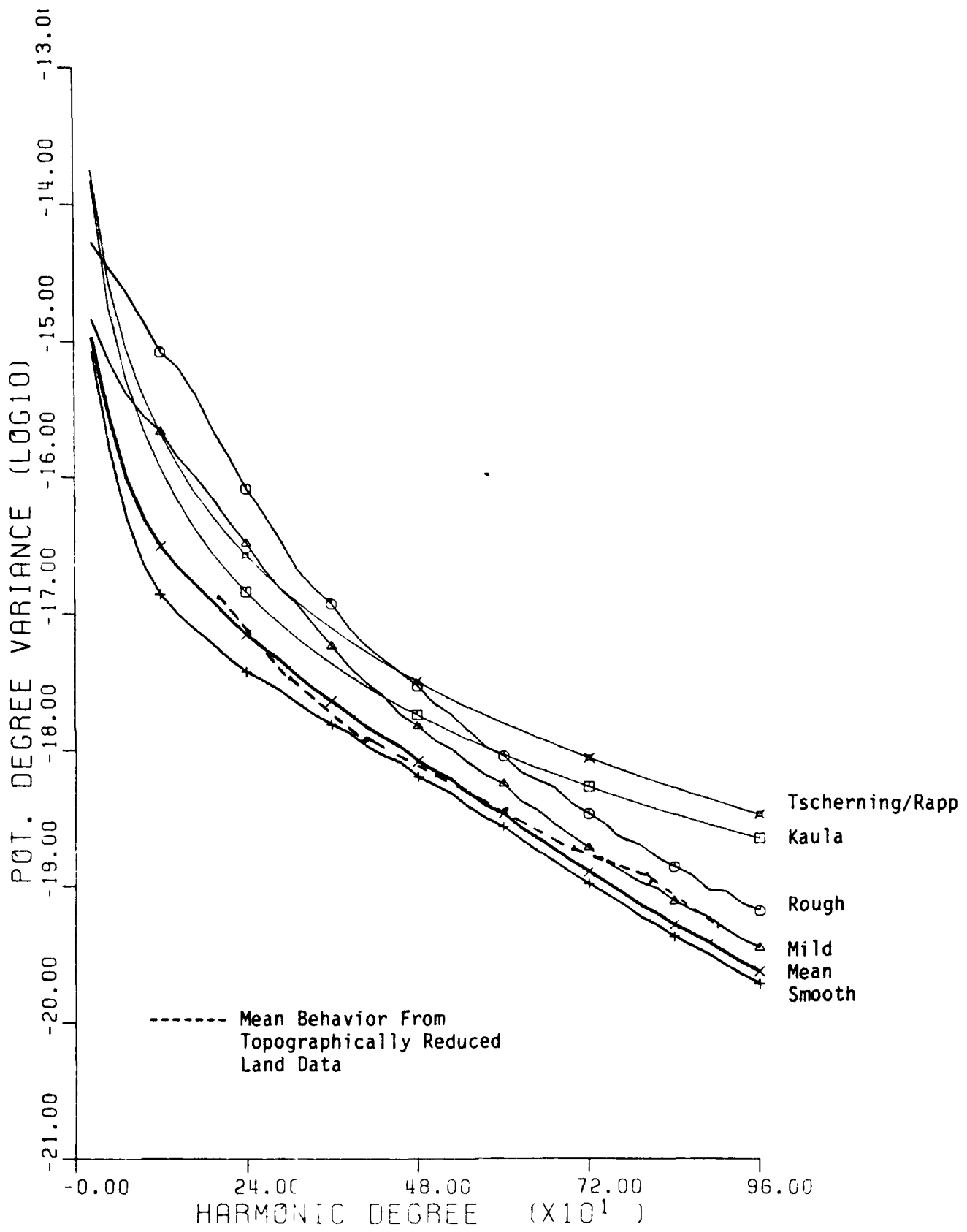


Figure 46  
 Geopotential Spectra for Smooth, Mild, and Rough Areas



Table 16. Comparison of RMS Coefficient Variation  
(All Values x10<sup>11</sup>)

<u>Degree</u>	<u>Mean from Spectra</u>	<u>Kaula's Rule</u>	<u>Ratio</u>
96	50.6	108.5	2.15
216	14.6	21.4	1.47
312	7.5	10.3	1.37
408	4.3	6.0	1.41
504	2.6	3.9	1.49
600	1.7	2.8	1.65
696	1.0	2.1	1.98
792	0.7	1.6	2.35
912	0.4	1.2	2.85

We recognize in these spectra that our computed values are only representative of the ocean regions of the world. Forsberg (1984) has computed spectra for four land areas in the United States using gravity anomalies given on a 2'x2' grid. The four areas studied by Forsberg were in Ohio, Colorado, California and New Mexico. The areas were classified as follows: Ohio: lowland/moderately hilly; Colorado: alpine area west of Denver and Colorado Springs; California: mixed area containing the central parts of the Sierra mountains and a part of the California Valley; New Mexico: 4°x4° area covering most of the state. The anomalies were first corrected by removing the Bouguer anomalies implied by the Dec 1981 potential field to 180 and a spherical harmonic expansion of the topography to degree 180. A mean curve was estimated from Figure 20 of Forsberg (1984) and plotted in Figure 46. The curve falls near the mean and mild curves estimated from the ocean data.

If the topographic effects had not been removed from the Colorado, California and New Mexico data, the spectra would be more varied and would show more power than the spectra computed from the corrected anomalies. This is clearly seen from Figure 21 of Forsberg (ibid).

Since the oceans cover 70% of the earth's surface, and since rugged topographic areas are not the normal continental structure, the mean global spectrum could be represented by a spectrum somewhat between the mean and mild area spectra shown in Figure 46. One could find improved spectrum models by fitting to these curves.

A simple computation assumes the potential power spectrum may be represented in the general form:

$$\sigma_t = \frac{A}{f^B} \quad (42)$$

where, for example, B is 3 for the Kaula rule. Values of B have been determined from the data shown in Figure 45 with selected results shown in Table 17.

Table 17. Values of B in the Potential Decay Law

Data	Range of $l$	B
Forsberg	200 to 500	3.38
	600 to 1455	3.74
	200 to 1455	3.65
Average of 104 Spectra	24 to 500	2.76
	24 to 792	3.63
	24 to 960	4.04
	100 to 700	4.56
	100 to 792	3.77
	500 to 792	4.00
	792 to 1440	5.69

From the Forsberg data we see an early decay of 3.38 which increases to 3.74 for degrees 600 and above. In considering the altimeter data we must recall that the higher frequencies have been smoothed by the collocation process and that the analysis on page 72 gave the highest estimable degree to be on the order of  $l=950$ . The slopes shown for the altimeter analysis in Table 17 indicate the more rapid decay at the higher frequencies. This behavior can be caused by several factors: 1. the effect of the smoothing caused by the collocation process and 2. the fact that the density anomalies are farther away from the surface in the ocean case than in the land case. Based on the comparison with the slopes of the Forsberg data, we might conclude that the altimeter derived spectra shown in Figure 46 are reasonable up to degree 800 after which they probably decay too rapidly.

#### Anomaly Degree Variances

An alternative to the analysis of potential coefficient behavior is the study of anomaly degree variances. Such values can be computed from the potential coefficient spectrum using equation (31). The anomaly degree variance implied by the Kaula Rule is:

$$c_l = \frac{192}{l+1.5} \text{ mgal}^2 \quad (43)$$

The Tscherning/Rapp model was given in terms of anomaly degree variances as:

$$c_l = \frac{A(l-1)}{(l-2)(l+B)} s^{l+2} \quad (44)$$

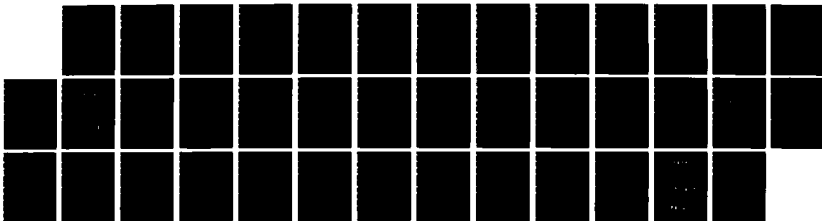
AD-A166 593

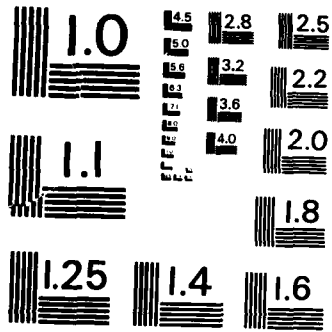
DETAILED GRAVITY ANOMALIES AND SEA SURFACE HEIGHTS  
DERIVED FROM GEOS-3/SE. (U) OHIO STATE UNIV COLUMBUS  
DEPT OF GEODETIC SCIENCE AND SURVEYING R H RAPP AUG 85  
OSU/DGSS-365 AFGL-TR-85-0191 F/G 8/5

2/2

UNCLASSIFIED

ML





MICROCOPY RESOLUTION TEST CHART  
NATIONAL BUREAU OF STANDARDS - 1963 - A

where A, B, and s have been defined after equation (40). To be exact, the  $c_s$  values defined by (44) refer to a mean earth radius of 6371 km instead of an equatorial radius. We will ignore the distinction here.

Table 18 contains the anomaly degree variances from the eight geographic areas discussed earlier. We have also included the  $c_s$  values computed from the two models given in (43) and (44). And we also have computed the  $c_s$  values from the Rapp (1981) expansion to degree 180; the GEM10C potential coefficients to degree 180; and from a set (B1) of potential coefficients to degree 250 estimated by Hajela (1984) in an "optimal" way using the same adjusted anomalies as Rapp (1981). All values are given in Table 18.

Table 18 Anomaly Degree Variances by Geographic Areas, From Models, and Potential Coefficient Sets. Units are  $\text{mgal}^2$ .

	Degree (#)								
	48	72	96	120	144	168	192	216	240
Kaula	3.96	2.61	1.97	1.58	1.32	1.13	0.99	0.88	0.80
Tsch/Rapp	5.92	4.37	3.45	2.84	2.41	2.09	1.84	1.64	1.47
Rapp(1981)	2.64	3.06	2.45	2.60	2.13	1.88	—	—	—
Hajela(1984)	2.33	2.78	2.11	2.17	1.57	1.08	0.66	0.48	0.29
GEM10C	2.62	2.10	1.56	1.33	1.10	1.10	—	—	—
Region A	0.44	0.49	0.50	0.61	0.61	0.63	0.50	0.56	0.46
B	1.10	1.11	1.34	1.61	1.89	1.56	1.59	1.41	1.24
C	1.33	0.98	0.94	0.68	0.84	0.66	0.58	0.48	0.46
D	0.47	0.50	0.41	0.47	0.50	0.53	0.51	0.44	0.38
E	0.67	0.45	0.33	0.34	0.32	0.43	0.38	0.35	0.39
F	0.56	0.40	0.36	0.31	0.30	0.29	0.29	0.30	0.28
G	2.53	2.60	2.37	2.30	1.98	2.29	2.01	1.65	1.62
H	0.17	0.11	0.09	0.08	0.08	0.09	0.12	0.12	0.11
Rough	7.33	11.32	12.26	11.27	12.70	11.10	8.06	6.24	4.53
Mild	1.51	2.02	2.43	2.94	2.75	2.74	2.49	2.08	1.79
Smooth	0.36	0.25	0.20	0.19	0.19	0.21	0.21	0.21	0.21
Mean of 104	0.59	0.48	0.43	0.42	0.43	0.44	0.44	0.41	0.38

In comparing the results we must keep in mind that the two models and the spherical harmonic sets represent the earth as a whole while the other values are representative of the ocean regions alone. At degree 72, the value of  $c_s$  should be between 2 to 3  $\text{mgal}^2$  as inferred from the spherical harmonic expansions. However, from the ocean spectra  $c_s$  is on the order of 0.5  $\text{mgal}^2$ . In principle the differences might be caused by the land data which is included in the spherical harmonic expansions. Whether a factor of 5 (at degree 72) between the two types of solutions is reasonable is not clear.

Estimates of  $c_s$  can be obtained from Figures 20 and 21 of Forsberg (1984). At degree 200  $c_s$  is approximately 0.5  $\text{mgal}^2$  when using terrain corrected data and 1.9  $\text{mgal}^2$  when the non-corrected data is used. The 0.5  $\text{mgal}^2$  is

consistent with the value of 0.4 mgal<sup>2</sup> found from the mean of our 104 profiles. The increase of  $c_\ell(200)$  to 1.9 mgal<sup>2</sup> indicates the sensitivity of this problem to the terrain.

The major question from this discussion relates to the substantial difference between the  $c_\ell$  values derived from our local spectra and the global spherical harmonic implied values. Is the difference due to the topography? Or is it due to some other factor in the analysis?

### Geoid Undulation Information by Degree Range

The geoid undulation is related to the disturbing potential as follows:

$$N = T/\gamma \quad (44)$$

where  $\gamma$  is a value of gravity.

Using (23) (with  $r = R$ ) the geoid undulation at degree  $\ell$  is:

$$N_\ell(R, \bar{\varphi}, \lambda) = \frac{kM}{R\gamma} \left(\frac{a}{R}\right)^\ell \sum_{m=-\ell}^{\ell} \bar{C}_{\ell m} \bar{Y}_{\ell m}(\bar{\varphi}, \lambda) \quad (45)$$

The undulation variance, per degree, is:

$$\sigma_\ell^2(N) = \left(\frac{kM}{R\gamma}\right)^2 \left(\frac{a}{R}\right)^{2\ell} \sigma_\ell^2 \quad (46)$$

If we let  $\gamma = kM/R^2$  and  $R = a$  we have:

$$\sigma_\ell^2(N) = R^2 \sigma_\ell^2 \quad (47)$$

The geoid undulation variance between degrees  $\ell_1$  and  $\ell_2$  would be:

$$\Delta N^2(\ell_1, \ell_2) = R^2 \sum_{\ell=\ell_1}^{\ell_2} \sigma_\ell^2 \quad (48)$$

The value of  $\sigma_\ell$  has been estimated from our altimeter derived anomaly data using equation (36). It can be computed from the models given by equation (39) and (40), or alternate models such as given by Wagner and Colombo (1979). Brammer and Sailor (1982) have analyzed Seasat altimeter data and terrestrial

gravity data from ship measurements to produce a power law decay model for the potential. This model has been used to compute the geoid undulation information in several degree ranges. These values are shown in Table 18 along with values from our rough, mild, smooth areas and from our average spectrum, as well as from the Kaula rule, the Tscherning/Rapp model, and the Wagner/Colombo model.

We can see the variability of the results depending on the area characteristic (rough, mild, or smooth). The total average results are close to the results for the smooth areas, because the latter dominates in the ocean. The results from the Tscherning/Rapp, Wagner/Colombo, and Kaula models have more power than seen from the local spectra information. (The Tscherning/Rapp and the Wagner/Colombo models are very similiar above degree 100). The Brammer/ Sailor results agree well with our results (i.e. total average) in the ranges 181-360, 361-720, and 721-1000. Because of the geographic dependence on the arc selection or ship tracks the results of Brammer/Sailor will depend on the location of the profiles that were analyzed.

Table 19. Geoid Undulation Information Between Selected Spherical Harmonic Degrees (Units are meters.)

Range of $\ell$	Rough Area	Mild Area	Smooth Area	Total Average	Tscherning Rapp	Wagner Colombo	Kaula	Brammer Sailor
50-100	2.16	.93	.34	.47	1.44	1.17	1.12	1.12
101-180	1.49	.73	.19	.28	0.71	0.68	0.53	0.49
181-360	0.76	.45	.16	.21	0.42	0.40	0.31	0.26
361-720	0.20	.14	.09	.10	0.20	0.19	0.15	0.12
721-1000	0.04	.03	.02	.03	0.08	0.07	0.06	0.04

#### Maximum Anomaly and Sea Surface Height Gradients

We now wish to identify those areas that have the largest changes in the anomalies and sea surface heights. We first computed the east/west and north/south gradients using the 0.5x0.5 mean anomalies or sea surface heights. The total gradient was computed by combining the individual components. The maximum values were identified and then maps of each area were made and specific gradients were computed based on the point data interpolated from the contour maps.

The largest anomaly gradient was found over the Kuril Trench in the northwest Pacific Ocean. This gradient was 6.9 mgal/km near  $\phi = 47.5$ ,  $\lambda = 154.5$ . The anomaly and sea surface height maps in this area are shown in Figure 47. There are a number of areas where the anomaly gradient reaches 5 mgal/km or somewhat higher. Such gradients should be regarded as an average gradient because of the smoothing that has taken place in the data analysis.

The maximum sea surface height gradient was 0.28 m/km. The location of this gradient was near  $\phi = 44:5$ ,  $\lambda = 148:5$ . This is also across the Kuril Trench but not as same location as where the anomaly gradient is a maximum. The above gradient corresponds to a deflection of the vertical of 58".

It would be of interest to prepare a map showing these gradients in some global fashion. However, the only global set of gradients we have is based on 0:5 mean values which may not show enough detail. This needs to be tried.

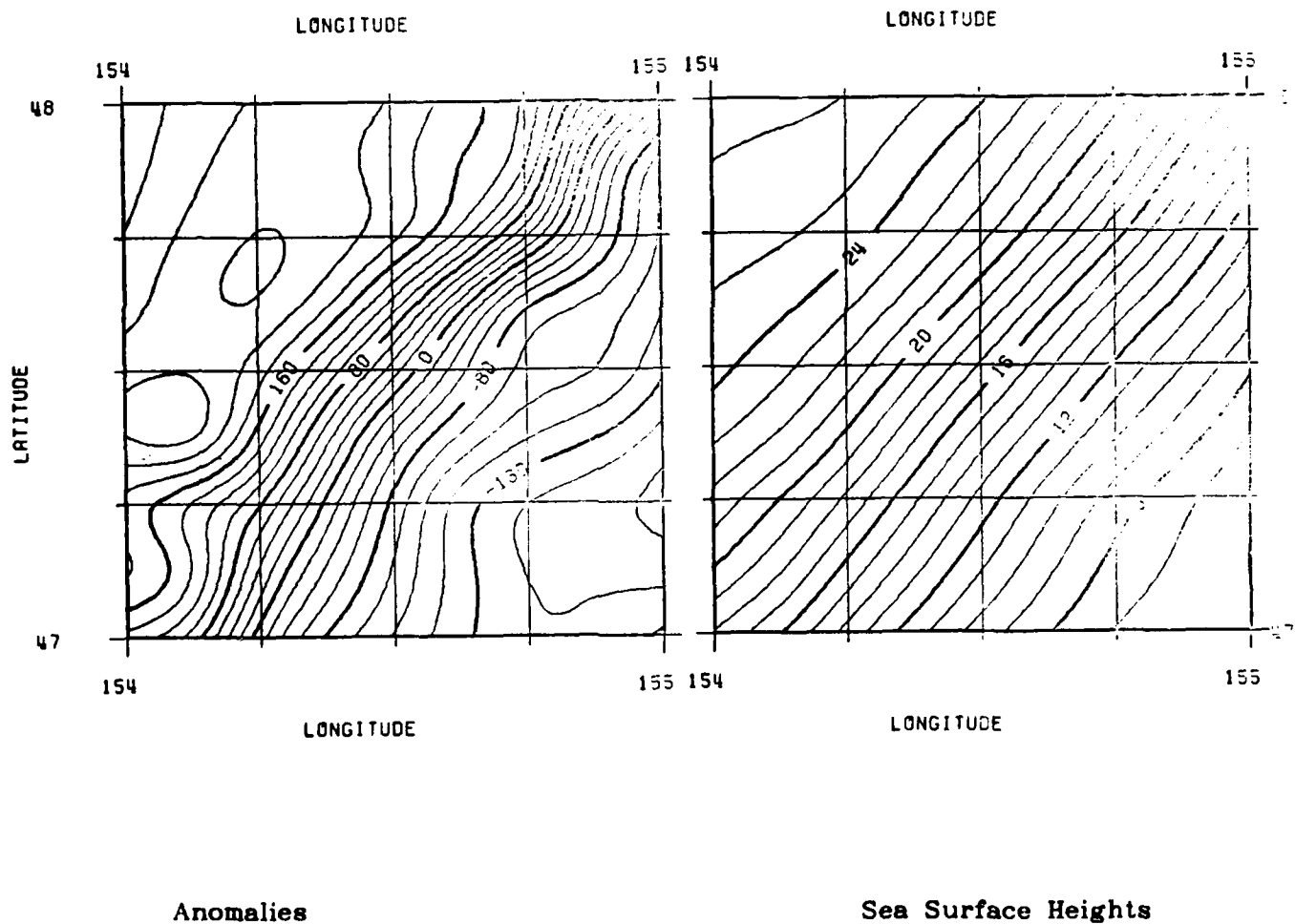


Figure 47  
Anomalies and Sea Surface Heights in the Area with the Maximum Anomaly Gradient



### Point Anomaly Variance

We saw that the root mean square value of the predicted point anomalies (for values with the standard deviation less than or equal to 30 mgals) was  $\pm 28.6$  mgals or a variance of  $818 \text{ mgal}^2$ . This value does not reflect contributions from spherical harmonic degrees above degree 900 (approximately). An estimate of this contribution can be made using anomaly degree variance models. A very approximate estimate (based on a modified Tscherning/Rapp model) is  $200 \text{ mgal}^2$ . Thus we have a point anomaly variance in the ocean areas of about  $1000 \text{ mgal}^2$  or  $\pm 32$  mgal. This is considerably smaller than the  $1795 \text{ mgals}^2$  ( $\pm 42$  mgal) of the original Tscherning/Rapp model.

For other comparisons of the point variance we used the results of Schwarz and Lachapelle (1980) for Canada where they found an average variance of  $1115 \text{ mgal}^2$  ( $\pm 33$  mgals) which agrees well with the altimeter result.

We also calculated the variance from the  $6' \times 10'$  anomalies described by Torge et al (1983) for most of western Europe. In this case we have a variance of  $1218 \text{ mgal}^2$  ( $\pm 35$  mgals). Again this value is reasonably consistent with the altimeter value and the Canadian result.

It seems clear from this brief analysis that the global anomaly variance of  $1795 \text{ mgal}^2$  computed by Tscherning and Rapp in 1974 is too high with a more reasonable value being around  $1100 \text{ mgal}^2$ .

### Summary

In 1982 we completed an analysis of Seasat altimeter data. This analysis included the adjustment of the Seasat arcs to remove orbit error using a crossing arc technique. This data set was used to estimate  $1' \times 1'$  mean gravity anomalies and sea surface heights (approximately geoid undulations). In 1983 Liang carried out an adjustment that merged the Geos-3 altimeter data to the Seasat data. This combined data set contained approximately 6 million altimeter measurements. This data set was analyzed in this paper for an improved determination of the gravity field in ocean area.

The first step taken was to carry out tests for the recovery of mean and point gravity anomalies using the combined Geos-3/Seasat data. These tests were made with  $0.5 \times 0.5$  mean anomaly and point gravity anomaly predictions with the comparison of the predicted values with "ground truth" defined by ship gravity measurements. These tests examined the role of various data selection procedures and the use of different covariance models in the least squares collocation prediction method used to recover the gravity anomalies. These tests clearly indicated the ability of the altimeter data to yield reliable ( $\pm 8$  mgals)  $0.5$  anomalies and promising ( $\pm 10$  mgals) point anomalies. (Actual accuracy estimates will depend on the anomaly behavior in an area and the density of the altimeter data). We found that the Tscherning/Rapp covariance model, with appropriate variance scaling to the altimeter data in a prediction region, gave somewhat better predictions than when a covariance model (with two adjusted parameters) suggested by Jordan (1972) was used. In both cases

the reference field was defined by the spherical harmonic expansion to degree 180 of Rapp (1981). It became clear with these tests that the primary quantity to be predicted should be values of the anomalies and sea surface heights on a point grid. Although such values appear to be point values, they are not because of frequencies missing in the predicted quantity caused by the use of finite data having noise.

Many tests were then carried out to develop an efficient process for the production computation of the point values from the combined altimeter data set. Decisions were made to predict the point values within a  $3^{\circ} \times 3^{\circ}$  block on a  $0.125^{\circ} \times 0.125^{\circ}$  grid using a maximum of about 300 data points. Consequently one data selection and one matrix inversion was needed for each  $3^{\circ} \times 3^{\circ}$  area in the ocean. In order to save computer time we deleted the ability to compute the rigorous accuracy of the predicted quantity. Such a decision reduced our computer requirements by a factor of 8. In addition our data selection was made from a thinned data base created by selecting a single data point for each  $10' \times 10'$  geographic cell. This procedure reduced our original 5.9 million point data base to a 1.1 million point set. The thinned data set reduced our data selection time and reduced track error effects since points were not systematically selected from a single track. However this thinned data set, and the decision to use only 300 data points per block prediction, does reduce the resolution of our prediction over the case of all data being considered with a large number of data points being selected for the prediction. The latter procedure causes other problems, notably increased data selection times and matrix instabilities.

Before the production predictions were started a number of Seasat arcs were re-adjusted to reduce crossover discrepancies. This was done by breaking the arcs into two components and adjusting each arc separately. In our actual computations we still saw examples of remaining track error which easily showed up in anomaly contour maps. In most of these cases the bad arc was identified and the prediction repeated with the bad arc removed.

We also considered the role of sea surface topography (SST) in our predictions. Our initial plan was to remove SST for our altimeter observations using a specific SST model. We decided not to do this because such models may not be representative of the ocean surface at the time of the altimeter measurement (or general time of the altimeter measurements), and because we did not want our results to be dependent on a specific model. Therefore the predicted sea surface heights refer to a mean sea surface defined by the average time of the altimeter measurements which were in the 1975-1978 time period. The values contain sea surface topography effects. The gravity anomalies that were predicted will contain errors caused by not removing SST from the altimeter measurement. On a point basis, this error was found to be  $\pm 2$  mgal. This error is also to be considered long wavelength reflecting the structure of long term SST.

A total of 2.4 million point values were predicted. Of these 0.2 million had standard deviations greater than  $\pm 30$  mgals. (The standard deviations were estimated considering data density and the roughness of the anomaly field; they were not rigorously computed.) The maximum anomaly was 396 mgal, the minimum value was -300 mgals, and the root mean square point value was  $\pm 28.6$

mgals. The eighth of a degree data set was used to produce a number of anomaly and sea surface height (SST) maps that showed the high frequency information in the predicted quantities, as well as the consistency of the results. The maps clearly show the trenches, seamounts, fracture zones associated with major features of the ocean floor. A number of seamount signatures are clearly seen for which no bathymetric data apparently exists. Contour maps revealed very large anomaly and SST gradients. The largest anomaly gradient was found to be 6.9 mgal/km over the Kuril Trench in the northwest Pacific Ocean. In this area we found an anomaly change of 345 mgals in just 50 km.

The frequency content of the point predictions was examined by carrying out a power spectrum analysis of eight long profiles. This analysis indicated that the average resolution of the predicted data was 0:19 or 21 km. This is somewhat lower resolution than implied by the prediction grid interval of 0:125.

The point anomaly values were used to form 1°x1° and 0:5x0:5 mean anomalies by the averaging of the point values in the specific block. Accuracy estimates for each block were computed in an approximate way. A total of 37419 1°x1° values were estimated. The root mean square standard deviation was ± 5 mgals. These were 29880 values having a standard deviation less than or equal to ± 6 mgals. The 1°x1° data were compared to our latest terrestrial data. Using the more reliable data in each data set, the RMS difference was ± 11 mgals for 19419 values. If one deletes residuals greater than 25 mgals this difference drops to ± 7.7 mgals for 11183 computed values. Comparisons of some anomaly estimates with new terrestrial estimates indicated the reliability of the altimeter derived values.

There were 148827 0:5x0:5 anomalies estimated that had a standard deviation of ± 30 mgals or smaller. The root mean square anomaly value was ± 26 mgals while the root mean square standard deviation was ± 8 mgals.

Our final computation with the data was to calculate the potential coefficient spectrum implied by the anomalies for 104 15°x15° regions. This was done using a procedure developed by Forsberg (1984). These spectra were classified in terms of rough, mild, and smooth areas through the anomaly variance in the 15° block. The smooth areas clearly dominate in the ocean areas (78 smooth, 9 rough, 17 mild). We found that the average spectrum was substantially smaller than implied by Kaula Rule for potential coefficient decay or implied by the Tscherning/Rapp anomaly degree variance model. However the average curve agreed well with the curve from Forsberg based on topographically reduced land data.

The point anomaly variance implied by the predicted altimeter anomalies was about 1000 mgal<sup>2</sup> after considering the influence of neglected high frequency terms. This is considerably less than the 1795 mgal<sup>2</sup> point variance computed by Tscherning/Rapp in 1974. However we saw that this smaller variance is more consistent with the anomaly variance found in Canada and in Europe. We also found that the anomaly degree variances implied by our spectrum computation were considerably smaller at around degree 168 (say) than found from spherical harmonic expansions out to degrees 180 or 240. One would

expect these expansions to yield higher values due to their use of land data in their solution. However it seems unreasonable that the land data could cause the values to differ by a factor of four or more.

The results of this study provide a detailed gravity anomaly field in the ocean areas between latitude limits  $\pm 65^\circ$  excluding certain small sea areas. This data can be a basis for geophysical or geodetic studies that require knowledge of the detailed gravity field. However the detail that we have obtained is not the most that can be extracted from the altimeter data. With additional computer resources more data points could be used in the prediction, and more detail in the actual field could be extracted, as well as actual accuracy predictions made.

A fundamental unresolved question in understanding our results relates to the accuracy of our adjusted altimeter data. Our original Seasat adjustment fixed one long arc in the Atlantic Ocean. The coordinate frame in which this (and other arcs) are defined is that defined for orbit determination with the release by JPL of the geophysical data seconds (GDR). The gravity field (PGS-S3) and station coordinates associated with the GDR are discussed by Lerch et al, (1982). All our adjusted values refer to this arc. If this arc is in error so will all the other arcs and such errors will propagate into the recovered anomalies and sea surface heights. Such problems will be encountered if the bias and tilt adjustments have not removed most of the orbit error. From the comparisons that have been done with ship data we have not found any systematic pattern that would indicate systematic errors caused by poor orbit adjustment. However such comparisons may not reveal errors at the several mgal or several decimeter level. Additional study is needed in orbit adjustment of the altimeter data and the effect on gravity anomaly and sea surface height computation.

We also need to study the smoothing effects introduced in our predictions through the use of the least squares collocation procedure. Do the smoother spectra and the smaller anomaly variances reflect reality, or is there an unaccounted for smoothing that is caused by the collocation process?

We must also develop better models for sea surface topography that are valid for the average time of the altimeter measurements. Our recovered anomalies are contaminated by SST effects that have not been removed from the altimeter measurements. Such errors will primarily be long wavelength because we have averaged the altimeter measurements over several years. Can we develop a procedure to correct the predicted anomalies or must we first correct each altimeter measurement?

The gravity field information obtained in this report (and studies such as carried out by Sandwell (1984), Haxby et al. 1983 and others) clearly reveal the unique role that satellite altimetry can play in the determination of the gravity field of the oceans. However as our accuracy requirements increase, we will find it necessary to seek improvements in our processing algorithms, or understanding of altimeter satellite orbits, sea surface topography, and other such effects for which only approximate models are now available.

## REFERENCES

- Beyer, L., Pisciotto K., and N. Sasnett, "Free-Air Gravity Map of the California Continental Borderland", Sheet 1 in U.S. Geological Survey, Miscellaneous Field Studies, MF-624, 1974.
- Brammer, R.F. and R.V. Sailor, "Preliminary Estimates of the Resolutions Capability of the SEASAT Altimeter", *Geophys. Res. Lett.*, 7, 193-196, 1980.
- Brammer, R. and R. Sailor, "Spectrum Analysis of the Ocean Geoid Using Seasat Altimeter Data and Shipboard Gravity Survey Data", manuscript, The Analytic Sciences Corp, Reading, Mass. 01867, April 1982.
- Brenneke, J. and D. Lelgemann, "Geoid and Gravity Anomalies in the North Sea Area Derived from Seasat Altimeter Data", *manuscripta geodaetica*, Vol. 8, 4, 301-320, 1983.
- Colombo, O., "A World Vertical Network", AFGL-TR-80-0077, AD-A086 011/4, Report No. 296, Dept. of Geodetic Science, The Ohio State University, Columbus, 1980. ADA086011
- Engelis, T., "Analysis of Sea Surface Topography Using Seasat Altimeter Data", Report No. 343, Dept. of Geodetic Science and Surveying, The Ohio State University, Columbus, 1983.
- Engelis, T., "Global Ocean Circulation from Seasat Altimeter Data", *Marine Geodesy*, Vol. 9, No. 1, 45-69, 1985.
- Eren, K., "Spectral Analysis of Geos-3 Altimeter Data and Frequency Domain Collocation", Report No. 297, Dept. of Geodetic Science, The Ohio State University, February 1980.
- Forsberg, R., "Local Covariance Functions and Density Distributions", AFGL-TR-84-0214, AD 7150792, Report No. 356, Dept. of Geodetic Science and Surveying, The Ohio State University, Columbus, 1984.
- Forston, R., "Digital Terrain Data Anomaly Removal Through the Use of an Interactive Fourier Frequency Filtering Process", Defense Mapping Agency Aerospace Center, St. Louis AFS, MO 63118, July 1984.
- Ganeko, Y., "10'x10' Detailed Gravimetric Geoid Around Japan", presented at IAG General Meeting, Tokyo, pub. in *Marine Geodesy*, 1983.
- Hajela, D.P., "Optimal Estimation of High Degree Gravity Field From a Global Set of 1°x1° Anomalies To Degree and Order 250", AFGL-TR-84-0263, Report No. 358, Dept. of Geodetic Science and Surveying, The Ohio State University, 64pp, 1984. ADA156008
- Haxby, W.F., G.D. Karner, J.L. La Brecque, and J.K. Weissel, "Digital Images of Combined Oceanic and Continental Data Sets and Their Use in Tectonic Studies", *EOS*, Trans. American Geophysical Union, Vol. 64, No. 52, 995-1004,

Dec 27, 1983.

- Jordan, S., "Self-Consistent Statistical Models for the Gravity Anomaly, Vertical Deflections, and Undulation of the Geoid", J. Geophys. Res., Vol. 77, 3660-3670, 1972.
- Kogan, M. and A. Watts, "Free-Air Gravity Field of the South Atlantic Ocean", Dept. of Navigation and Oceanography, USSR Ministry of Defense, Institute of Physics of the Earth, USSR Academy of Sciences, 1983.
- Lerch, F. et al., "Gravity Model Improvement Using Geos-3 (GEM9 and 10)", J. Geophys. Res., 84, 3897-3916, 1979.
- Lerch, F.J., J.G. Marsh, S. Klosko, R.G. Williamson, "Gravity Model Improvement for SEASAT", J. Geophys. Res., vol. 87, No. C5, 3281-3296, April 30, 1982.
- Levitus, S., "Climatological Atlas of the World Ocean", NOAA Professored Paper 13, NOAA Fluid Dynamics Lab., Princeton, N.J., 1982.
- Liang, C., "The Adjustment and Combination of Geos-3 and Seasat Altimeter Data", Report No. 346, Department of Geodetic Science and Surveying, The Ohio State University, 1983.
- Moritz, H., "Advanced Physical Geodesy", Herbert Wechmann Verlag Karlsruhe, FRG, 1980.
- Papoulis, A., "Systems and Transforms with Applications in Optics", Robert E. Krieger Publishing Co., Malabar, Florida, 1981.
- Rapp, R.H., "Potential Coefficient and Anomaly Degree Variance Modeling Revisited", AFGL-TR-79-0245, AD-A082 322/9, Report No. 293, Dept. of Geodetic Science, The Ohio State University, Columbus 1979a.
- Rapp, R.H., "Geos-3 Data Processing for the Recovery of Geoid Undulations and Gravity Anomalies", J. Geophys. Res., 84, B4, 3784-3792, 1979b.
- Rapp, R.H., "Global Anomaly and Undulation Recovery Using Geos-3 Altimeter Data", Report No. 285, Department of Geodetic Science, The Ohio State University, Columbus, May 1979.
- Rapp, R.H., "The Earth's Gravity Field to Degree and Order 180 Using Seasat Altimeter Data, Terrestrial Gravity Data, and Other Data", AFGL-TR-82-0019, AD-A113 098/8, Report No. 322, Dept. of Geodetic Science and Surveying, The Ohio State University, Columbus, 1981.
- Rapp, R.H., "A Summary of the Results from the OSU Analysis of Seasat Altimeter Data", Report No. 335, Dept. of Geodetic Science and Surveying, The Ohio State University, Columbus, 1982.
- Rapp, R.H., "The Determination of Geoid Undulations and Gravity Anomalies from Seasat Altimeter Data", J. Geophys. Res., 88, 1552-1562, 1983a.

- Rapp, R.H., "Report of Special Study Group No. 5.39 of IAG: Fundamental Geodetic Constants", presented at the XVIII General Assembly of IUGG, Hamburg, August, 1983b.
- Rapp, R.H., "The Development of the January 1983 1°x1° Mean Free-Air Anomaly Data Tape", Internal Report of the Department of Geodetic Science and Surveying, The Ohio State University, Columbus, 1983.
- Rapp, R.H., "Gravity Field Products from Ocean Altimeter Data", in Proc of AIAA Guidance and Central Conference held in Seattle, August 1984.
- Rowlands, D., "The Adjustment of Seasat Altimeter Data on a Global Basis for Geoid and Sea Surface Height Determinations", Report 325, Dept. of Geodetic Science and Surveying, The Ohio State University, Columbus, 1981.
- Sandwell, D.T., "A Detailed View of the South Pacific Geoid From Satellite Altimetry", J. Geophys. Res., Vol. 89, No. B2, 1089-1104, Feb. 10, 1984.
- Schwarz, K.P. and G. Lachapelle, "Local Characteristics of the Gravity Anomaly", Bulletin Geodesique, Vol. 54, No. 1, 21-36, 1980.
- Torge, W., G. Weber, H.-G. Wenzel, "6'x10' Free-Air Gravity Anomalies of Europe Including Marine Areas", presented to the XVIII IUGG General Assembly, Hamburg, (authors at University of Hannover, SFB 149, FRG), 1983.
- Tscherning, C.C., and R.H. Rapp, "Closed Covariance Expressions for Gravity Anomalies, Geoid Undulation, and Deflections of the Vertical Implied by Anomaly Degree Variance Models", AFCRL-TR-74-0231, AD 786 417, Report No. 208, Dept. of Geodetic Science, The Ohio State University, Columbus, 1974.
- Wagner, C., and O. Colombo, "Gravitational Spectra from Direct Measurements", J. Geophys. Res., 84, B9, 4699-4712, 1972.
- Watts, A. and J. Bodine, "A Geophysical Atlas of the East and South East Asian Seas, (Free Air Gravity Field)", The Geological Society of America, Boulder Colorado, MS-25, 1978.

Appendix A  
Readjustment of Selected Seasat  
Primary Arcs

prepared by Chih-kuo Liang



The Seasat adjustment was originally carried out in two steps, a primary adjustment and a local adjustment. The primary adjustment was a crossing arc adjustment of long arcs to obtain a global network to which the remaining (and mostly) shorter arcs could be adjusted in five geographic regions. The 549 adjusted primary arcs are shown in Figure A1. Although the RMS crossover discrepancy after the adjustment of the primary arcs was  $\pm 28$  cm (Rowlands 1981, p.51) there were 53 arcs where the crossover discrepancies (along the arc) were greater than 40 cm. The location of these arcs is shown in Figure A2. (Of these arcs the largest RMS crossover discrepancy was  $\pm 61$  cm.) The reason for the larger RMS is primarily due to the length of the arc being too long for the radial orbit error to be modeled by the simple bias and tilt term. To reduce this error we decided to readjust these arcs by splitting them into smaller arcs.

The readjustments were regional adjustments. By giving the size of a region, the observations of these 53 arcs were collected only for those observations that fell into the region. Such observations from an arc were collected to form a cut arc. For one cut arc, the crossovers of the cut arc and the remaining primary arcs (excluding the 53 arcs) were found and used to readjust the cut arc by a crossover adjustment. In other words, the readjustment was a crossover adjustment and was separately performed in principle for each cut arc. Practically, all cut arcs within one region were adjusted with one regional adjustment although they were independent of one another.

From Figure A2, we see that most of the high crossover discrepancy arcs were located in the Pacific area, therefore, two regional adjustments for the Pacific area and another two for the remaining areas were performed. The results are shown in Table A1.

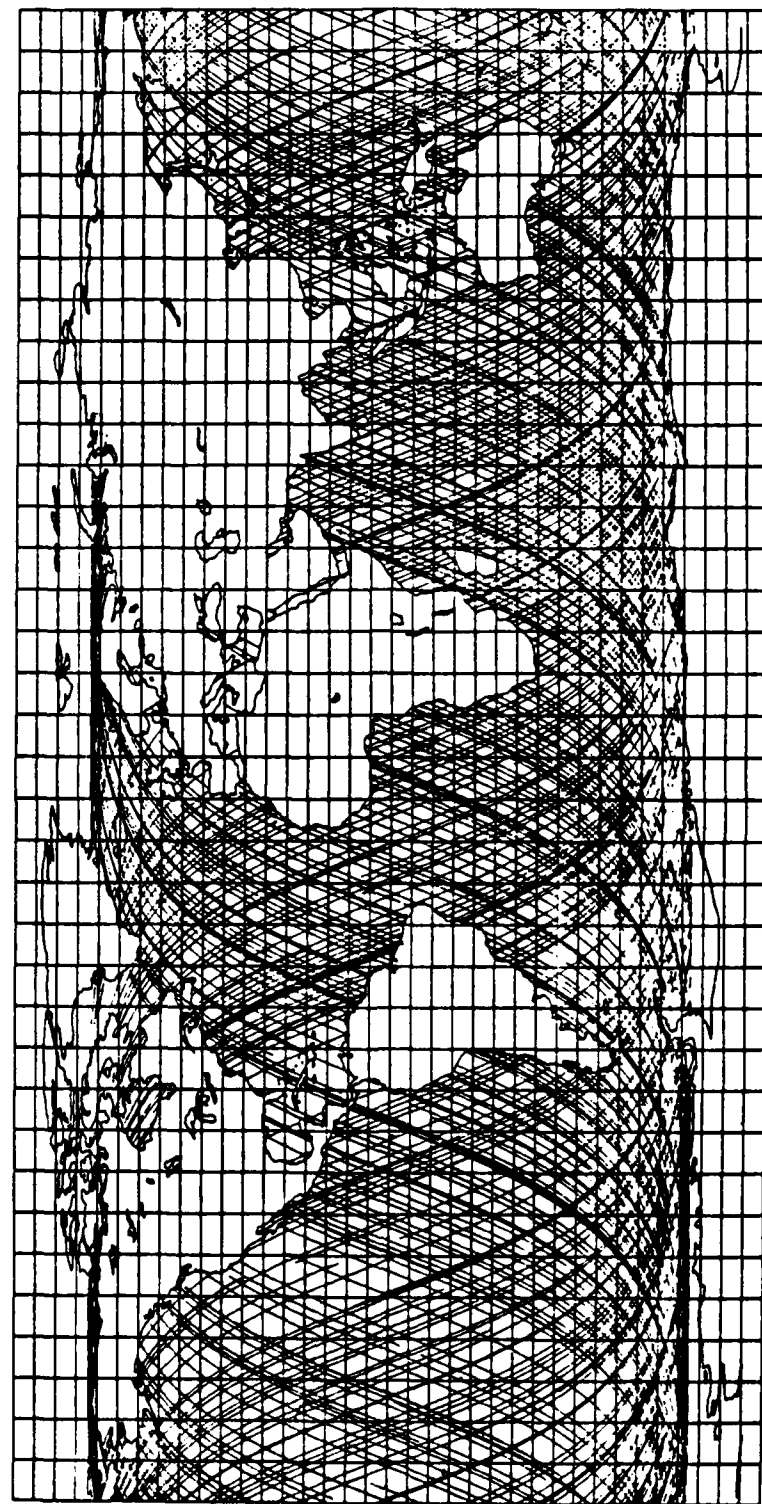


Figure A1  
Distribution of the SEASAT Primary Arcs.

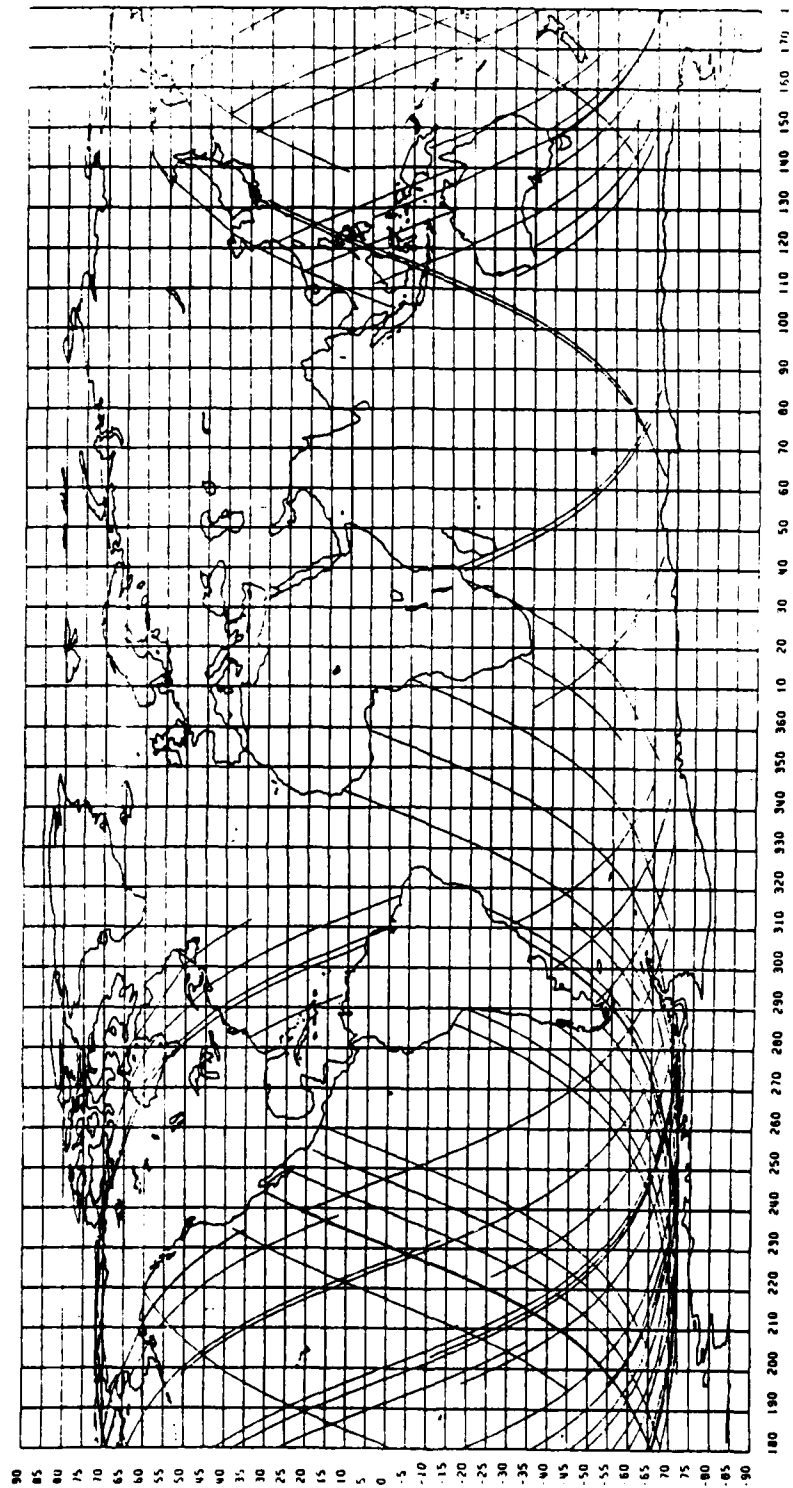


Figure A2  
53 Arcs Having Crossover Discrepancies Larger Than 40 cm.

Table A1  
Locations and Statistics of Selected Primary Arc Adjustment

Region	N. Pacific	S. Pacific	North	South	Total
Latitude	-2°44'72"	-72°44'42"	-2°44'72"	-72°44'42"	
Longitude	158°E44'98"W	158°E44'98"W	102°W44'162°E	102°W44'162°E	
no. of cut arcs	23	30	16	29	98
no. of crossovers	256	523	93	362	1234
*priori RMS crossover discrepancies cm	40	36	36	31	35.5
**posteriori RMS crossover discrepancies cm	22	21	23	24	22.3

\* after the primary adjustment

\*\* after the readjustment

After the readjustments, the data sets containing the primary adjusted arcs were updated. Only the adjusted sea surface heights of the readjusted arcs were replaced. The remaining data points were kept the same as before. With the updated data sets, 0:25x0:25 grid collocation predictions were carried out and the results compared to values predicted from the previously adjusted Seasat data. The irregular track patterns that were present in the latter results were no longer present in the revised data set. It was clear that a substantial improvement had been made with the revised Seasat data. We should note that no readjustment of the local arcs to the newly adjusted Seasat arcs was made. In principle this should be done but the effect in not doing this is expected to be small.

Appendix B  
Estimates of Sea Surface Topography

prepared by Theodossios Engelis

In order to determine the geoid from altimeter measurements, an estimate of the stationary sea surface topography (SST) is required. The stationary SST represents the deviation of the mean sea surface from the geoid (appropriately defined), caused mainly by oceanic circulation phenomena. The geoid in turn, has to be defined in such a way that the average non tidal SST is zero, for a specific epoch of measurement, as sampled globally in the oceanic regions (Rizos, 1980).

To date, only estimates of the large scale SST are available. These estimates have been computed either by geodetic techniques (Engelis 1983, 1985, Engelis et al 1984, Tai and Wunsch 1984) or by traditional oceanographic methods (Levitus, 1982).

Geodetic techniques require an independent estimate of the marine geoid, which is provided only by satellite derived gravity fields. These gravity fields have accuracies which are acceptable, for SST determinations, only for very long wavelengths. Consequently, only the large scale SST can be adequately determined and used to correct the mean sea surface to obtain an estimate of the geoid.

In recent studies by Engelis (1985) long wavelength SST was determined as follows: a set of 1° gridded sea surface heights was used to represent the mean sea surface as realized by SEASAT. The geoid was implied by using the GEM2 gravity model up to degree 6 (providing an accuracy of 18 cm in geoidal heights). Then the difference of the two, up to degree 6, would in principle provide the large scale SST. In order to reduce the leakage of energy between different wavelengths due to the inconsistent representation of the geoid and the mean sea surface, the gravity model by Rapp (1981) was used from degree 7 to 180, to create geoidal heights with wavelengths comparable to the ones of the sea surface heights. Then, raw estimates of SST were obtained by differencing the two sets. In order to conform with the definition of the geoid, the mean value of these estimates was obtained and a new data set was created that had a zero mean. In this set zeros have been used for land and the polar regions. This global set has been harmonically analysed and harmonic coefficients up to degree 6, representing SST effects, were retained. Synthesis of these coefficients provided maps of SST up to degree 6 that can be found in Engelis (1985). Errors that are to be associated with such a determination of the SST include errors in the GEM2 model up to degree 6, very long wavelength orbital errors remaining from the crossover adjustment and leakage of energy between coefficients due to errors in the Rapp model and shorter wavelength orbital errors. The estimated accuracy of the SST estimates is on the order of 20 to 25 cm.

Sea surface topography has also been determined by oceanographic methods. These methods, being unable to use an estimate of the geoid, define a deep surface as a level of no motion (equipotential surface) and then they determine the mean annual anomaly of geopotential thickness of the layer between that surface and the surface of the oceans, using geostrophy assumptions. The data used are salinity, temperature, and dissolved oxygen observations. The most recent determination of such a dynamic sea surface topography was made by Levitus (1982). A 2000 dbar deep surface was used as a reference. The data that Levitus has used were obtained by the National

Oceanographic Data Center. This data file represents all observations of salinity, temperature, and dissolved oxygen taken over several decades. A first analysis made by Levitus indicated several problems. The most important were regional biases of data and lack of data in extended regions. Moreover there were representative problems of the data, since observations were not synoptic but scattered with respect to time (with the exception of a few limited areas) and so, the results cannot in a strict sense be considered a true long term average.

After the initial stability and statistical checks to eliminate spurious observations, averages of data in  $1^\circ \times 1^\circ$  blocks were created by Levitus. In order to overcome biases and lack of data and to improve their representativeness, a smoothing analysis was performed. The smoothing operation was a weighted average operation in which a Gaussian type filter was used as a weighting operator. First, approximate values for each grid point were assigned. Then, corrections to the approximate values were computed as a distance weighted mean of all grid points within the area specified by the radius of the Gaussian filter. The iterations were repeated until convergence. After each iteration, the resulting data set was smoothed by a five point smoother. During this smoothing operation the radii of the Gaussian filter ranged from 1540 km to 770 km resulting in the total elimination of any signal with wavelengths less than 600 km, while wavelengths between 600 km and 3000 km were affected with changes in the amplitudes of the signal. For example, wavelengths of 1000 km had a reduction in amplitude of about 50% (Levitus, 1982, Figure 11). The minimum wavelengths of some existing signal is of the order of 800 km, roughly corresponding to an harmonic degree 20. Levitus considers that the resulting large scale features are representative of the real ocean, although it is expected that some local differences would occur because of interannual variability. This smoothed data set was used to compute the annual mean anomaly of geopotential thickness of the 0-2000 m layer assuming the 2000 m level as a level of no motion and also assuming geostrophy.

The Levitus estimates of SST were available to us in  $1^\circ \times 1^\circ$  means in the oceanic areas of the world. The global mean value of this data set was 202 dyn cm. First analysis of that data indicated the existence of some outliers in the west Pacific and the extremely negative values of SST in the Mediterranean Sea. Areas with no data were found in the North Sea and along many of the coastlines. The outliers in the west Pacific were substituted by the global average. For the Mediterranean Sea, estimates from a map of Lisitzin with respect to a 4000 meter surface (Lisitzin 1974, p.153) were used to substitute the estimates of Levitus. In order to put the Lisitzin estimates in the same reference system as the Levitus set, their mean value was subtracted and the global mean value of Levitus set was added.

The analysis of the Levitus SST was carried out similar to the analysis of the Seasat-GEML2 derived SST. So, a new mean value was computed (204 dyn cm) and subtracted from the original estimates and zeros were assigned on land, in areas with no data and polar regions (beyond  $-70$  and  $70$  degrees). Some discontinuities that are created especially in areas with some lack of data cannot be avoided, although they are not important since they mainly distort the higher part of the frequency spectrum and so they do not significantly

affect the determination of the large scale SST. This global data set has then been harmonically analysed, using procedures appropriate for mean values (Colombo, 1980). The harmonic analysis was carried out up to degree 100, although it was expected that beyond degree 20 one would mainly have white noise. The power spectrum of Levitus' SST, shown in Figure B1, just shows such a behavior. Coefficients up to degree 20 were used to generate the SST map shown in Figure B4.

Comparison between the two sets up to degree 6 made by Engelis (1985) indicates that, except for the smoother behavior of the Levitus set, the two sets are compatible in representing qualitatively the major features of the ocean topography. Indeed only their amplitudes differ, while there is no change in polarity, with the exception of the Indian Ocean. Moreover, it was seen in our tests that contributions of degrees 7-20 in the Levitus set simply enhance the larger scale features without creating any changes in the phase. These facts indicate that features with wavelengths in the band between 7 and 20 harmonic degrees can be combined with the lower degree coefficients derived from Seasat. Tests have shown that such an addition, although consistent, is not very significant since (mainly because of the smoothing in the Levitus original data) the total power in the band 7-20 is  $334 \text{ cm}^2$ , accounting only for 10% of the total power of  $3340 \text{ cm}^2$  of the Seasat SST up to degree 6. The contribution of the coefficients between 7-20 degrees, in terms of SST itself, has a maximum effect of about 10cm occurring in the southern latitudes while in most of the oceanic regions it hardly exceeds 5 cm. The power spectrum of this combined set is given in Figure B2 while a contour map is given in Figure B5.

For the gravity anomaly recovery from altimetry, SST can be used in correcting the sea surface heights before their usage for  $\Delta g$  recovery, or alternatively it can be used to compute the effect of SST coefficients in terms of  $\Delta g$  correction and apply that correction after the gravity anomalies are computed. In the first case global gridded SST estimates have to be computed. Then by one simple bilinear interpolation one can determine the SST correction at any point of interest and apply it to the corresponding sea surface height to get the geoidal undulation. In the second case the SST coefficients are used to compute a  $\Delta g$  correction, using the traditional synthesis for gravity anomalies. Considering that the second method is much more convenient to apply, we chose it for the correction of the altimetrically derived gravity anomalies due to SST effects. A map showing the magnitudes of the  $\Delta g$  correction using coefficients up to  $n = 20$  is shown in Figure B6, while the power spectrum in terms of  $\Delta g$  is shown in Figure B3.



## References to Appendix B

- Colombo, O., "Numerical Methods for Harmonic Analysis on the Sphere", Dept. of Geodetic Science, Report no. 310, The Ohio State University Columbus, 1981
- Engelis, T., "Analysis of Sea Surface Topography from Seasat Altimeter Data", Dept. of Geodetic Science and Surveying, Report No. 343, The Ohio State University, Columbus, 1983
- Engelis, T., "Global Ocean Circulation from Seasat Altimeter Data", Marine Geodesy, Vol 9, No. 1, 1985
- Engelis, T. and Rapp, R. H., "Global Ocean Circulation Patterns Based on Seasat Altimeter Data and the GEML2 Gravity Field", Marine Geophysical Researches 7, pp 55-67, 1984
- Levitus, S., "Climatological Atlas of the World Ocean", NOAA, Geophysical Fluid Dynamics Laboratory, Professional Paper 13, Rockville, MD, 1982
- Lisitzin, E., "Sea Level Changes", Elsevier Oceanography Series, Amsterdam, 1974
- Rapp, R.H., "The Earth's Gravity Field to Degree and Order 180 Using Seasat Altimeter Data", Dept. of Geodetic Science and Surveying, AFGL-TR-82-0019, AD-A113 098/8, Report No. 322, The Ohio State University, Columbus, 1981
- Rizos, C., "The Role of Gravity Fields in Sea Surface Topography Studies", School of Surveying, Kensington, University of NSW, Sydney, Australia, 1980
- Tai, C. and C. Wunsch, "An Estimate of Global Absolute Dynamic Topography", Journal of Physical Oceanography, 1984

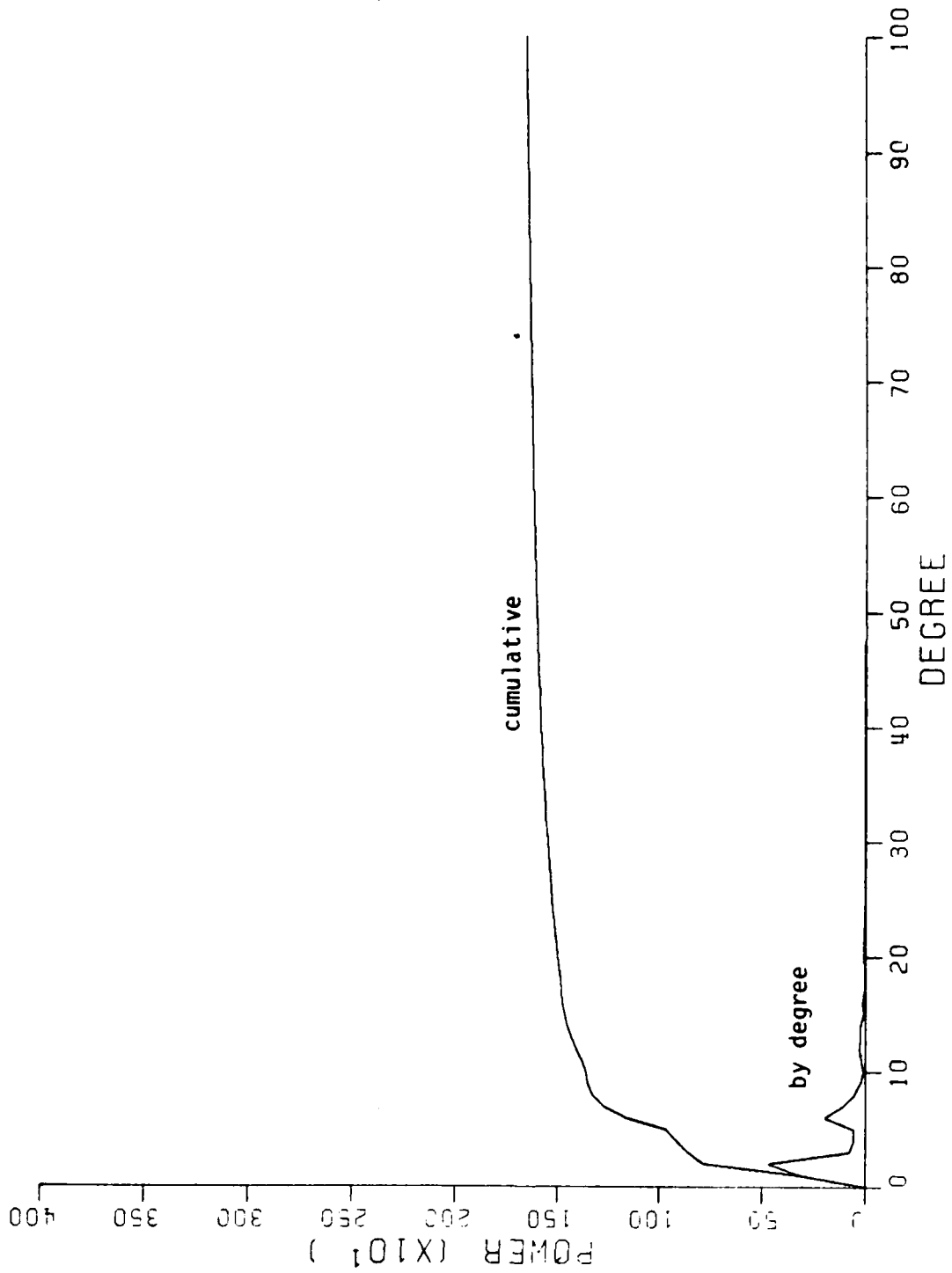


Figure B1  
 Cumulative and By Degree Power Spectrum of the Levitus SST. Units are in cm<sup>2</sup>.

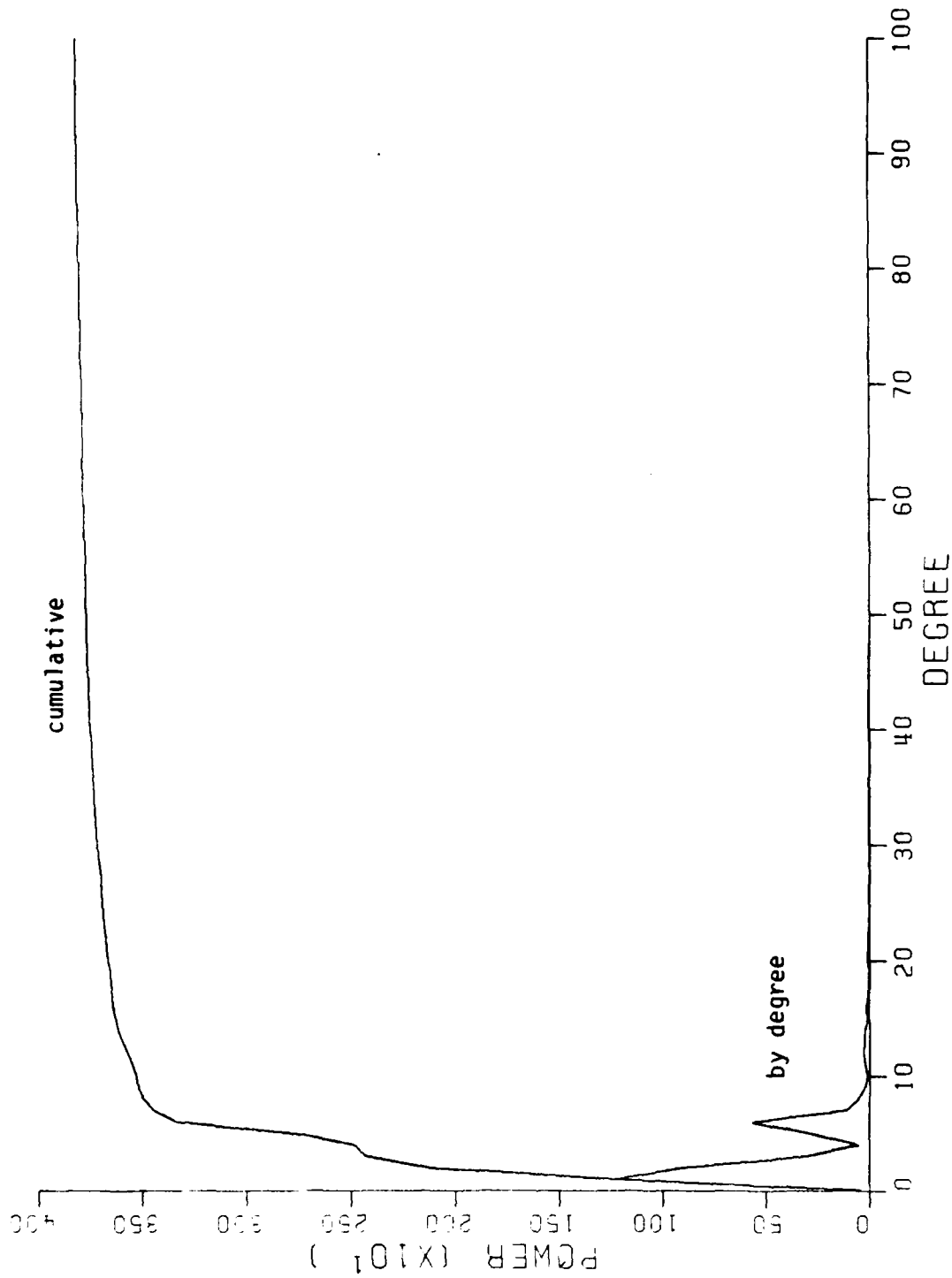


Figure B2  
 Cumulative and By Degree Power Spectrum of SST as Derived From a Combination of Seasat and Levitus  
 SST Coefficients. Units are in cm<sup>2</sup>.

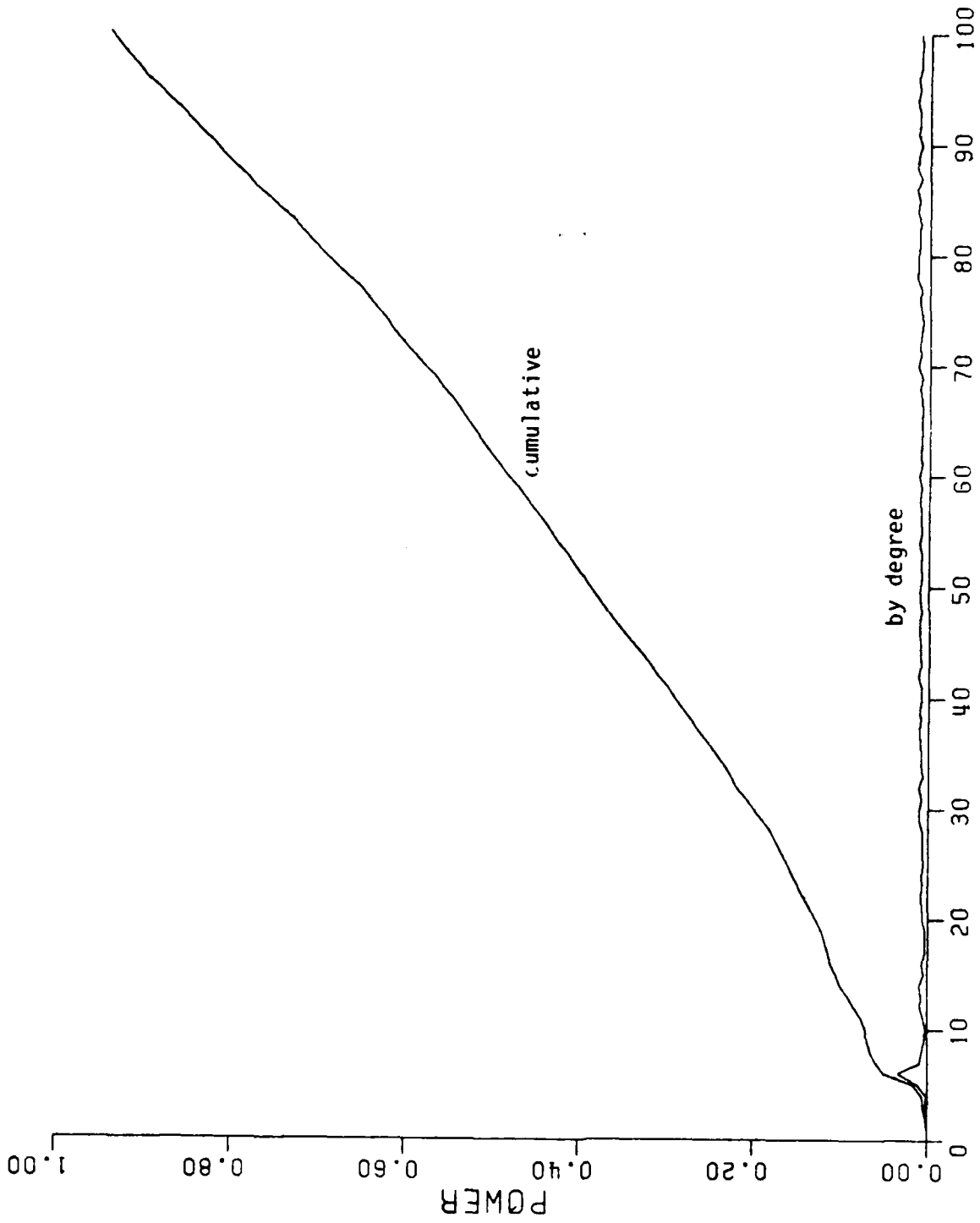


Figure B3  
 Cumulative and By Degree Power Spectrum in Terms of Anomaly Correction as Computed From the  
 Seasat-Levitus SST Coefficient Set. Units are in  $\text{mgal}^2$ .

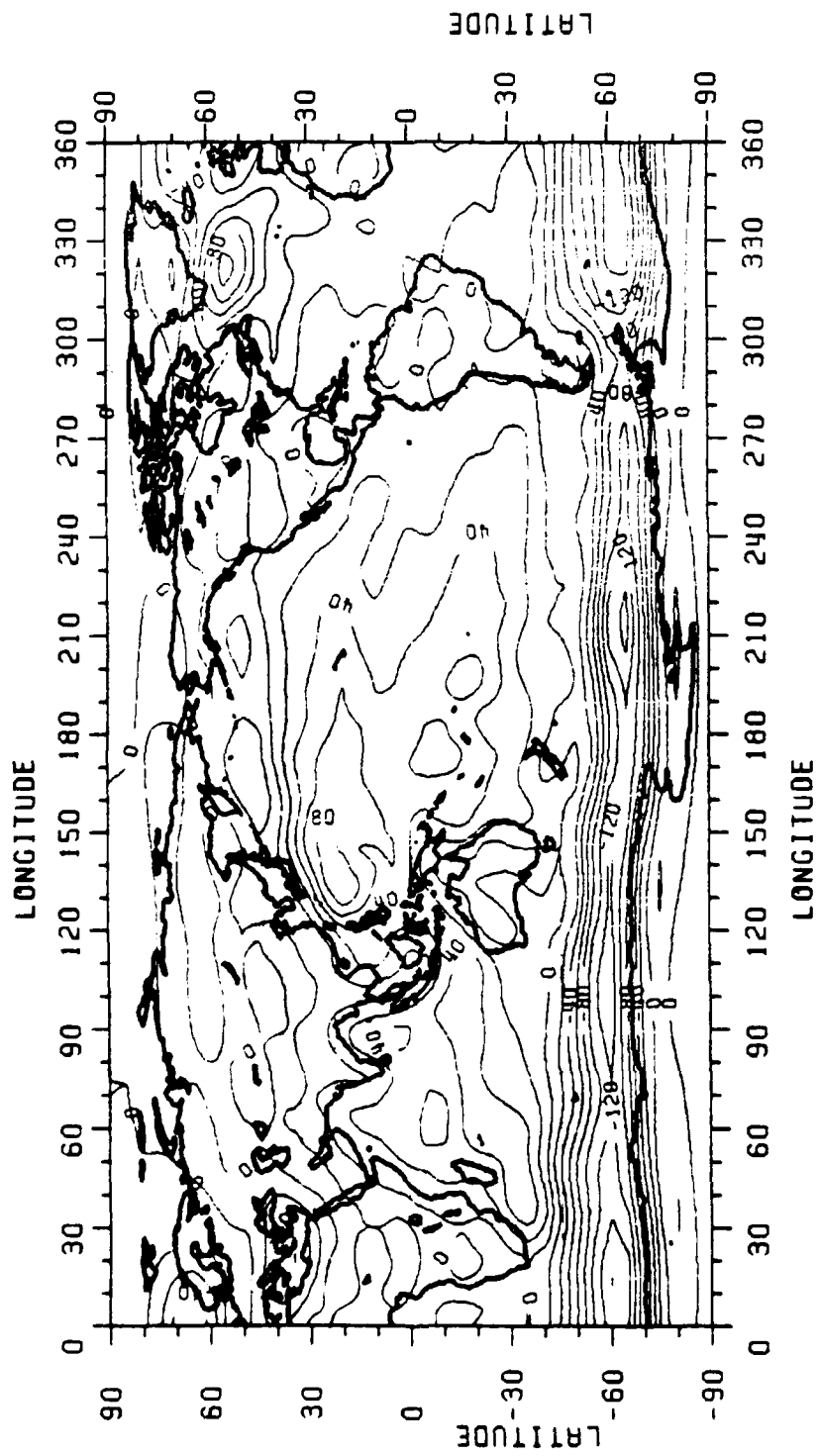


Figure B4  
 Sea Surface Topography Based on the Levitus Data Set Using a Spherical Harmonic Expansion to Degree  
 20 (Contour Interval is 20 cm)

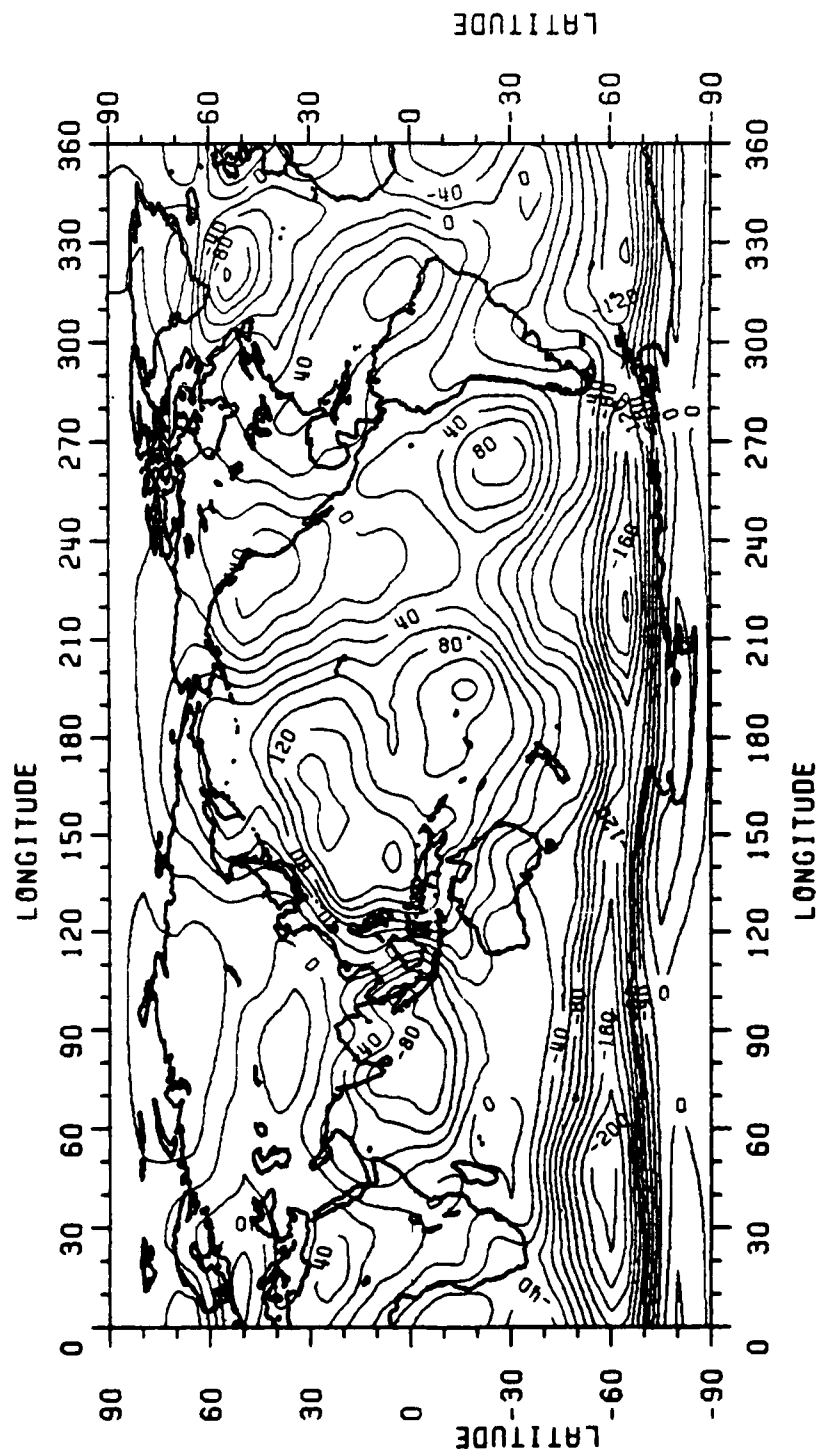


Figure B5  
 Sea Surface Topography Based on the Seasat/Levitus Coefficients to Degree 20 (Contour Interval is 20 cm)

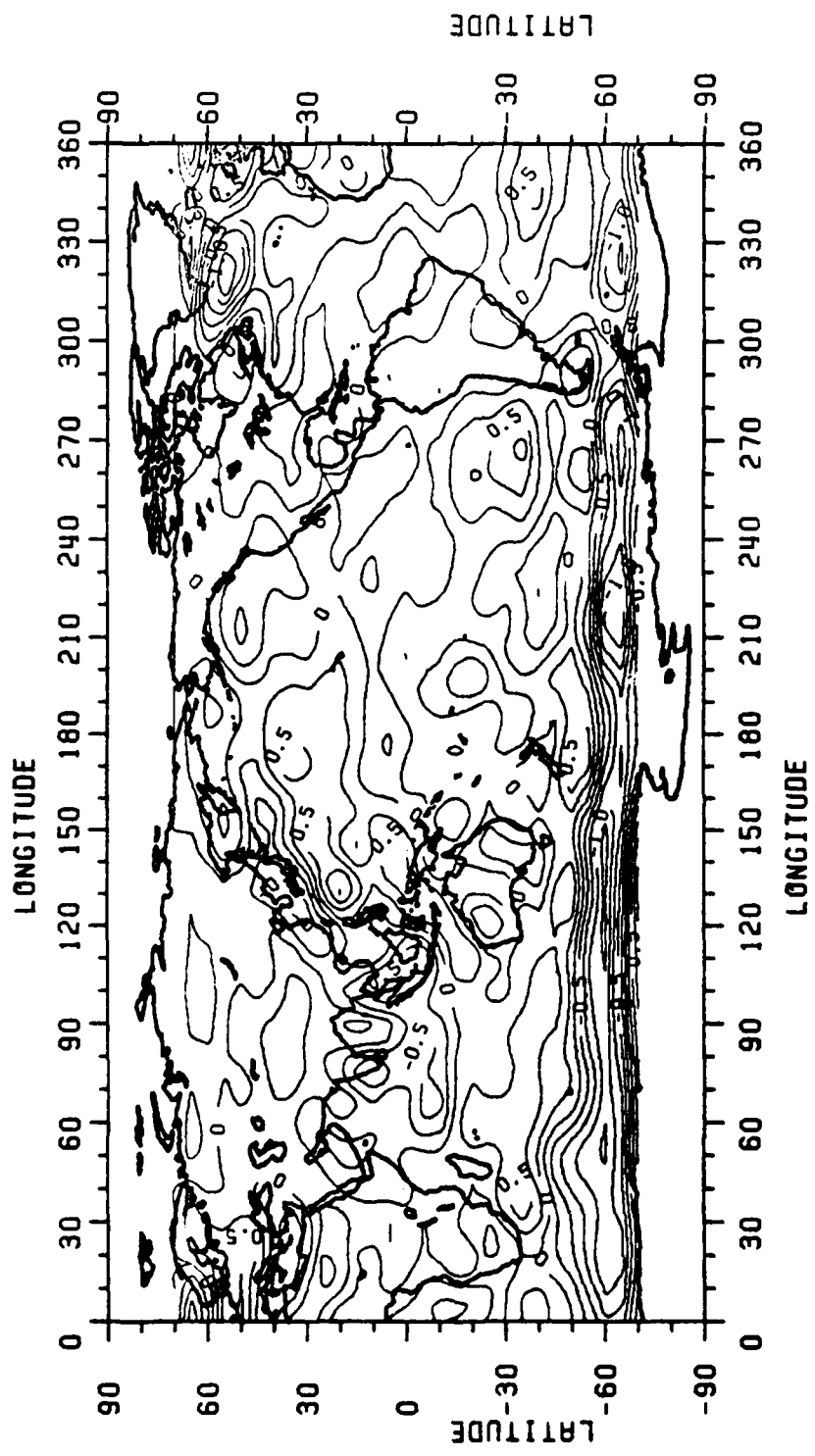


Figure B6  
Gravity Anomaly Correction Terms (Based on a Spherical Harmonic Expansion to Degree 20) to be Subtracted From the Estimates Derived Directly From Sea Surface Heights (Contour Interval is 0.25 mgal)

Appendix C

Power Spectrum Analysis of the  $1/8^\circ \times 1/8^\circ$  Anomalies

prepared by Theodossios Engelis



In order to obtain an estimate of the frequency content of the  $1/8^\circ \times 1/8^\circ$  gravity anomalies recovered from altimetry, a power spectrum analysis of eight profiles is performed. These profiles are  $60^\circ$  long (481 data points) and are taken to be along meridians, so that there is a uniform spacing in all of them. The locations of the profiles are shown in Figure C1.

Estimation of the power spectral density (or simply power spectrum) of discretely sampled deterministic or stochastic signals can be made by several methods (Kay et al., 1981). One approach is based on procedures employing the Fast Fourier Transform (FFT) technique which has been shown to give reasonable results for a large class of signals and also is computationally efficient. Problems that are associated with this approach relate to the inability to distinguish between the signal and the noise inherent in the sampled data and to the low resolution of the recovered spectrum.

An additional problem is due to the implicit windowing of the data that occurs when processing with the FFT. Windowing manifests itself as leakage in the spectral domain, i.e. energy in the main lobe of the spectral response leaks into the sidelobes, obscuring and distorting other spectral responses that are present. Appropriate smoothing of the spectrum can reduce leakage effects at the expense of resolution.

Conventional FFT spectral estimation is based on a Fourier series model of the data. Indeed if  $x(n)$  is a series of  $N$  data at  $N-1$  equispaced intervals  $\Delta x$ , then by taking its Fourier transform we obtain:

$$X(f) = \frac{1}{N} \sum_{n=0}^{N-1} x(n) e^{-j2\pi f n \Delta x} \quad (C1)$$

where  $f$  is the frequency (in cycles per total length of the profile), which according to the well known sampling theorem, can only be recovered in the interval  $-(1/2\Delta x) \leq f \leq (1/2\Delta x)$ . ( $1/2\Delta x$  is the so-called Nyquist frequency). Use of the FFT permits evaluation of the above equation at the discrete set of  $M$  equally spaced frequencies  $f_m = m\Delta f$  for  $m = 0, 1, \dots, M$  and  $\Delta f = 1/N\Delta x$ . Then we obtain:

$$X_m = \frac{1}{N} \sum_{n=0}^{N-1} x(n) e^{-j2\pi \frac{mn}{N}} \quad (C2)$$

The index  $M$  corresponds to the Nyquist frequency  $1/2\Delta x$ . So it is:

$$M = \begin{cases} \frac{N}{2} & N \text{ even} \\ \frac{N-1}{2} & N \text{ odd} \end{cases} \quad (C3)$$

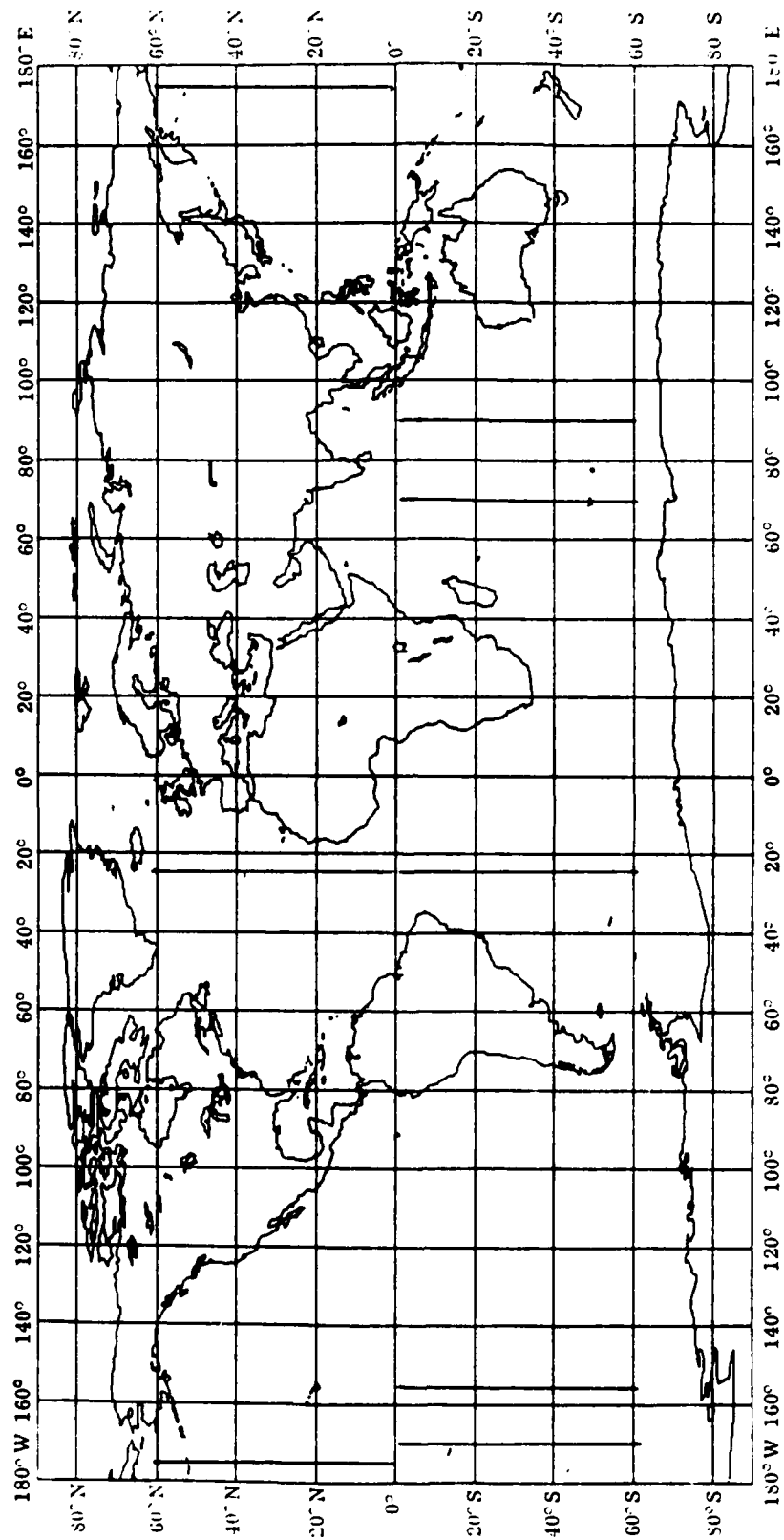


Figure C1  
Location of Anomaly Profiles for Which Power Spectra Were Computed.

Once the Fourier transform is obtained, the power spectrum is simply:

$$P_m = \begin{cases} |X_m|^2 & m = 0 \\ 2|X_m|^2 & 0 < m \leq M \end{cases} \quad (C4)$$

This estimate of the power spectrum, also known as the periodogram, is usually quite erratic due to leakage and has to be smoothed. Different smoothing windows can be applied. One of them, widely suggested, is the Hanning window which in the frequency domain is simply the smoothing of the original periodogram as follows:

$$\begin{aligned} \bar{P}_m &= 0.25P_{m-1} + 0.50P_m + 0.25P_{m+1} \\ \bar{P}_0 &= 0.5P_0 + 0.5P_1 \\ \bar{P}_M &= 0.5P_{M-1} + 0.5P_M \end{aligned} \quad (C5)$$

An alternative procedure, also using FFT techniques and yielding identical results if properly applied, is the one via an autocovariance function estimate, also known as the Blackman and Tuckey method (Blackman and Tuckey, 1959). In this method the power spectrum is:

$$P(f) = \frac{1}{N} \sum_{n=-L}^L C_{XX}(n) e^{-j2\pi f n \Delta x} \quad (C6)$$

where  $C_{XX}(n)$  is the autocovariance function at lags  $n\Delta x$  up to a maximum of  $L\Delta x \leq (N-1)\Delta x$ . Again  $f$  can only be recovered in the interval  $-(1/2\Delta x) \leq f \leq (1/2\Delta x)$ . Use of the FFT can give us estimates of  $P(f)$  at the discrete frequencies  $f_m = m\Delta f$  where  $\Delta f = 1/N\Delta x$ , up to  $f_m = 1/2\Delta x$ . Then:

$$P_m = \frac{1}{N} \sum_{n=-L}^L C_{XX}(n) e^{-j2\pi \frac{mn}{N}} \quad (C7)$$

This method yields identical results with the previous one if  $L = N-1$ . The autocovariance function can be computed by:

$$C_{XX}(n) = \frac{1}{N-n} \sum_{k=0}^{N-n-1} x(k+n)x(k) \quad (C8)$$

which is an unbiased estimate of the true autocovariance function. Since the variance of this estimate tends to be high for larger lags giving an erratic behaviour to  $C_{XX}$ , it is usually computed up to  $L = N/2$  if  $N$  is even or  $(N-1)/2$  if  $N$  is odd. Additionally a smoothing window must be applied. The Hanning window in the space domain is:

$$W(n) = \begin{cases} \frac{1}{2} \left( 1 + \cos \frac{\pi n}{L} \right) & n \leq L \\ 0 & \text{otherwise} \end{cases} \quad (C9)$$

To smooth the autocovariance function the window weights  $W(n)$  are multiplied to  $C_{XX}(n)$ .

The Blackman and Tuckey method has been applied to the eight profiles under investigation. In order to reduce leakage effects due to existing power at wavelengths larger than  $60^\circ$ , the gravity anomalies defined by the GEM9 potential coefficients complete up to degree 20 were first subtracted. This operation effectively removed all constant terms and substantially reduced any existing trends.

Since the spacing ( $\Delta x$ ) between the gravity anomalies is  $0:125$  and there are 481 data samples, the frequency increment is:

$$\Delta f = \frac{1}{480 \times 0.125} = 1 \text{ cycle/60 degree} \quad (C10)$$

which is also the minimum frequency of the spectrum. The Nyquist frequency is 4 cycles/degree. On the other hand, since the wavelength  $\lambda$  is defined as  $\lambda = 1/f$ , the maximum wavelength that is resolvable is  $\lambda_{\max} = 60^\circ$  and the minimum is  $\lambda_{\min} = 0:25$ .

The wavenumber  $m$  can be related to the corresponding spherical harmonic degree  $l$ , using the following ratio:

$$\frac{l}{360^\circ} = \frac{m \Delta f}{1} \quad (C11)$$

or, using (C10):

$$l = 6m \quad (C12)$$

In principle the smallest spherical harmonic degree in the profiles is 6 (i.e.  $m = 1$ ) while the maximum degree is 1440 (i.e.  $m = 240$ ). Because  $m$  increases in steps of 1, it is clear from (C12) that the values of  $l$  implied by the profile are

determined only in steps of 6; i.e. the frequency resolution in terms of harmonic degrees is 6. If a reference field to degree 20 is used, the minimum wavenumber for which power should exist in the spectrum should be 3. If a reference field to degree 180 is used, the minimum wavenumber is 30.

After the power spectra for all the profiles have been computed and plotted, some conclusions can be drawn:

First, in all the spectra there is some power up to wavenumber 3. This power is implied by the residual anomalies with respect to GEM9. This contribution is expected to come from errors in the GEM9 model, errors in the altimetric  $\Delta g$  due to long wavelength orbital errors, data errors, and the neglect of sea surface topography.

Second, the power is negligible above a certain wavenumber in the range of 134-202 depending on the profile. This indicates that the 0:125 data spacing does not really provide us information up to the corresponding maximum wavenumber which is 240. In the above, negligible contribution is considered (rather arbitrarily) to be less than 0.3% of the total power. The maximum wavenumber and the corresponding wavelength for each of the profiles are shown in Table C1. From the table one can also see the variances of the profiles which range from 113 to 1521  $\text{mgal}^2$ .

In order to obtain a more definitive picture of the power spectrum for the eight profiles, their average spectrum has been computed and shown in Figure C2. Again we can draw similar conclusions. More specifically, the power attributed to the discrepancy between GEM9 and altimetric  $\Delta g$  still exists and amounts to about 77  $\text{mgal}^2$  (cumulative power up to wavenumber 3). The formal accuracy estimates for GEM9 give a total error variance of 15  $\text{mgal}^2$ , which is not consistent with the discrepancy of 77  $\text{mgal}^2$  reported above, thus indicating that the additional errors (orbital errors etc) are expected to have a significant power, of the order of 60  $\text{mgal}^2$ .

Table C1  
Power Information of the 60° Latitude Profiles

Profile		Variance* $\text{mgal}^2$	Max Frequency of non-negligible power	
N.Lat	Lon		wavenumber	wavelength
61	175	853	160	0:375
61	185	1013	134	0:447
61	335	393	137	0:437
-1	70	211	201	0:300
-1	90	208	176	0:340
-1	190	306	171	0:350
-1	205	113	202	0:300
-1	335	1521	136	0:440
Average		577	155	0:380

\* with respect to the GEM9 gravity field to degree 20

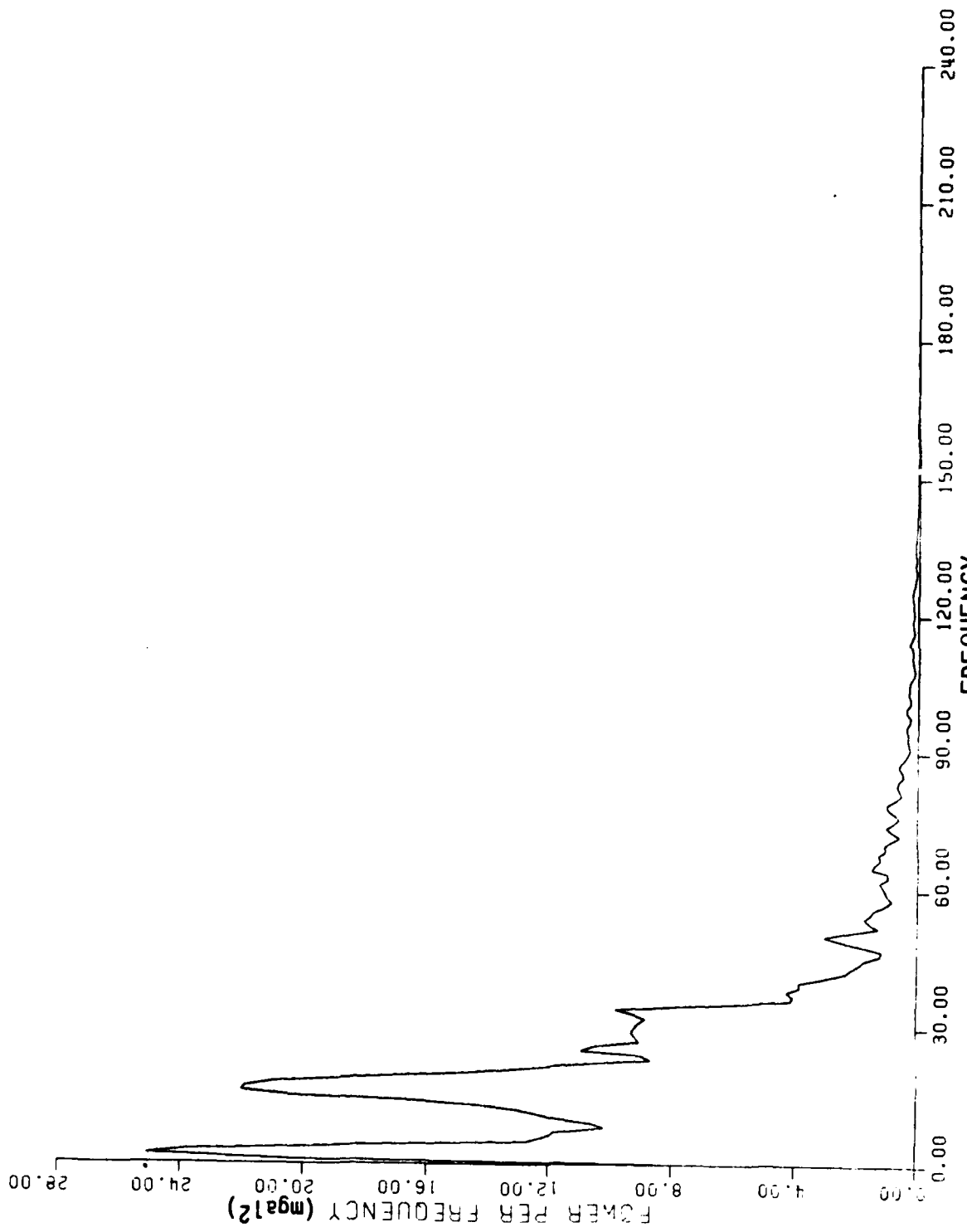


Figure C2  
 Average Power Spectrum From Eight 60° Latitude Profiles.  
 (Units of frequency are cycles/60 degrees)

In a similar way, it is observed that about 75% of the total power is contained in frequencies corresponding to degrees up to  $l_{\max} = 180$  (or 0.5 cycles/degree) and about 90% to frequencies corresponding to  $l_{\max} = 360$  (1 cycle/degree). In the average power spectrum the contribution of power is negligible (less than 0.3%) above the wavenumber 155 (2.6 cycles/degree) or above harmonic degree 930. This corresponds to a minimum wavelength of about 0.38 or in a data spacing of 0.19. This minimum wavelength is consistent with the one found by Brammer and Sailor (1982). From a coherent analysis of overlapping passes of SEASAT they have established that the minimum wavelength that can be recovered from altimetry is of the order of 40 km (0.36). Smaller wavelengths cannot be recovered since the signal to noise ratio is unfavorable and so the signal is completely contaminated by noise. In our spectrum estimation the power at these frequencies is zero because the noise and the contaminated signal have been effectively removed by the least squares collocation.

Considering the above discussion the selected spacing of 0.125 is justified since a wider spacing, say 0.25, would result in some loss of information. This argument becomes stronger if we consider that the aliasing effects, which always arise during the discretization of a continuous non-bandlimited signal, would be larger if a wider spacing had been chosen.

The above discussions yield the conclusion that these power spectral estimates are qualitatively correct. It is believed that analysis of more profiles will give more reliable results although they are not expected to considerably differ from the ones analysed above.

## REFERENCES

- Blackman, R.B., and J.W. Tukey, "The Measurement of Power Spectra from the Point of View of Communication Engineering", Dover Publications Inc., New York, 1959.
- Sailor, R.V., "Determination of the Resolution Capability of the Seasat Radar Altimeter, Observations of the Geoid Spectrum, and Detection of Seamounts", Report TR-3751, The Analytic Sciences Corp, Reading, MA 01867, May 1982.
- Forsberg, R., "Local Covariance Functions and Density Distributions", AFGL-TR-84-0214, ADA150792, Report No. 356, Department of Geodetic Science and Surveying, The Ohio State University, Columbus, 1984.
- Kay, S.M., and S.L. Marple, Jr., "Spectrum Analysis - A Modern Perspective", Proceedings of the IEEE, Vol. 69, No. 11, November 1981.



Appendix D

Location of Rough, Mild, and Smooth 15°x15° Areas Used in Spectrum  
Classification

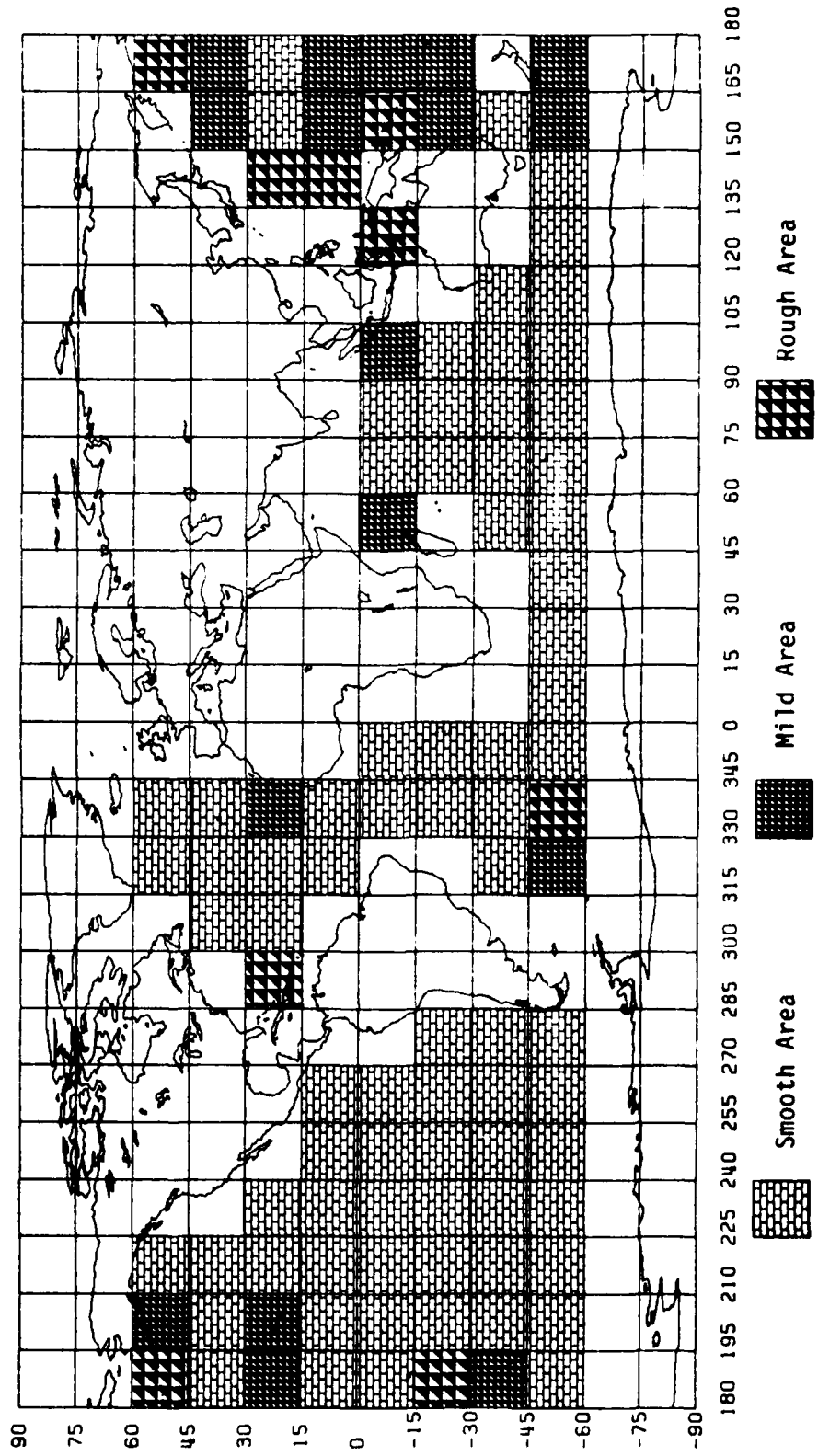


Figure D1

END

Dtjc

5-86